12-2017

# Numerical Studies of Iron Based Superconductors using Spin-Fermion Models

Christopher Brian Bishop
*University of Tennessee, Knoxville*, cbisho12@vols.utk.edu

To the Graduate Council:

I am submitting herewith a dissertation written by Christopher Brian Bishop entitled "Numerical Studies of Iron Based Superconductors using Spin-Fermion Models." I have examined the final electronic copy of this dissertation for form and content and recommend that it be accepted in partial fulfillment of the requirements for the degree of Doctor of Philosophy, with a major in Physics.

Adriana Moreo, Major Professor

We have read this dissertation and recommend its acceptance:

Elbio Dagotto, Steve Johnston, Takeshi Egami

Accepted for the Council:
Carolyn R. Hodges

Vice Provost and Dean of the Graduate School

(Original signatures are on file with official student records.)

# Numerical Studies of Iron Based Superconductors using Spin-Fermion Models

A Dissertation Presented for the

Doctor of Philosophy

Degree

The University of Tennessee, Knoxville

Christopher Brian Bishop

December 2017

# Acknowledgements

I would like to thank Shuhua Liang for all of his help during my early stages of graduate research. For all of the opportunities and guidance that she has given me throughout my graduate years, I would like to thank my advisor Dr. Adriana Moreo. I would also like to thank my brothers for all of their support. Lastly, I would like to thank my parents Leonard and Carol Bishop. Without their support and sacrifices this Dissertation would not have been possible.

# Abstract

The iron pnictide and iron chalchogenide superconductors are studied numerically using classical Monte Carlo techniques to reproduce experimental data and make predictions about the nature of the relevant interactions. The focus will be using Spin-Fermion models in a classical approximation to explore the phase diagram and calculate important physical properties of these materials over a wide range of temperatures.

# Table of Contents

# List of Tables

# List of Figures

# Chapter 1

# Introduction

## 1.1  High Temperature Superconductors

Several materials have been found to have zero resistivity after they are cooled below some critical temperature, $T_c$. This phenomenon, called superconductivity, was first discovered by Heike Onnes in purified mercury [1]. Since for mercury $T_c \sim 4$ K, this discovery was due in large part to Onnes' ability to liquefy Helium whose temperatures were the lowest ever produced on Earth at the time. Despite many more superconducting materials being discovered afterwards, it was not until decades later when Bardeen, Cooper, and Schrieffer published their theory of superconductivity [2] that the underlying mechanism was explained. In BCS theory, the superconducting phase arises when the attractive retarded electron-phonon interactions overcome the Coulomb repulsion among electrons, forming quasiparticles, known as Cooper pairs. This description was sufficient to describe superconductivity in the contemporary materials until the first unconventional superconductor [3], $CeCu_2Si_2$, was discovered that could not be explained by the BCS mechanism.

In 1986 Bednorz and Müller [4] discovered the first high temperature unconventional superconductor when $Ba_xLa_{5-x}Cu_5O_{5(3-y)}$ was cooled below $T_c \sim 35K$ and the material became superconducting. This was the highest $T_c$ discovered at this time. The subscript x indicates the replacement of La by Ba which introduces hole doping in the compound. However other cuprates were later found that become superconductors upon electron

doping [5]. These layered materials characterized by $CuO_2$ planes (See Fig. 1.1(Top)) have become collectively known as the cuprate family of high temperature superconductors. Much attention was given to these materials for the next decade because of the promise of synthesizing materials with higher $T_c$. However, $HgBa_2Cu_3O_8$, the cuprate with the highest $T_c$ at $T_c = 134$ K was discovered in 1993 [8]. A new breakthrough occurred in 2008 when the material $LaFeAsO_{1-x}F_x$ was discovered to be another unconventional high temperature superconductor with $T_c \sim 26$ K [9]. Since that time many other iron based superconductors (FeSC) have been discovered and currently there are six different families of these materials. Referencing Fig. 1.1(Bottom), the 1111, 122, and 111 pnictide compounds are categorized by the ratio of their constituent atoms and this family of materials can be characterized by their Fe and pnictide (elements in the 15th column of the periodic table) layers. The 11 chalcogenide compounds have the simplest structure and only contain layers of chalcogenides (elements in the 16th column) and Fe.

The study of the FeSC will be the focus of this dissertation. The FeSC are complex materials that have multiple degrees of freedom (DOF) whose contributions must be isolated in order to understand the importance of each. In this manuscript, the focus will be to determine which DOF are most relevant to describe several of the properties observed in the pnictides and chalcogenide FeSC. This will be accomplished by developing models that capture the individual contributions of each DOF over a wide temperature range. In the remainder of this Chapter, the general properties of the FeSC will be described.

## 1.2 Properties of the Iron Pnictides

The discovery of unconventional high temperature superconductivity in the Fe-based superconducting materials prompted comparisons to the cuprates. Both families of materials have parent compounds that are magnetic and non-superconducting. They are complex layered materials that become superconducting upon doping with either electrons or holes (See Fig. 1.2). As previously mentioned, the layers of interest for the cuprates are those containing the copper oxide planes with $CuO_2$ per unit cell. As can be seen in Fig. 1.3(a), this layer contains the Cu's in a square lattice with coplanar oxygen in the links that connect
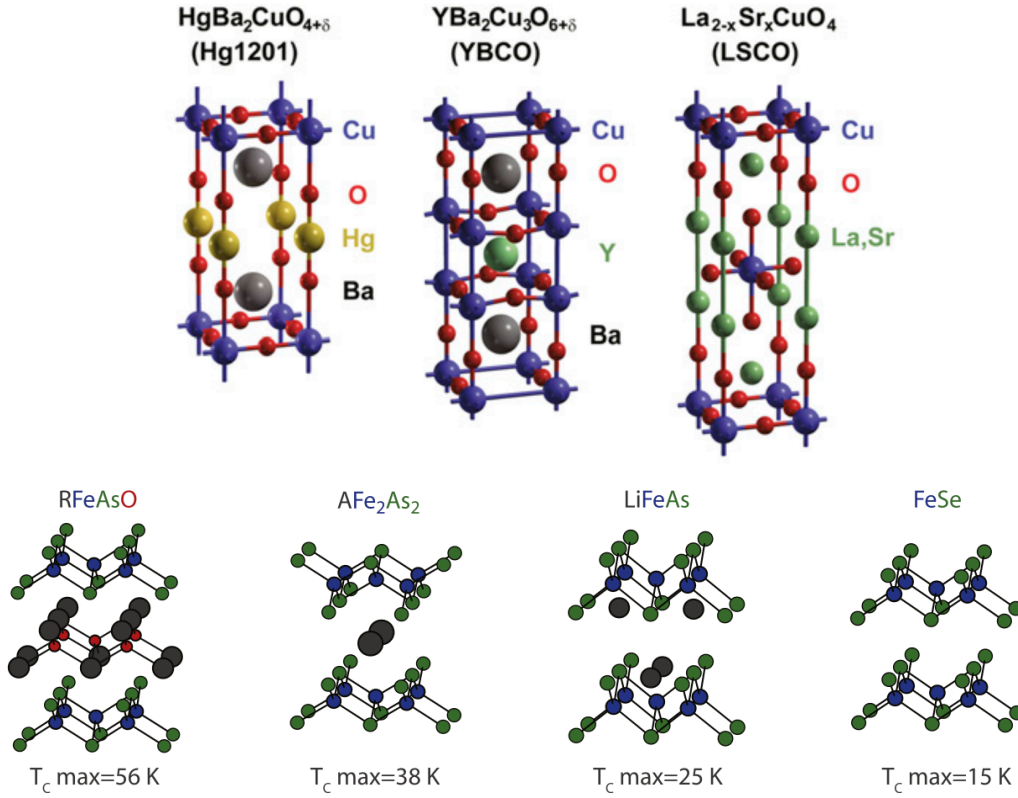
**Figure 1.1:** (Top) The lattice structure and chemical formula for three common copper based superconductors characterized by $CuO_2$ layers. This figure is reproduced from Ref. [6].(Bottom) The lattice structure for the iron based superconductors and their superconducting transition temperatures $T_c$. The left three materials exemplify the 1111, 122 and 111 members of the pnictide family. The green circles are As atoms (pnictides) and the blue are Fe atoms. These form the FeAs layers that characterize these materials. The compound on the far right does not contain As and is a representative of the chalcogenides where here the green circles are Se/Te. This figure is reproduced from Ref. [7]

nearest neighbor Cu's. Fig. 1.3(b) shows the planes of relevance that characterize the iron pnictdes. The Fe atoms form a square lattice with the As atoms in the plane above or below the Fe and located in the center of four Fe ions. In contrast to the cuprates, because the As ions are staggered above and below the Fe plane, the unit cell for the iron pnictdes is $Fe_2As_2$. Although there are physically two Fe per unit cell in the pnictdes, due to glide-mirror symmetry of the lattice, it can be convenient to study systems with a FeAs unit cell [13].
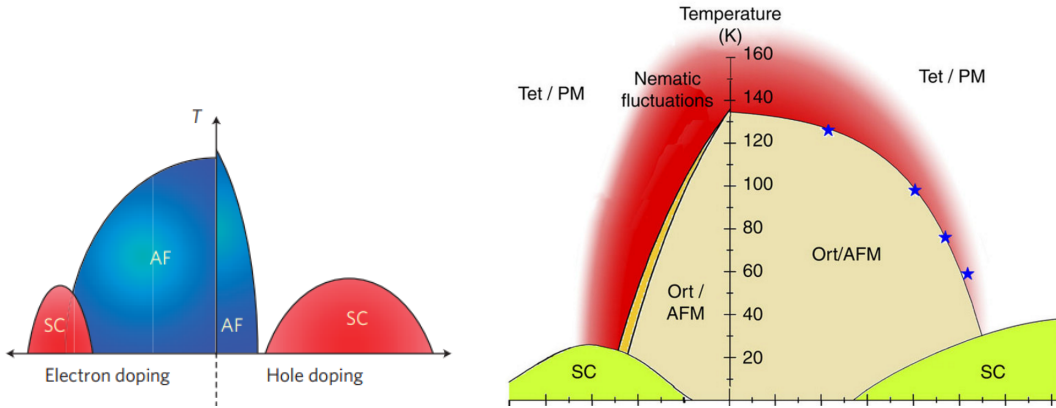


**Figure 1.2:** (Left) A schematic phase diagram for the cuprates. The blue areas denote the checkerboard AFM phase while the red areas indicate the superconducting phase. This figure is reproduced from Ref. [10]. (Right) Schematic phase diagram for 122 pnictdes. Ort/AFM denotes the phase with collinear magnetic order and orthorhombic lattice distortion, SC the superconducting phase,and PM/Tet the paramagnetic and tetragonal phase. In addition, a nematic phase appears upon doping. Tetragonal symmetry is only broken below the nematic/orthorhombic transition line, but nematic fluctuations remain at higher temperatures. This figure is reproduced from Ref. [11].

The undoped cuprates are Mott insulators with a "checkerboard" antiferromagnetic (AFM) phase described by a magnetic structure factor, $S(\vec{Q})$, that peaks at $\vec{Q}=(\pi,\pi)$ (See Fig. 1.3(a)), while the undoped pnictdes are bad metals with a "collinear" AFM state defined by an $S(\vec{Q})$ that peaks at either $\vec{Q}=(\pi,0)$ or $\vec{Q}=(0,\pi)$ (See Fig. 1.3(b)). The $S(\vec{Q})$ is the Fourier transform of the real space spin-spin correlations between spins on each lattice site and can therefore be used to describe long range magnetic order.
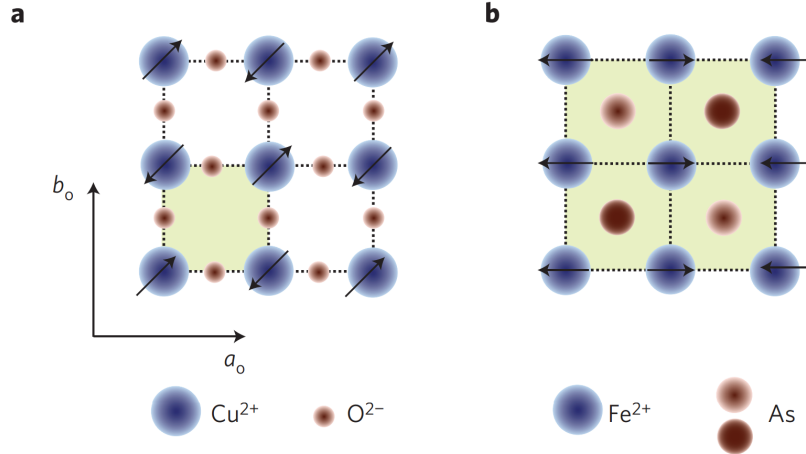
**Figure 1.3:** (a) The copper oxide plane in the cuprate superconductors showing the $\vec{Q}=(\pi,\pi)$, checkerboard AFM order in the Cu spins. The red circles are oxygen ions and are co-planar with the blue Cu ions. (b) The pnictide FeAs plane. The blue circles are Fe ions and the red circles are As ions where the darker (lighter) red circles are the As ions above (below) the Fe plane. The collinear $(\pi,0)$ AFM order is indicated in the Fe spins. This figure is reproduced from Ref. [12]
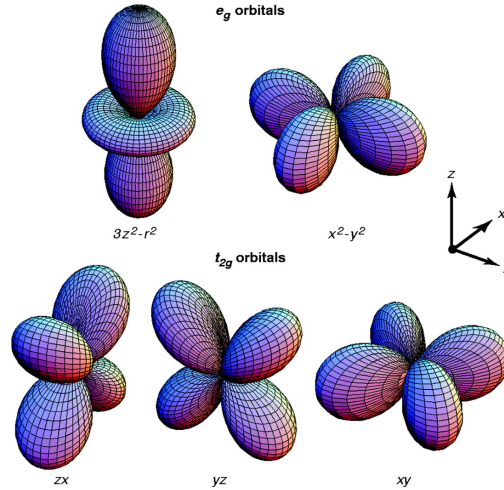


**Figure 1.4:** An illustration of the five d orbitals where the valence electrons in Fe and Cu reside. The orbitals can be separated into two groups: $t_{2g}$ and $e_g$. For Cu the $e_g$ orbitals, particularly $d_{x^2-y^2}$, contain the most weight at the FS while for Fe the $t_{2g}$ orbitals are the ones that form the FS. This figure is reproduced from Ref. [14]

The "base" atoms Cu and Fe are transition metals that have valence electrons occupying their d orbitals which are outlined in Fig. 1.4. LDA calculations and ARPES measurements

have demonstrated that the Cu $d_{x^2-y^2}$ band (See Fig. 1.5(Left)) dominates at the Fermi surface (FS) (See Fig. 1.6(Left)), thus single orbital models have mostly been used to study the cuprates [19, 20]. However, in the case of the pnictides, LDA calculations have shown that several Fe 3d bands hybridize (See Fig. 1.5(Right)) at or near the FS (See Fig. 1.6(Right)) and produce a more complex FS characterized by hole pockets at the center of the Brillouin zone and electron pockets at the X and Y points. Although first principles calculations [16, 21] have shown that the $3d_{xz}$ and $3d_{yz}$ Fe orbitals have the dominant weight at the FS in the Fe-pnictides, there is a non-negligible contribution from the $3d_{xy}$ orbital at the electron pockets, as shown in Fig. 1.6(Right). These orbital contributions have been confirmed by orbital resolved ARPES experiments [22] that use different polarizations to identify the dominant orbital characteristic of the individual bands. The multi-orbital nature of the pnictides greatly increases the complexity for the simplest models needed to describe them.
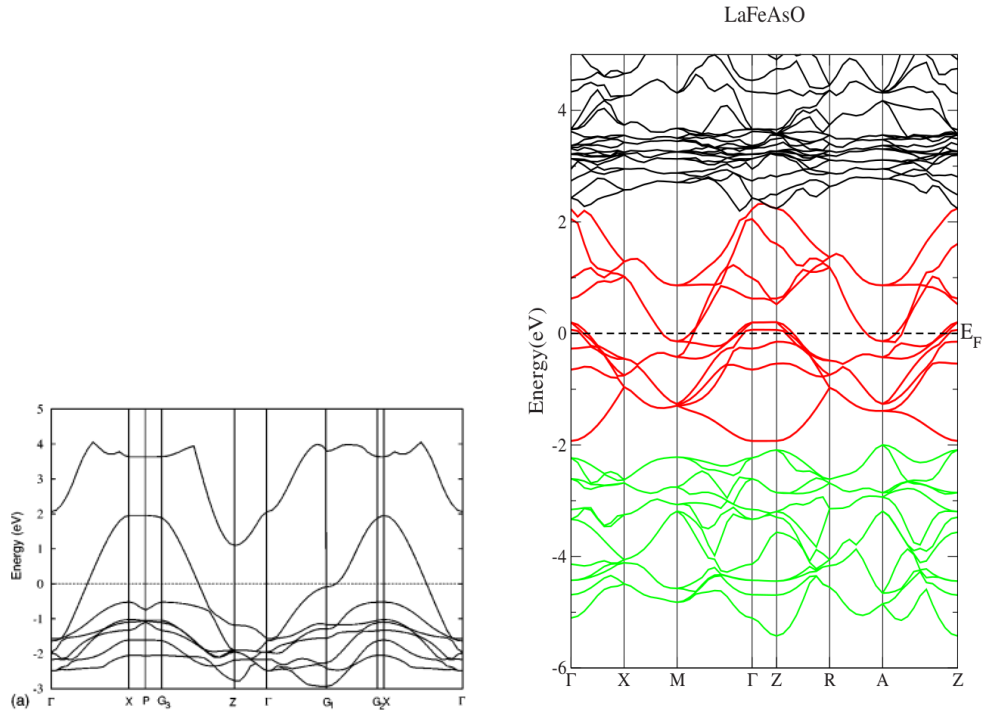


**Figure 1.5:** (Left) The $La_2CuO_4$ band structure from LDA calculations. The band that crosses the Fermi surface has mostly Cu $3d_{x^2-y^2}$ character. This figure is reproduced from Ref. [15]. (Right) Band structure of LaFeAsO from First Principles calculations. The red and green bands have mainly Fe 3d and pnictogen/oxygen p characters, respectively. This figure is reproduced from Ref. [16]

6
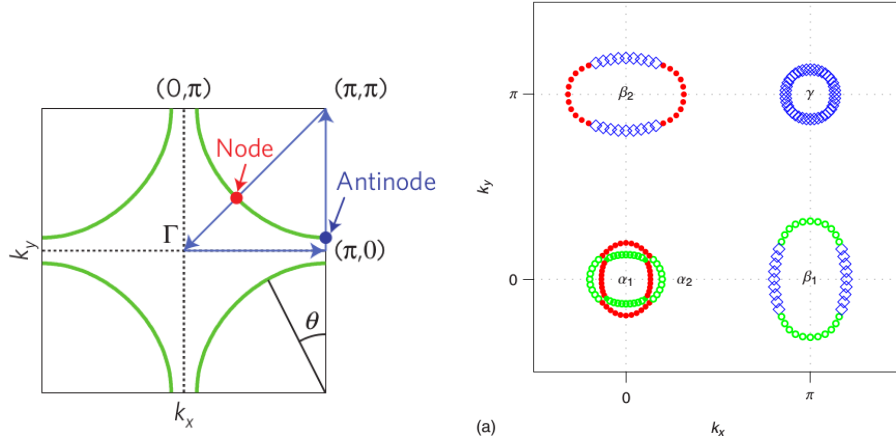
**Figure 1.6:** (Left) Fermi Surface for the cuprates calculated in a one band Hubbard model. This figure is reproduced from Ref. [17]. (Right) Fermi Surface for the pnictides calculated in a five orbital tight-binding model. This figure is reproduced from Ref. [18]. The blue, red, and green represents the $d_{xy}$, $d_{xz}$, and $d_{yz}$ orbitals respectively.
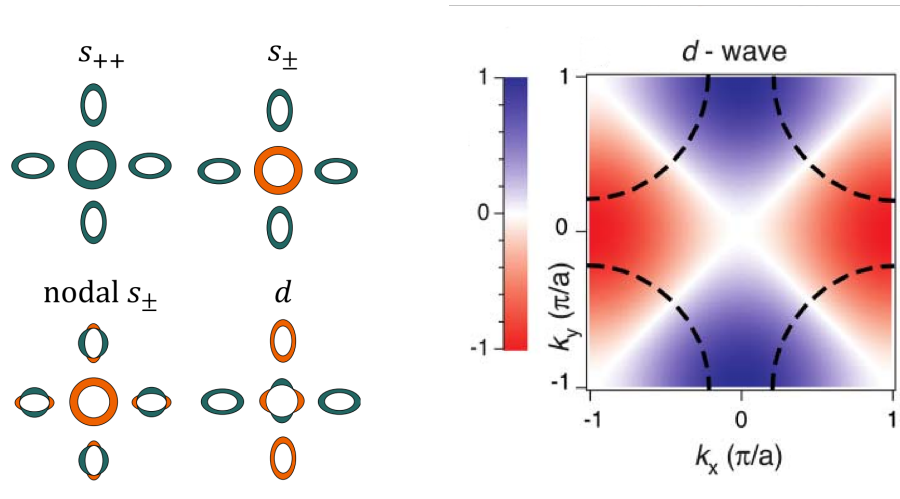


**Figure 1.7:** (Left) An illustration of four examples of proposed pairing symmetries for the iron pnictides. The colors (green/orange) represent the sign (+/-) of the superconducting gap function. This figure is reproduced from Ref. [23]. (Right) An illustration of the d-wave pairing symmetry for the cuprates where the red/blue color represents the sign of the superconducting gap function. This figure is reproduced from Ref. [24].

It is not yet known if superconductivity in both families of materials has the same origin. Electron-phonon interactions as in BCS appear to be insufficient to overcome the Coulomb repulsion in the cuprates and it is believed that magnetism plays a role [12]. This leads to a

peculiar SC gap that usually contains nodes in which the gap function changes sign at the FS. Thus, instead of the uniform S-wave gap of BCS materials, the SC gap in the cuprates has nodes at $(\pm\frac{\pi}{2},\pm\frac{\pi}{2})$ and D-wave symmetry. The pairing symmetries in superconductors can be characterized by the sign of the gap function. Examples for the proposed pairing symmetries for the cuprates and pnictides are shown in Fig. 1.7. The pairing symmetry in the cuprates has been proven to be D-wave [25], but in the pnictides this is still an area of controversy. $S^{+/-}$ and D-wave pairing symmetries have been proposed [23] as a result of the magnetic/Coulomb interactions that are supposed to lead to D-wave pairing in the cuprates, while $S^{++}$ pairing [26], is the result of the standard electron-phonon interactions in multi-orbital systems. Despite the multiple experiments that have studied the pairing symmetries of the pnictides [27, 28, 29], the results are still controversial due to the variety of materials in the family, the difficulty to distinguish $S^{++}$ from $S^{+/-}$ symmetries, and the possibility of nodeless D-wave gaps under certain conditions.

It is important to notice that both families of materials also undergo a structural transition. In the pnictides the Fe ions form a tetragonal arrangement, which becomes orthorhombic for temperatures below T$_S$ (See Fig. 1.2(Right)). This transition is very relevant in the pnictides because it breaks the degeneracy between the $\vec{Q}=(\pi,0)$ and $\vec{Q}=(0,\pi)$ collinear states, and the $d_{xz}$ and $d_{yz}$ orbitals. The structural transition from tetragonal to orthorhombic also occurs in the cuprates, but it is not as relevant as in the pnictides because the cuprates have a $\vec{Q}=(\pi,\pi)$ magnetic state which is not affected by the lattice distortion. As can be seen in the phase diagram shown in Fig. 1.2(Right)), for the pnictides $T_N$ may occur above $T_N$. In fact for several different concentrations of doping for the "122" compounds and in the "1111" compounds [30] this is the case. Early experiments [9, 30] had discovered a resistance anomaly associated with this structural transition, and the existence of a nematic phase of electronic origin [31] was proposed shortly after. Experimentally the nematic phase has been studied through in-plane resistivity measurements along the two perpendicular lattice vectors [32]. Due to the small lattice distortion in the orthorhombic phase (on the order of $\delta = (a_x - a_y)/(a_x + a_y) \sim 0.003$), the lattice is not expected to be the driver of the resistance anomaly [33, 34]. Here $\delta$ is the order parameter describing the orthorhombic distortion and $a_x$ ($a_y$) is the average Fe-Fe distance in the $\hat{x}$ ($\hat{y}$) direction. For

this reason it has been suggested that the nematic state may be driven by the spin degrees of freedom [31, 35, 36] or by the orbital ones [26, 34, 37, 38]. The idea is that the "driver" of the nematic phase may be the DOF that also drives superconductivity due to the proximity of the nematic and superconducting phases. However, complexities in experiments (with external strain required to detwin crystals) and in the theoretical approaches (multiorbital models, intermediate correlations regimes) have prevented the identification of a primary driver of the nematic state.

The so-called "magnetic" scenario for the nematic state proposes that the magnetic long-range order in iron pnictides develops in two stages (See Fig. 1.8): the Ising $Z_2$ symmetry is broken when the short-range degeneracy of the $\vec{Q}=(\pi, 0)$ and $\vec{Q}=(0,\pi)$ AFM states is lifted at $T_S$ and the O(3) symmetry is broken when the spins develop long rang order favoring a direction in spin space [35]. From a magnetic point of view the nematic phase is described by the broken $Z_2$ symmetry while the system remains paramagnetic, and the rotational O(3) symmetry remains unbroken. In the orbital driven scenario the $d_{xz}/d_{yz}$ symmetry is broken inducing the structural transition at $T_S$ via an orbital-lattice coupling and before the long-range magnetic order develops at $T_N$. As pointed out above, the importance of understanding which degree of freedom drives this transition is that it may unveil which DOF is responsible for the superconducting mechanism due to the proximity of the nematic and SC phases.
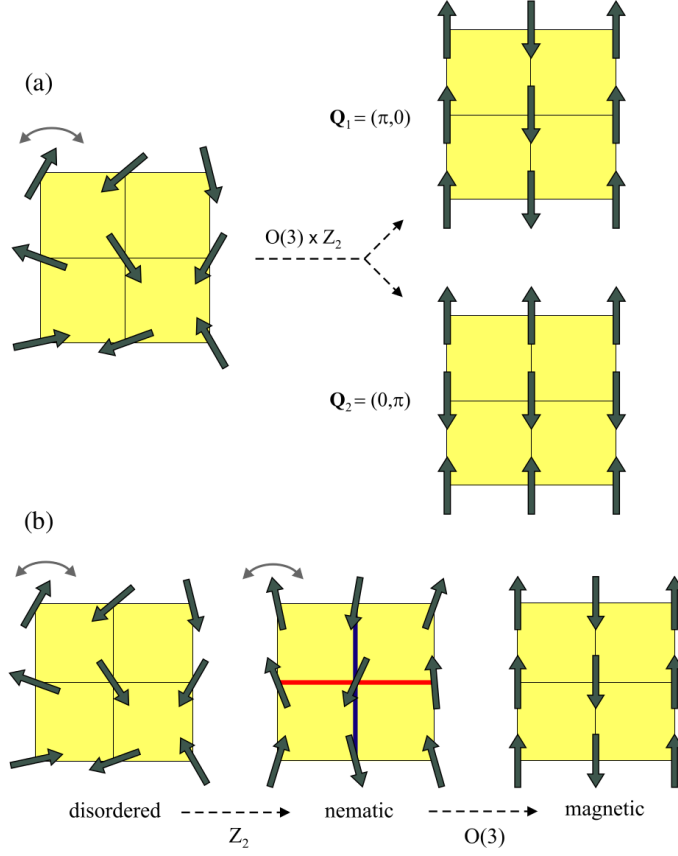
**Figure 1.8:** Schematic representation of the magnetically driven nematic transition in real space. (a) The transition from the disordered phase to the AFM phase breaks an O(3) x $Z_2$ symmetry. The O(3) symmetry encompasses the rotations in spin space while the $Z_2$ (Ising) symmetry involves the two degenerate ground states of magnetic stripes with parallel spins along the y axis (ordering vector $Q_1 = (\pi,0)$) or along the x axis (ordering vector $\vec{Q_2} = (0,\pi)$). (b) The O(3) x $Z_2$ symmetry can be broken in two steps. First, only the $Z_2$ symmetry is broken, but the system is still paramagnetic (indicated by the gray double arrow on top of the spins). In the second step, the O(3) symmetry is broken and the system acquires long-range magnetic order. This figure is reproduced from Ref. [35].

## 1.3 Properties of Iron Chalcogenides

Another exciting development in the study of Fe-based superconductors was the discovery of superconductivity in the iron chalcogenides such as $FeSe_xTe_{1-x}$ [39]. As mentioned previously, understanding how these materials compare to the other high temperature superconductors is crucial to the development of a generalized theory that explains this phenomenon. As can be seen in Fig. 1.1(Right), the chalcogenides are characterized by

iron/chalcogen planes with the chalcogens being S, Se, or Te [40]. The chalcogenides have the simplest structures and the highest $T_c$ of all the FeSC. They share some properties with the pnictides. For example, at high temperatures the iron chalcogenides develop the same tetragonal PbO-type structure (staggered chalcogenide atoms in/out of the Fe plane) as the FeAs layers in the pnictides, and a similar Fermi surface. However the parent compound, FeTe, has unique properties. Its lattice undergoes a monoclinic distortion upon cooling [41, 42, 43](See Fig. 1.9(Top-Left)). This structure is puzzling because it does not seem to result from FS nesting as in the collinear state of the pnictides. Upon doping the parent compound, FeTe, with Se, a rich phase diagram that includes superconductivity is observed. When Te is completely replaced by Se, the material FeSe is superconducting, but the optimal superconductivity occurs near $FeTe_{0.5}Se_{0.5}$ [41](See Fig. 1.9(Bottom)). The magnetic order of FeTe is also different from the pnictides because the high temperature paramagnetic state undergoes a transition to long range "bicollinear" AFM order shown in Fig. 1.9(Top-Right)). The bicollinear AFM order can be described by a structure factor that peaks at $\vec{Q} = \pm(\frac{\pi}{2}, \pm\frac{\pi}{2})$ which are not nesting vectors in the Brillouin zone.

A puzzling characteristic of superconducting FeSe is that it goes through an orthorhombic structural transition at $T_S \sim 90$ K and develops superconductivity at $T_c \sim 8$ K. The material appears to be in a nematic state for $T_S > T > T_c$, although the collinear AFM state has not been observed in any region of the phase diagram of $FeSe_x Te_{1-x}$ (at ambient pressure).

## 1.4 Relevant Degrees of Freedom in the Fe-Based Superconductors

One of the goals of this manuscript is to identify the degrees of freedom that drive the properties of the FeSC in the intermediate interaction regime. The spin, charge, orbital, and even lattice DOF are all active in the actual materials. The role that each DOF plays is a subject of debate. It is necessary to unveil the minimum number of DOF that a model should contain in order to describe the relevant properties of the material. Since the cuprates are Mott insulators with mostly one active orbital at the FS, strong coupling, single band
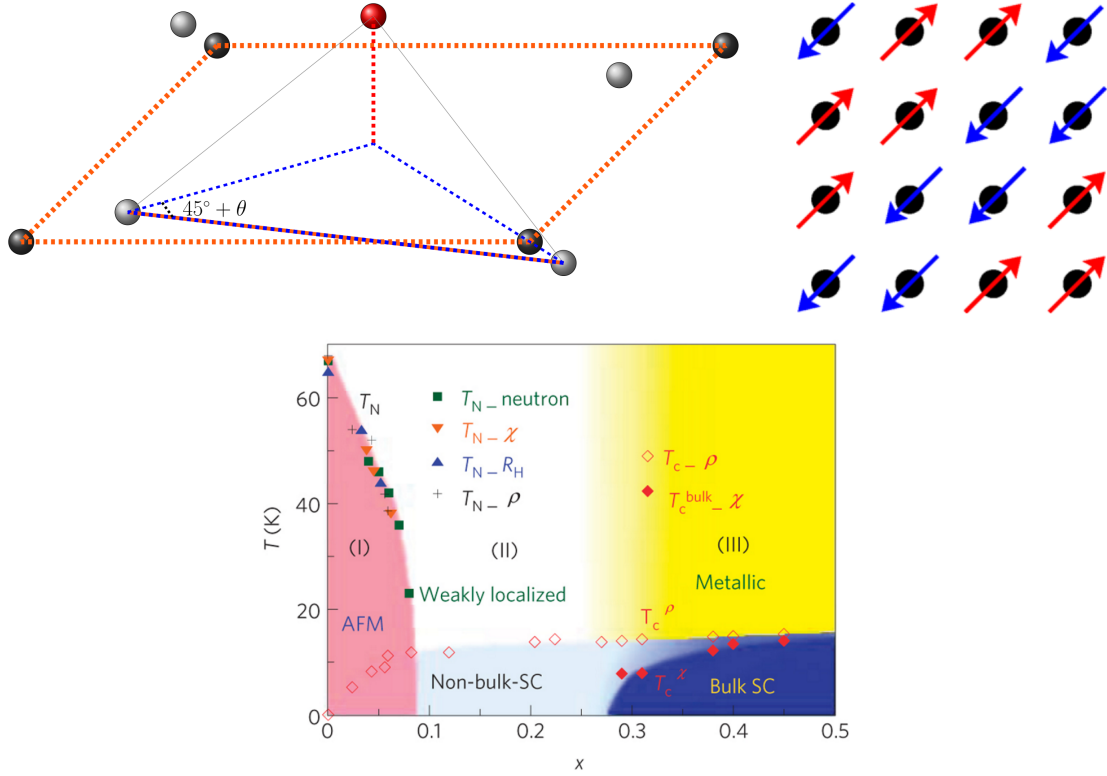
**Figure 1.9:** (Top-Left) Schematic description of the tetragonal to monoclinic distortion in FeTe where the Fe-Fe distance along the diagonals are elongated in one direction and shortened in the other. The red circles indicate Te, Fe in the tetragonal structure is indicated by light-gray circles and dark-gray circles denote the position of the Fe in the monoclinic phase. (Top-Right) Bicollinear Magnetic order. (Bottom) The phase diagram temperature (K) vs Se doping for FeTe$_{1-x}$Se$_x$. This figure is reproduced from Ref. [42].

models are used to describe many of their properties [44]. However, the iron pnictides are more complex, with several active orbitals and in an intermediate Coulomb regime [12]. Thus, the models that were successful for the cuprates cannot be used for the pnictides. When materials are in an intermediate regime it is imperative that numerical tools are developed to complement the traditional calculations performed in the easier to study strong and weak coupling limits. Numerical studies are the most useful tool to obtain unbiased results. This is the approach that will be followed in this manuscript with the goal to propose models with the minimum number of DOF that capture the observed physical behaviors.

The success of the first principles calculations stated previously [16, 21] led some scientists to believe that the properties of the pnictides could be obtained from weak coupling approaches. In fact, the collinear AFM state of the parent compounds of the pnictides can be guessed from the nesting of their Fermi surface [45]. However, other authors succeeded in reproducing the magnetic properties of the pnictides using strong coupling approximations by studying models with localized magnetic moments [46, 47, 48]. Super-Exchange spin models can be studied numerically [46, 47] and with mean field (MF) techniques [48] and including nearest neighbor and next-nearest neighbor Heisenberg parameters they can reproduce the observed collinear magnetic behavior of the pnictides. However, these models are insulating and fail to describe the metallic parent compounds. The rational for studying this limit is the experimental observation of localized magnetic moments even at room temperature and the existence of insulating states in some regions of the phase diagrams of some Cu-doped pnictides and layered chalcogenides [49, 50]. However, it has been shown that both itinerant electrons as well as localized magnetic moments [51, 52, 53] are present in the Fe based superconductors indicating that they are in an intermediate coupling regime.

The standard models proposed to describe the FeSC are multiorbital Hubbard models that include the on-site Coulomb interactions $U(intraorbital)$, $U'(interorbital)$, and $J(Hund)$ [54]. The tight binding multiorbital term can be obtained via Slater-Koster techniques [55] for a number of d-like orbitals that ranges from two [55] to five [18], and the

interaction term is given by [56] :

$$H_{int} = U \sum_{\mathbf{i},\alpha} n_{i,\alpha,\uparrow} n_{i,\alpha,\downarrow} + (U' - J/2) \sum_{\mathbf{i},\alpha<\beta} n_{i,\alpha} n_{i,\beta}$$

$$-2J \sum_{\mathbf{i},\alpha<\beta} \mathbf{S}_{\mathbf{i},\alpha} \cdot \mathbf{S}_{\mathbf{i},\beta} + J \sum_{\mathbf{i},\alpha<\beta} (d^\dagger_{\mathbf{i},\alpha,\uparrow} d^\dagger_{\mathbf{i},\alpha,\downarrow} d^\dagger_{\mathbf{i},\beta,\downarrow} d^\dagger_{\mathbf{i},\beta,\uparrow} + H.c), \tag{1.1}$$

where $U$ is the on-site Coulomb repulsion for electrons in the same orbital, $U'$ is the Coulomb repulsion of electrons on the same site but in different orbitals, and $J$ is a ferromagnetic Hund coupling between electrons on the same site. The indices $\alpha$, $\beta$ denote the orbitals (xz, yz) in a minimal two orbital model [55], xy is added for a three orbital model [56], and the five d orbitals are included in the five orbital case [18]. The operator $d^\dagger_{\mathbf{i},\alpha,\sigma}$ creates an electron with spin $\sigma$ on site $\mathbf{i}$ in orbital $\alpha$, $n_{i,\alpha,\sigma} = d^\dagger_{\mathbf{i},\alpha,\sigma} d_{\mathbf{i},\alpha,\sigma}$ is the electronic number operator, and $\mathbf{S}_{\mathbf{i},\alpha}$ is the spin in orbital $\alpha$ at site $\mathbf{i}$ given by $d^\dagger_{\mathbf{i},\alpha,a} \vec{\sigma}_{a,b} d_{\mathbf{i},\alpha,b}$ where $\vec{\sigma}_{a,b}$ are the Pauli matrices. Due to the presence of four fermion operators in these terms, exact calculations can be performed only for two orbitals in an 8-site cluster [55].

It is crucial to develop multiorbital models that can be studied with unbiased numerical simulations in larger lattices. The first principles calculations mentioned previously showed that the $3d_{xz}$ and $3d_{yz}$ orbitals have the highest density of states at the FS, and a minimum model must include at least these two orbitals. Two-orbital models with the Coulomb interactions given by Eq. 1.1 can be solved exactly only in small lattices (8 sites) or via mean field (MF) approximations [55]. These models have successfully provided the metallic, magnetic ground state as well as a reasonable FS for the pnictides [57, 58]. However, calculations using only two-orbitals have been criticized because they failed to include the $3d_{xy}$ orbital that has a non-negligible weight at the electron pockets in the FS and could not capture the correct band structure at several points in the Brillouin Zone such as the Γ-point. Therefore, it is accepted that the minimum number of itinerant orbitals to describe the pnictides is three. For this reason, three-orbital models were developed [56].

Unlike the two orbital model, the three orbital model only can be studied using MF techniques because the addition of the extra orbital makes exact calculations unfeasible due to limitations in computer memory. Using MF techniques, orbital and magnetic ordering in

the ground state and a FS that matched the first principles calculations for the pnictides were obtained [56]. With this model, the optical conductivity was calculated [59], showing the resistance anisotropy between the ferromagnetic and AFM directions that have been observed experimentally [60]. While this model reproduces many important properties of the pnictides, its study is restricted to low temperatures where the MF calculations can be performed and the region near the structural transition, that is important to understand the nematic phase, cannot be accessed. Because of the limitations of exact diagonalization and MF calculations for the three orbital model mentioned above, a three orbital spin fermion model [61] was proposed for the pnictides that can be studied numerically in large clusters at finite temperatures.

## 1.5  Spin Fermion Model

For decades prior to the discovery of the iron pnictides, double exchange models had been developed to study materials with itinerant and localized DOF [62]. The lattice-Kondo model, which includes a tight-binding Hamiltonian to describe the itinerant electrons and a Hund coupling term to couple the itinerant and localized electrons [63], was developed as a fully quantum model to study transition metal-oxides such as the manganites. Treating the localized spins as classical fields that could be treated with classical Monte Carlo techniques was later proposed [64, 65, 66], opening the possibility of studying the quantum system in large lattices and at any temperature. The classical treatment of the localized spins replaces the four-fermion interaction terms in the Hamiltonian by two-fermion ones, so that the problem can be numerically studied in a single particle framework. Because of the success of this "spin-fermion" approach in the lattice-Kondo model to study the manganites [65, 66], a spin fermion model was later developed to study the cuprates [19]. When the pnictides were found to be in the intermediate coupling regime and it was discovered that they contain both itinerant and localized DOF, spin fermion models were developed for these materials [52, 57, 61]. The following Chapters of this manuscript will be devoted to the presentation of numerical results obtained from various adaptations of spin fermion models which are described in detail in the corresponding chapters. The base Hamiltonian for the

pnictides is presented in Appendix A. In chapters Ch. 4 and Ch. 5 the addition of spin and orbital couplings to monoclinic distortions to describe properties of the chalcogenides will be discussed.

In this dissertation, various adaptations of the spin-fermion model will be developed with the goal to understand, reproduce, and predict properties of the Fe-based superconducting pnictides and chalcogenides. The terms added to the spin-fermion model Hamiltonian, as well as novel numerical techniques developed for their study, will be described in the following chapters. Ch. 2 is devoted to the understanding of the puzzling behavior of the nematic susceptibility observed in experiments on $Ba(Fe_{1-x}Co_x)_2As_2$ under uniaxial pressure [67]. Via a Ginzburg-Landau analysis and Monte Carlo simulations of the spin-fermion model with a tunable axial strain affecting the spin/orbital/lattice interactions, the experimental susceptibility is reproduced and its features interpreted. Ch. 3 is devoted to understanding how nemacity develops with doping in materials of the 122 family. Our numerical calculations demonstrate that the phenomenon develops due to the introduction of non-magnetic impurities in the Fe-As planes as opposed to the loss of FS nesting due to electronic doping as proposed in the weak coupling regime. The last two chapters present the studies performed for the chalcogenides. An explanation of the origin of the bicollinear long-range magnetic order observed in FeTe, the parent compound of the superconductor $FeTe_{1-x}Se_x$, is presented in Ch. 4 while the possible existence of a bicollinear nematic state in iron chalcogenides is demonstrated based on analytical and numerical grounds in Ch. 5. Additional technical aspects are presented in Appendices A to I.

# Chapter 2

# Study and Explanation of the Features of the Magnetic Susceptibility Under Uniaxial Pressure in BaFe$_2$As$_2$

This chapter is a modified version of PHYSICAL REVIEW B 90, 184507 [68, 69].

## 2.1 Introduction

As discussed previously in Sect. 1.4, the complexity of high critical temperature iron-based superconductors [12, 70], with coupled spin, charge, orbital, and lattice degrees of freedom, creates exotic regimes such as the widely discussed nematic state with broken rotational invariance [60, 71, 72]. This state may originate in the spin [31, 36, 73, 74, 75] or in the orbital [33, 34, 38, 76, 77, 78] degrees of freedom, but subtleties in experiments (with strain required to detwin crystals) and in theory (employing complicated multiorbital models) have prevented the identification of the primary driver of the nematic regime.

Previous efforts to study nematicity have considered spin fermion models with electrons coupled to the lattice [79]. These studies unmasked a considerable electron-lattice feedback, that led to several results in agreement with experiments, such as anisotropic resistivities

17

and a nematic and structural (tetragonal-orthorhombic) transition at $T_S$, slightly separated from the Néel temperature $T_N$ ($< T_S$) [80]. This nematic phase is similar to the results for the 1111 parent compound LaFeAsO, however, experiments have shown that the transition temperatures are simultaneous in the 122 parent compound $BaFe_2As_2$. Despite the fact that $T_S = T_N$ for this material, experiments have shown the existence of nematic fluctuations under strain [60, 71].

More recently, a remarkable experimental development was the report of a diverging nematic susceptibility $\chi^{exp}$ vs. temperature $T$, with a mysterious characteristic temperature scale $T^*$, for single crystals of $Ba(Fe_{1-x}Co_x)_2As_2$ [67] measured by varying an *in-situ* uniaxial strain. Although contrasting $\chi^{exp}$ against theory and explaining the physical meaning of $T^*$ are crucial aspects to identify the mechanism that drives nematicity, $\chi^{exp}$ and $T^*$ had not been addressed theoretically before since temperatures above $T_S$ are difficult to study with reliable methods.

In this Chapter results where, this nematic susceptibility was theoretically calculated for the first time, via the spin-fermion model coupled to the lattice in precisely the same setup as in Ref. [67] are reported. Note that this susceptibility, which tests a local geometric property of an enlarged parameter space, is *different* from the simpler magnetic susceptibility calculated in Ref. [79] obtained from thermal statistics. The present computational effort required an order of magnitude more work than in Ref. [79] because the strain is an extra parameter to vary, rather than being dynamically adjusted in the Monte Carlo (MC) process as before. To implement this demanding task, modifications in the MC algorithm were introduced, as explained in Sec. 2.3. Compared to Hubbard multiorbital approaches, a unique characteristic of the spin-fermion model is that simulations can be carried out for a wide range of finite temperatures, including the nematic regime above the ordering temperatures. This is due to the classical approximation of the localized spins that enables the Hamiltonian to be described by single particle states, greatly reducing the size of the matrix, and now the Hamiltonian can be exactly diagonalized. Remarkably, our susceptibility is very similar to the diverging experimental $\chi^{exp}$ result. Moreover, we observed that the $T^*$ scale in the Curie-Weiss behavior is the preexisting Néel critical temperature of the purely electronic sector,

18

which is independent of the lattice. We also observed a density-of-states pseudogap and nematic fluctuations above $T_S$, caused by short-range $(\pi,0)$-$(0,\pi)$ antiferromagnetic order.

This Chapter is organized as follows: the model is introduced in Section 2.2; the many-body techniques developed for this work as well as the main results are presented in Section 2.3; the results for the spin-nematic and orbital-nematic susceptibilities are analyzed in Section 2.4, while the dependence on the structural transition temperature with the orbital-lattice coupling is discussed in Section 2.5. The analysis of the spin structure factors and the pseudogap in the density of states is presented in Section 2.6. Section 2.7 is devoted to the conclusions. The full Hamiltonian is provided in Appendix A, the numerically guided Ginzburg-Landau (GL) calculations appear in Appendix B. Appendix C contains the comparison between total and partial derivatives at the critical temperature $T_S$, and numerical results for an unphysically large value of the lattice-orbital coupling are presented in Appendix D.

## 2.2  Models

The model employed here combines the purely electronic spin-fermion model [52, 57, 61, 82] together with lattice orthorhombic distortions:

$$H_{\mathrm{SF}} = H_{\mathrm{Hopp}} + H_{\mathrm{Hund}} + H_{\mathrm{Heis}} + H_{\mathrm{SLO}} + H_{\mathrm{OLO}} + H_{\mathrm{Stiff}}. \qquad (2.1)$$

This (lengthy) full Hamiltonian is provided in detail in Appendix A. $H_{\mathrm{Hopp}}$ is the Fe-Fe hopping of the $d_{xz}$, $d_{yz}$, and $d_{xy}$ electrons (a three orbital model is used with an electronic bandwidth $W \sim 3$ eV), with amplitudes that reproduce photoemission results [22, 61]. The average number of electrons per itinerant orbital is $n=4/3$ [56], i.e. the undoped regime will be our focus. This is reasonable since many experiments that address the nematic state are carried out for the parent compounds. Moreover, technically the study simplifies in the absence of doping and quenched disorder.

The Hund interaction is canonical: $H_{\mathrm{Hund}}=-J_{\mathrm{H}} \sum_{\mathbf{i},\alpha} \mathbf{S_i} \cdot \mathbf{s_{i,\alpha}}$, with $\mathbf{S_i}$ ($\mathbf{s_{i,\alpha}}$) the localized (itinerant with orbital index $\alpha$) spin. $H_{\mathrm{Heis}}$ is the Heisenberg interaction among the localized

spins involving nearest-neighbors (NN) and next-NN (NNN) interactions with couplings $J_{\text{NN}}$ and $J_{\text{NNN}}$, respectively, and ratio $J_{\text{NNN}}/J_{\text{NN}}=2/3$ [61] to favor collinear order.

Within the spin-driven scenario for nematicity, the state between $T_N$ and $T_S$ is characterized by short-range spin correlations that have as an order parameter $\Psi_{\mathbf{i}}=\sum_{\pm}(\mathbf{S_i}\cdot\mathbf{S_{i\pm y}}-\mathbf{S_i}\cdot\mathbf{S_{i\pm x}})/2$ that satisfy $\langle\Psi\rangle>0$ [36, 83], where $\mathbf{S_i}$ is the spin of the iron atom at site $\mathbf{i}$ and $\mathbf{x},\mathbf{y}$ are unit vectors along the axes. As described in Appendix A the $\mathcal{O}_{rth}$-distortion $\epsilon_{66}(\mathbf{i})$ associated to the elastic constant $c_{66}$ [81] will be considered here. The coupling of the spin-nematic order and the lattice is $H_{\text{SLO}}=-g_{66}\sum_{\mathbf{i}}\Psi_{\mathbf{i}}\epsilon_{66}(\mathbf{i})$ [36, 75], where $g_{66}$ is the lattice-spin coupling [84]. To also incorporate orbital fluctuations, the term $H_{\text{OLO}}=-\lambda_{66}\sum_{\mathbf{i}}\Phi_{\mathbf{i}}\epsilon_{66}(\mathbf{i})$ is added, where $\lambda_{66}$ is the orbital-lattice coupling, $\Phi_{\mathbf{i}}=n_{\mathbf{i},xz}\text{-}n_{\mathbf{i},yz}$ is the orbital order parameter, and $n_{\mathbf{i},\alpha}$ the electronic density at site $\mathbf{i}$ and orbital $\alpha$ [33, 34]. Finally, $H_{\text{Stiff}}$ is the spin stiffness given by a Lennard-Jones potential that speeds up convergence as described in Appendix A.

Here it must be noted that the lattice, spin-nematic, and orbital order parameters all transform as the $B_{1g}$ representations of the $D_{4h}$ point group (See Fig. 2.1). Taking the basis as along the Fe-Fe directions with the $\hat{z}$ axis out of plane, $B_{1g}$ transformations can be described by $\frac{\pi}{2}$ rotations about the $\hat{z}$ axis that lead to a change of sign in the order parameter (see Eq. A.8, A.9, and A.13). Since each term couples two of these order parameters that both have $B_{1g}$ symmetry, the overall Hamiltonian is rotationally invariant.
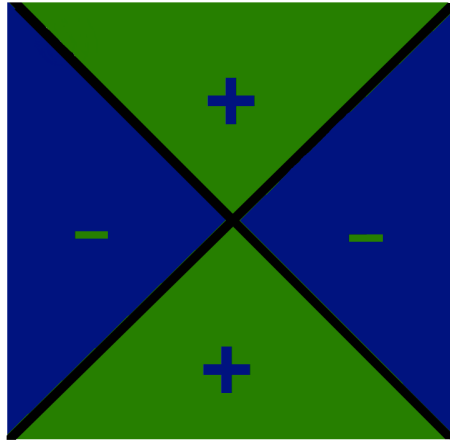


**Figure 2.1:** Example of the $B_{1g}$ representation of the $D_{4h}$ group.

## 2.3 Many-body techniques and main results

The details of the Monte Carlo method used in our study can be found in Ref. [82] and Ch. 7 of Ref. [85]. However, here an extra computational component had to be introduced because, compared with Ref. [79], for each temperature $T$ now the strain was varied as an extra parameter. Since for each temperature typically 15 values of strain were used, this effort is $\sim$15 times more costly than in Ref. [79]. While the standard Monte Carlo is time consuming because of the fermionic-sector exact diagonalization (ED) at every step, in the related double-exchange models for manganites an improvement has been used before: the "Traveling Cluster Approximation" (TCA) (See Ref. [86] and Ref. [87]), where the MC updates are decided employing a cluster centered at site $\mathbf{i}$ but with a size substantially smaller than the full lattice size [88]. In addition, twisted boundary conditions (TBC) were also used (See Ref. [89] and Ref. [61]). In fact, this is the first time that TCA and TBC are employed together. To simplify further the analysis, most couplings are fixed to values that were used successfully before [61]: $J_{\mathrm{H}}$=0.1 eV, $J_{\mathrm{NN}}$=0.012 eV, and $J_{\mathrm{NNN}}$=0.008 eV. Dimensionless versions of the electron-lattice couplings are constructed via the definitions $\tilde{g}_{66} = 2g_{66}/\sqrt{kW}$ and $\tilde{\lambda}_{66} = 2\lambda_{66}/\sqrt{kW}$ [90], as discussed in the supplementary material of Ref. [79]. Here, $W = 3$ eV is the electronic bandwidth and $k$ regulates the spin stiffness, as shown in Appendix A. These dimensionless constants are fixed to the values 0.16 and 0.12, respectively, that before were found to be realistic [79]. However, results for other values of these couplings are provided in Appendix D.

The spin nematic susceptibility calculated here is defined as $\chi_s = \frac{\partial \Psi}{\partial \epsilon_{66}}|_{\epsilon_0}$, where $\epsilon_0$ is the value of the lattice distortion obtained from the "unrestricted" numerical simulation, and the lattice is equilibrated together with the spins, as in Ref. [79]. To calculate the susceptibility $\chi_s$ of our model, a procedure similar to the experimental setup was employed: the spin nematic order parameter $\Psi$ was measured at various temperatures and at *fixed* values of the lattice distortion $\epsilon_{66}$=$(a_x - a_y)/(a_x + a_y)$. Henceforth, this procedure will be called "restricted" MC (note that this dimensionless $\epsilon_{66}$ should not be confused with the dimensionful $\epsilon_{66}(\mathbf{i})$ used in the Hamiltonian and defined in Appendix A). By this procedure, $\Psi(\tilde{g}_{66}, \tilde{\lambda}_{66}, T, \epsilon_{66})$ are
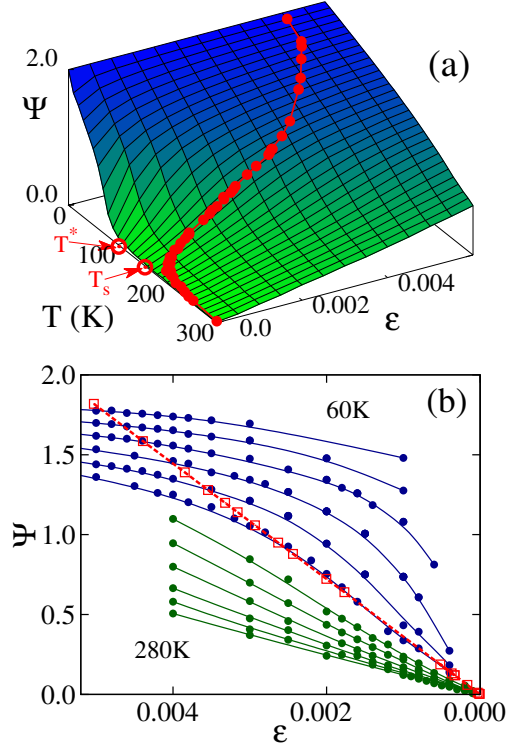
**Figure 2.2:** Monte Carlo spin-nematic order parameter, at $\tilde{g}_{66}=0.16$ and $\tilde{\lambda}_{66}=0.12$. (a) $\Psi$ vs. $T$ and $\epsilon_{66}$, measured at a fixed lattice distortion $\epsilon_{66}$ for each temperature (restricted MC). Shown are the $T^*$ (see text) and $T_S$ ($\sim T_N$) temperatures. Data are for an $8\times8$ cluster with TCA+TBC (PBC $8\times8$ clusters with ED give similar results). Red points are the equilibrium values using unrestricted MC with ED and PBC $8\times8$ clusters. (b) $\Psi$ vs. $\epsilon_{66}$ at fixed temperatures, illustrating their nearly linear relation in unrestricted MC (red), and also the linear slopes of the restricted MC curves (green/blue) close to $T_S$. Results are obtained with ED/PBC $8\times8$ clusters. Note that the number of green/blue points vastly outnumbers the number of red points, highlighting how much more demanding this effort has been than in Ref. [79].
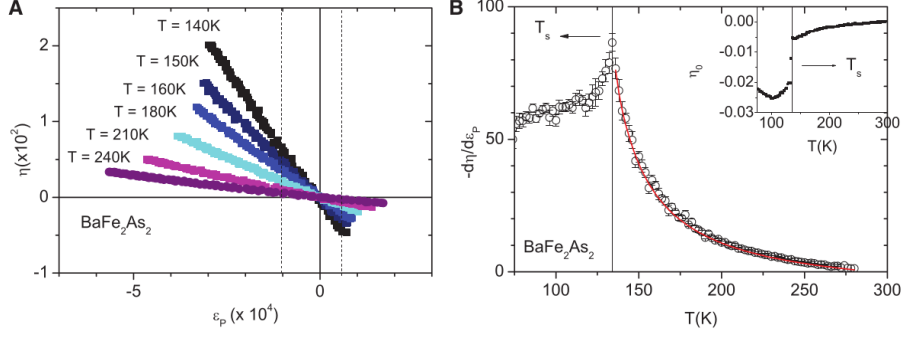
**Figure 2.3:** (A) This figure demonstrates the relative change in resistivity anisotropy as a function of applied strain. These results are for the parent compound $BaFe_2As_2$. (B) This figure demonstrates the temperature dependence of the nematic response which is the derivative of the results from figure (A) but across a wider range of temperatures. The red line is the fit to equation $\frac{d\eta}{d\epsilon_{66}} = \frac{\lambda_{66}}{a_0(T-T^*)+3b\eta^2} + \chi_0$ that is obtained form a Curie-Weiss formulism. Figures (A) and (B) are reproduced from Ref. [67].

obtained at fixed couplings, defining surfaces as those shown in Fig. 2.2(a). Allowing the lattice to relax, the equilibrium curve that is shown with red points in Fig. 2.2(a) is obtained.

Figure 2.2(b) contains the (restricted) MC measured spin-nematic order parameter versus the (fixed) lattice distortion $\epsilon_{66}$, at various temperatures. In a wide range of temperatures, a robust linear behavior is observed and $\chi_s$ can be easily extracted numerically. Figure 2.2(b) is similar to the experimental results in Fig. 2.3(A) [67]. The equilibrium result with both spins and lattice optimized (unrestricted MC) is also shown (red squares) in Fig. 2.2(b).

Our main result is presented in Fig. 2.4, where the numerically calculated $\chi_s$ vs. $T$ is displayed, at the realistic couplings used in previous investigations [79]. In remarkable agreement with experiments, $\chi_s$ grows when cooling down and it develops a sharp peak at $T_S$ (compare with the experimental results of Fig. 2.3(B) from Ref. [67]). These results were obtained via two different procedures (standard ED and the TCA+TBC), and for two lattice sizes, indicating that systematic errors (such as size effects) are small.
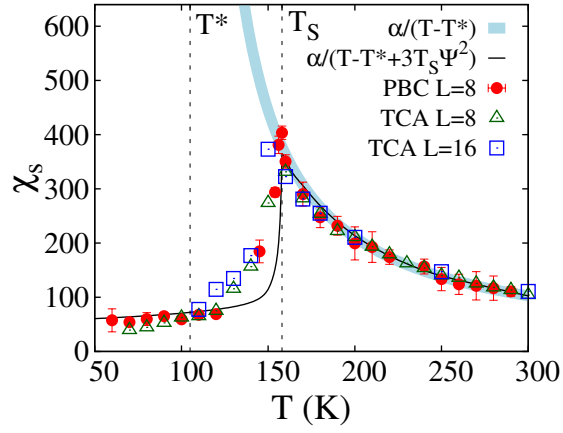
**Figure 2.4:** Nematic susceptibility $\chi_s$ of the spin-fermion model vs. temperature $T$ (circles, triangles, and squares) obtained from Fig. 2.2(b), at the realistic couplings $\tilde{g}_{66}=0.16$ and $\tilde{\lambda}_{66}=0.12$ ($\alpha=\tilde{g}_{66}/a_0$). Two MC techniques were employed: "PBC L=8" is the standard MC method with ED in the fermions at every step, using 8×8 clusters with PBC. "TCA L=8" and "TCA L=16" correspond to the TCA+TBC method on L×L clusters. Size effects are small. Also shown are two GL fits: the light blue (thick) line displays the Curie-Weiss equation $\chi_s \approx \frac{\tilde{g}_{66}}{a_0(T-T^*)}$, indicating a divergence at a lower temperature $T^*$, characteristic of the electronic sector alone. At $T \leq T_S$, the lattice follows the electronic sector. The black (thin) line is Eq.(B.29) with the $3T_S\Psi^2$ correction (see text) [91].

## 2.4 Nematic Susceptibility

### 2.4.1 Analysis of $\chi_s$ results

Supplementing the computational results, here Ginzburg-Landau (GL) calculations were also performed, similarly as in Ref. [67] for experiments. Note that the previous GL analysis considered only a generic nematic order parameter while our study separates the spin and orbital contributions. The rather complex numerical results presented previously can be rationalized intuitively by this procedure. The results for $\chi_s$ (Fig. 2.4) are well fitted quantitatively for $T > T_S$, and qualitatively for $T < T_S$, by the expression:

$$\chi_s = \frac{\tilde{g}_{66}}{a_0[(T - T^*) + 3T_S\Psi^2]}, \tag{2.2}$$

where $T_S$=158 K, $T^*$=105 K, and $a_0\sim0.093$. The GL analysis presented in Appendix B shows that the fitting parameter $a_0$ arises from the GL quadratic term $a\Psi^2/2$ in a second order transition where $a = a_0(T - T^*)$. $\Psi$ is the equilibrium value of the spin nematic order parameter from the unrestricted MC simulations [red, Fig. 2.2(a)] and it is temperature dependent. For $T \geq T_S$, $\Psi$ vanishes and $\chi_s$ exhibits Curie-Weiss behavior, in excellent agreement with the experimental $\chi^{exp}$ [67] and can be seen in Fig. 2.3(B).

Let us discuss the meaning of the parameter $T^*$:

(1) From Fig. 2.2(b), the unrestricted numerical results at the critical temperature $T_S$ indicate a linear relation between $\Psi$ and $\epsilon_{66}$, while individually both behave as order parameters, i.e. they change fast near $T_S$. The lattice distortion is temperature dependent, i.e. $\epsilon_{66} = \epsilon_{66}(T)$, because the lattice is equilibrated together with the spins. However, this nearly temperature independent ratio $\Psi/\epsilon_{66}=K$ ($\sim360$) depends on couplings: comparing results at several values of the coupling $\tilde{g}_{66}$, it is empirically concluded that $K = \frac{\hat{c}}{\tilde{g}_{66}}$ (where $\hat{c}$ is a constant).

Note also that $\chi_s$ depends on the partial derivative $\partial\Psi/\partial\epsilon_{66}|_{\epsilon_0}$, since $\chi_s$ is obtained at a constant temperature varying $\epsilon_{66}$ via strain to match the procedure followed in experiments [67], in the vicinity of the equilibrium point $\epsilon_0$ [namely, $\chi_s$ arises from the green/blue curves of Fig. 2.2(b), not from the red equilibrium curve]. While these slopes

(restricted vs. unrestricted MC) are in general different, both become very similar at temperatures close to $T_S$ where, as shown analytically in Appendix C, these derivatives are indeed almost the same. Thus, at $T_S$: $\frac{d\Psi}{d\epsilon_{66}} = \frac{\hat{c}}{\tilde{g}_{66}} \approx \frac{\partial\Psi}{\partial\epsilon_{66}}|_{\epsilon_0} = \chi_s$. This relation can be independently deduced from the GL analysis, Eq. (B.7), with $\hat{c}=c_0$, and $c_0$ arising from $c_0\epsilon_{66}^2/2$ in the free energy, providing physical meaning to parameters in the computational fits.

(2) Since the numerical susceptibility $\chi_s$ can be fit well by Eq.(B.29) including the special case of $T_S$ where $\Psi = 0$, then, as shown in Appendix B, $T_S = T^* + \frac{\tilde{g}_{66}^2}{a_0\hat{c}}$ [10, 67]. Comparing with Eq (B.10), $\hat{c}$ is again identified with the uncoupled shear elastic modulus $c_0$. In addition, from previous investigations [61] it is known that at $\tilde{g}_{66}=\tilde{\lambda}_{66}=0$ there is no nematic regime and $T_S=T_N$, the Néel temperature. Then, $T_N = T^* + \frac{\tilde{g}_{66}^2}{a_0c_0}$, that at $\tilde{g}_{66} = 0$ leads to the important conclusion that *the scale $T^*$ is simply equal to the Néel temperature of the purely electronic spin-fermion model*. In previous work [61] it was reported that $T_N$ at $\tilde{g}_{66}=\tilde{\lambda}_{66}=0$ is ~100-110 K, in remarkable agreement with the fitting value of $T^*$ obtained *independently*. Thus, in the Curie-Weiss formula $T^*$ is solely determined by the magnetic properties of the purely electronic system.

An important comment is here in order. In principle, by symmetry considerations it is to be expected that all operators with the same $B_{1g}$ symmetry, as $\Psi$, $\Phi$, and $\epsilon_{66}$ have, will simultaneously develop a nonzero expectation value in the ground state if this state breaks spontaneously the $B_{1g}$ symmetry as in the case of the $(\pi, 0)$ antiferromagnetic state. However, the magnitude of these expectation values can be used as an indicator of which one dominates. For instance, although the lattice ($\epsilon_{66}$) does develop a distortion in experiments, its value is widely considered to be too "small" [21] to assume that the lattice is the driver. Consider now the spin and orbital: for results corresponding to our model see Fig. 2.5. That figure contains the expectation values of $\Psi$ (spin) and $\Phi$ (orbital) vs. temperature. The important point is that in the temperature range of that figure the expectation value of $\Psi$ is already a large fraction of the small temperature result, but in the same temperature range $\Phi$ had to be multiplied by 10 to magnify its value to become more visible. Thus, based on these relative values considerations we arrive to the conclusion that in the spin fermion model the spin dominates more than the orbital.
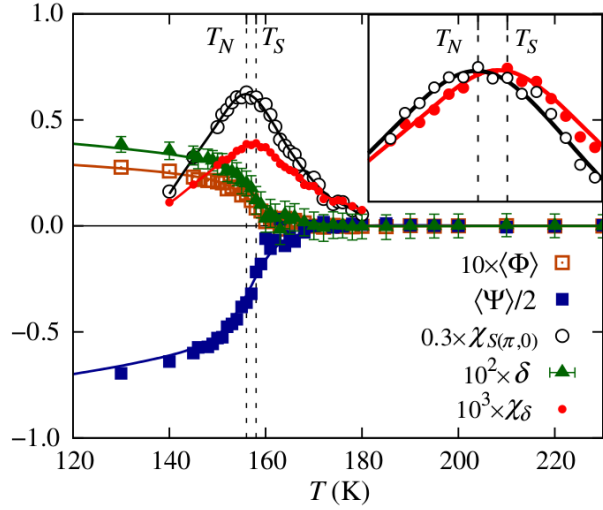
**Figure 2.5:** Spin magnetic susceptibility (open circles), lattice distortion susceptibility (filled circles), spin-nematic order parameter (filled squares), orbital order (open squares), and lattice distortion (triangles) vs T at couplings $\tilde{g_{66}} = 0.16$ and $\tilde{\lambda}_{66} = 0.12$ . $T_N$ and $T_S$ are indicated by the dashed lines. This is a reproduction from Ref. [79].

## 2.4.2   Analysis of $\chi_o$ results

The orbital-based nematic susceptibility, $\chi_o = \frac{\partial \Phi}{\partial \epsilon_{66}}|_{\epsilon_0}$, was also numerically calculated varying the temperature. For small $\tilde{\lambda}_{66}$, such as $\tilde{\lambda}_{66} = 0.12$, the result is approximately temperature independent and well fit by Eq. (B.27) in Appendix B, with $e_0 = 0.016$ and $f = 0.33$. In other words, the analog of Fig. 2.2(b) but for the orbital-nematic order parameter presents blue/green/red curves all with very similar slopes. Then, in $\chi_o$ there is no Curie-Weiss behavior for $T \geq T_S$. However, Raman scattering studies of charge nematic fluctuations in $BaFe_2As_2$ and $Sr(Fe_{1-x}Co_x)_2As_2$ have reported Curie-Weiss behavior in the orbital-nematic susceptibility that was well-fitted by the expression $a + \frac{b}{T-T_0}$ where $a$ represents the temperature independent flat continuum and the Curie-Weiss term describes the diverging behavior of the quasi-elastic peak observed in the Raman spectrum [92] (See Fig. 2.6).

To reproduce the results found in Fig. 2.6 with the spin-fermion model, we considered a small direct coupling $\tilde{\alpha}$ between the magnetic and orbital degrees of freedom, and introduce a new term in the model

$$H_{SO} = -\tilde{\alpha} \sum_{\mathbf{i}} \Psi_{\mathbf{i}} \Phi_{\mathbf{i}}. \qquad (2.3)$$

27

In Fig. 2.7(a) the spin-nematic susceptibility is displayed after repeating the simulation in the presence of this new coupling, and it can be seen that its qualitative form is not affected by the inclusion of a small $\tilde{\alpha} = 0.0011$. However, the orbital susceptibility shown in panel (b) of the same figure now displays Curie-Weiss behavior induced by the new coupling between the orbital and magnetic degrees of freedom. The numerical data are well fitted by the expression

$$\chi_o = \frac{\tilde{\lambda}_{66}}{e_0} + \frac{\tilde{\alpha}(\tilde{g}_{66}e_0 + \tilde{\lambda}_{66}\tilde{\alpha})}{a_0 e_0^2[T - (T^* + \frac{\tilde{\alpha}^2}{a_0 e_0})]}, \tag{2.4}$$

that has the form $a + \frac{b}{T - T_0}$ used in Ref. [92] to fit the experimental data. Notice that Eq. (2.4) has been obtained with the GL approach described in Appendix B.
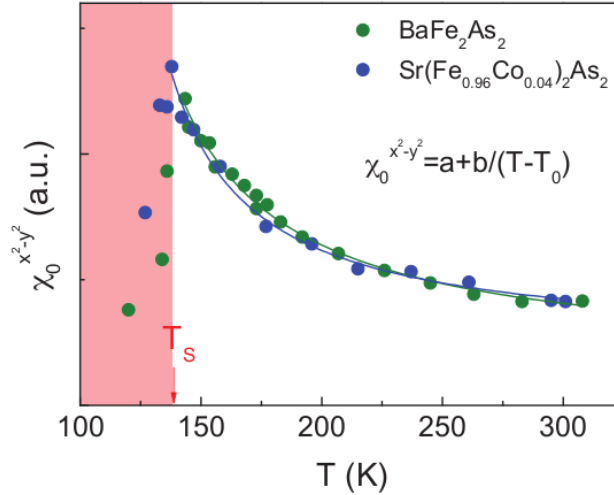


**Figure 2.6:** This figure shows the temperature dependence of the orbital nematic susceptibility for two iron pnictide compounds. The lines are for the Curie-Weiss fit in the tetragonal phase. These susceptibilities were calculated using Raman scattering experiments to measure the orbital anisotropy for a wide range of temperatures. This figure is reproduced from Ref. [92].

The difference between $T^*$ and $T_0$ is only about 10 K for the parameters used here. In other words, if a direct coupling between the magnetic and orbital degrees of freedom is present, the Curie-Weiss divergence still occurs at the Néel temperature for the purely electronic system now given by $T_0$. These results demonstrate how experimental data
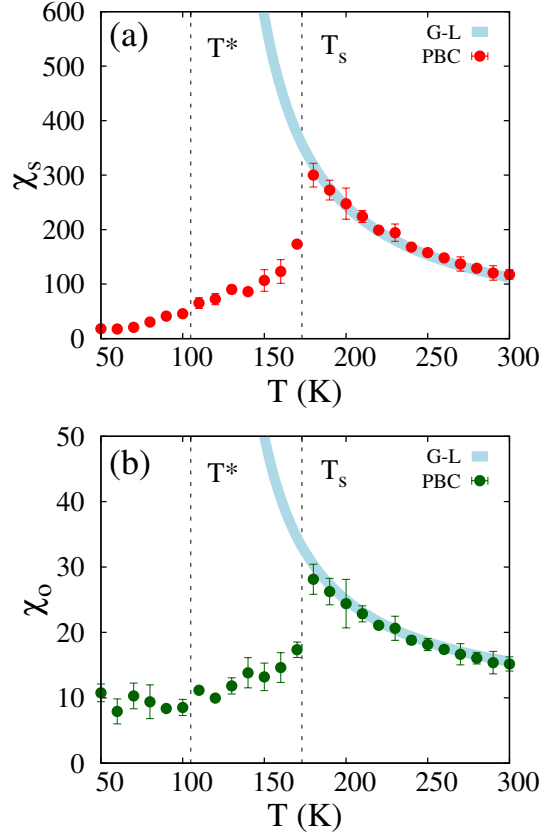
**Figure 2.7:** (a) The spin and (b) orbital nematic susceptibility obtained from Monte Carlo simulations for $\tilde{\alpha} = 0.0011$, $\tilde{g_{66}} = 0.16$, and $\tilde{\lambda_{66}} = 0.12$. The continuous curves in light blue are the fittings obtained from the numerically guided Ginzburg-Landau approach.

obtained with different techniques can all be well reproduced by the spin-fermion model studied here.

## 2.5   $T_S$ vs. $\tilde{\lambda}_{66}$

The study in Figs. 2.2(a,b) was repeated for other values of the coupling $\tilde{\lambda}_{66}$. It was observed that $\hat{c}$ varies with $\tilde{\lambda}_{66}$, compatible with the GL analysis where $c(\tilde{\lambda}_{66}) = c_0(1 - \frac{\tilde{\lambda}_{66}^2}{e_0 c_0})$, Eq. (B.24). At small $\tilde{\lambda}_{66}$, the total (unrestricted MC) and partial (restricted MC) derivatives of $\Psi$ with respect to $\epsilon_{66}$ are still approximately equal at $T \approx T_S$ as shown in Appendix C. Then, $\chi_s \approx c(\tilde{\lambda}_{66})/\tilde{g}_{66} = \frac{\tilde{g}_{66}}{a_0(T_S - T^*)}$, leading to the novel result

$$T_S = T^* + \frac{\tilde{g}_{66}^2}{a_0 c_0 (1 - \frac{\tilde{\lambda}_{66}^2}{c_0 e_0})}. \tag{2.5}$$

Numerically, it was found that $a_0 \sim 0.093$, $c_0 \sim 60$ $e_0 = 0.016$, and $T^* = 105$ K, for $\tilde{g}_{66} = 0.16$ (note that the values of the various GL parameters are the same in all the fits reported here, as expected). In practice, it was observed that Eq.(2.5) fits remarkably well the numerical values for $T_S$ in the range of $\tilde{\lambda}_{66}$ studied showing that the GL approach provides an excellent rationalization of the numerical results. This is shown explicitly in Fig. 2.8(a).

## 2.6   Spin structure factors and pseudogaps

In Fig. 2.8(b), the spin structure factors $S(\mathbf{k})$ calculated with MC at both $(\pi, 0)$ and $(0, \pi)$ are shown. The results illustrate the development of short-range magnetic order upon cooling with two coexisting wavevectors. Within the error bars, given roughly by the oscillations in the plot, these results indicate that the two wavevectors develop with equal weight upon cooling approximately starting at $T_{PG}$ where the pseudogap develops (see below) [93].

In the spin-fermion model, dynamical observables can be easily calculated. In particular, the density of states $N(\omega)$ is shown in Fig. 2.8(c). This figure indicates the presence of a Fermi-level pseudogap (PG) in a wide temperature range, in agreement with photoemission and infrared experiments [94]. A zero temperature pseudogap is to be expected: Hartree-Fock
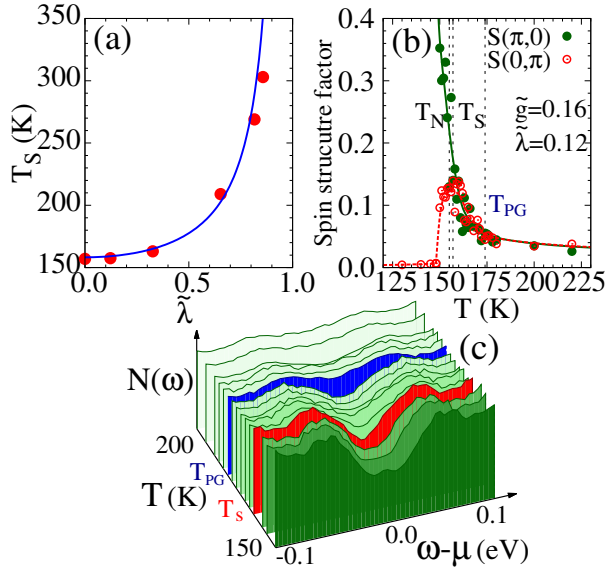
**Figure 2.8:** (a) The MC structural transition temperature $T_S$ vs. the orbital-lattice coupling $\tilde{\lambda}_{66}$, at fixed $\tilde{g}_{66} = 0.16$. The continuous line is the fit in Eq.(2.5), from the GL equations. (b) Spin structure factor $S(\mathbf{k})$ vs. temperature $T$ for the two magnetic wavevectors of relevance. Results were obtained via MC simulations on PBC 8×8 clusters. $T_{PG}$ is the pseudogap temperature [Fig. 2.8(c)]. (c) Density of states $N(\omega)$ (symmetrized) from unrestricted MC simulations on 8×8 clusters ($\tilde{g}_{66}$=0.16; $\tilde{\lambda}_{66}$=0.12), at various temperatures. Results at $T_S$=158 K are in red. $T_{PG}$~174 K (blue) is the crossover temperature where the pseudogap opens at the Fermi level (i.e. at $\omega$-$\mu$=0.0) upon cooling.

studies of the multiorbital Hubbard model [95] already detected such a feature. However, our finite temperature studies reveal that upon cooling this pseudogap develops at a $T_{PG}$ clearly above $T_S$. From the analysis of our results, the pseudogap is present when short-range spin correlations are present [Fig. 2.8(b)]: the "nematic fluctuations" regime is basically the range of temperatures where $(\pi, 0)/(0, \pi)$ magnetic fluctuations exist. The coupling to the lattice creates concomitant local orthorhombic distortions: it is important to remark that the region between $T_S$ and $T_{PG}$ is tetragonal only on *average* [96]. All these results are in good agreement with recent scanning tunneling spectroscopy studies of NaFeAs [97].

## 2.7 Conclusions

Our combined numerical and analytical study of the spin fermion model leads to results in agreement with the experimentally measured nematic susceptibility of Ba(Fe$_{1-x}$Co$_x$)$_2$As$_2$ [67]. For spins coupled to the lattice our spin-nematic susceptibility has a Curie-Weiss behavior for $T > T_S$ governed by a $T^*$ which we here identify as the critical $T_N$ of the purely electronic sector, which is preexisting to the introduction of the lattice. For realistic nonzero electron-lattice couplings, the lattice induces a nematic/structural transition at a higher temperature $T_S$. The addition of an orbital-lattice coupling $\tilde{\lambda}_{66}$ further increases $T_S$, with a Curie-Weiss behavior that continues being regulated by $T^*$.

Our main prediction is that whenever fluctuating nematic order is observed, inelastic neutron scattering for the same sample should also reveal the existence of short-range magnetic order: nematic fluctuations, pseudogap, and short-range antiferromagnetic order should all develop *simultaneously* in these materials. Although the experiments in Ref. [67] were conducted over a range of dopings, these numerical results were limited to the parent compounds. Also, as stated in Sec. 2.1, this nematic susceptibility is dependent on an applied strain which is different from the 1111 compounds and doped 122 materials. For this reason, a model that can numerically study the doped 122 compounds will be the focus of Ch. 3.

# Chapter 3

# Disorder Induced Nemacity

This chapter is a modified version of PHYSICAL REVIEW B 92, 104512 (2015) [98, 99].

## 3.1    Introduction

As previously mentioned in Sec. 1.4, the interaction among the many different DOF in pnictides generates rich phase diagrams when varying temperature and doping [49]. In addition to the superconducting phase, magnetic and nematic phases, accompanied by structural distortions, have been identified [49, 67, 71, 100]. To properly address this difficult problem it is necessary that the spin, orbital, lattice, and charge should all be incorporated in a treatable model where their respective roles in the properties of these materials can be monitored. Due to the complexity of the problem, most of the previous theoretical studies have been performed either in the weak or strong coupling limits. In weak coupling, the interactions among the electrons are considered small and the physical properties are studied in momentum space in terms of itinerant electrons, with emphasis on particular properties of their Fermi Surfaces (FS) such as nesting [33, 34, 36, 73, 75]. On the other hand, the strong coupling approach is based on the experimental observation of localized magnetic moments and on the fact that several properties of the pnictides can be reproduced via Heisenberg models [31, 46, 74]. Both approaches were successful in the study of the magnetic properties of the parent compounds, indicating that in these materials both localized and itinerant magnetic moments are important. However, upon doping there are

challenges explaining experimental data in both approximations. In particular, when doping is achieved by chemical substitution of iron atoms the effects of disorder and dilution must also be incorporated into the theoretical considerations.

The parent compound of the 122 family, $BaFe_2As_2$, can be doped with electrons by replacing Fe by a transition metal (TM) resulting in $Ba(Fe_{1-x}TM_x)_2As_2$ or with holes by replacing Ba by an alkali metal (A) leading to $Ba_{1-x}A_xFe_2As_2$ [101]. It is also possible to dope in an isovalent manner replacing, for example, Fe with Ru to obtain $Ba(Fe_{1-x}Ru_x)_2As_2$ [102]. Nominally, replacing Fe with Ru, Co, Ni, and Cu would introduce 0, 1, 2, and 3 electrons per dopant atom. However, experiments indicate a difference between nominal doping $x$ and the measured doping concentration $x_m$ usually determined using wavelength dispersive x-ray spectroscopy (WDS) [49]. This means that in some cases, electrons may get trapped by the doped impurities but this is still an area of controversy [103, 104, 105]. Chemical substitution introduces an amount of disorder that is difficult to control experimentally. In addition to electrons being trapped, other effects such as magnetic dilution and impurity scattering may also occur [106].

In undoped 122 compounds the structural and the Néel transition temperatures, $T_S$ and $T_N$, are equal to each other. Upon electron doping both are rapidly reduced, with $T_S$ decreasing at an equal or slower rate than $T_N$ [49, 102]. The reduction of these temperatures is explained in weak coupling by a loss of FS nesting induced by the electronic doping and in strong coupling by magnetic dilution as in $t$-$J$ models. However, these views seem to be in contradiction with several experimental results. For example, in $Ba(Fe_{1-x}Ru_x)_2As_2$, which nominally does not introduce electronic doping and associated changes in FS should not be expected, both $T_S$ and $T_N$ decrease with doping and the material eventually becomes superconducting [102]. In addition, doping with Co, Ni, and Cu is expected to introduce 1, 2, and 3 extra electrons per doped atom. However, the experimentally observed reduction on $T_N$ and $T_S$ was found to be primarily a function of the doping concentration $x$ rather than of the density of electrons [49, 107]. Experiments, thus, indicate that when dopants are introduced directly on the Fe-As planes, as it is the case for electron-doped 122 materials, disorder and dilution must play an important role [33, 34, 49, 108, 109, 110, 111, 112, 113]. Due to the experimental uncertainty on the doping concentration and the nature of the disorder,

a theoretical understanding of the phase diagrams under these challenging circumstances is elusive. Density functional theory (DFT) studies indicated that the rigid band model is insufficient to describe the carrier density [103], while first-principles methods found that the interplay between on-site and off-site impurity potentials could induce FS distortions in nominally isovalent doping [106]. Moreover, a calculation considering two-orbiton processes predicts a non-symmetric impurity potential which could be responsible for the observed transport anisotropies [33, 34].

In this Chapter, the effects of electron doping in the 122 pnictides will be studied numerically using a spin-fermion model (SFM) for the pnictides [52, 57, 61] including the lattice DOF [79]. The SFM considers phenomenologically the experimentally motivated evidence that requires a combination of itinerant and localized DOF to properly address the iron-based superconductors [12, 51, 114, 115]. The itinerant sector mainly involves electrons in the $xz$, $yz$, and $xy$ $d$-orbitals [56], while the localized spins represent the spin of the other $d$-orbitals [52, 57], or in a Landau-Ginzburg context it can be considered as the magnetic order parameter.

The focus of this effort will be on the structural and the Néel transitions, and the properties of the resulting nematic phase that will be monitored as a function of the electronic and impurity densities. Earlier studies performed in the undoped parent compounds indicated that the coupling between the lattice orthorhombic distortion $\epsilon_{66}(\mathbf{i})$, associated to the elastic constant $C_{66}$, and the spin-nematic order parameter $\Psi_{\mathbf{i}}$ stabilizes the orthorhombic $(\pi, 0)$ antiferromagnetic (AFM) ground state [79] with $T_S = T_N$ as in the 122 materials [49]. The small separation between $T_S$ and $T_N$ observed in the parent compounds of the 1111 family [30] was found to be regulated by the coupling of the lattice orthorhombic distortion to the orbital order parameter $\Phi_{\mathbf{i}}$ [79].

The effect of disorder in iron superconductors has been studied before using mainly analytical or semi-analytical techniques and primarily in the context of Fermi Surface nesting (for a partial list of references see Refs. [116, 117]). However, ours is the first time that electronic doping supplemented by quenched disorder and dilution effects is computationally studied in a system that includes magnetic, charge, orbital, and lattice DOF. Our numerical approach involves Monte Carlo (MC) calculations on the localized spin

and lattice components, combined with a fermionic diagonalization of the charge/orbital sector. Technically, we also employ twisted boundary conditions (TBC) (See Ref. [89] and Ref. [61]) and the Traveling Cluster Approximation (TCA) is implemented (See Ref. [86] and Ref. [87]) in order to study large clusters of size $64 \times 64$, a record for the spin-fermion model. This numerical approach allows us to incorporate the effects of in-plane chemical doping and to gather results for temperatures above $T_S$, where all DOF develop strong short-range fluctuations [73, 96], a difficult regime for other many-body procedures. Our main conclusion is that disorder and dilution are needed to stabilize the broad nematic phase in 122 materials observed experimentally. That a critical temperature such as $T_N$ decreases faster with doping by including disorder than in the clean limit is natural [118, 119], but our most novel result is the concomitant stabilization of a nematic regime. In other words, $T_N$ and $T_S$ are affected *differently* by disorder/dilution. Isotropic dopant profiles are sufficient to obtain these results. Our analysis illustrates the interdependence of the many degrees of freedom present in real materials and the need to study models with robust many-body techniques to unveil the physics that emerges in these complex systems.

The organization of this Chapter is as follows: the model is described in Sec. 3.2 and the computational methods are presented in Sec. 3.3. Sec. 3.4 is devoted to the main results addressing the phase diagram upon doping. Sec. 3.5 describes the properties of the nematic phase stabilized in our study, including a comparison with neutron scattering and scanning tunneling microscopy experiments. The discussion and summary are the scope of Sec. 3.6.

## 3.2    Model

### 3.2.1    Hamiltonian

The spin-fermion model studied in this chapter is based on the Hamiltonian outlined in Sec. 2.2 and further details can be found in Appendix A. This Hamiltonian consists of the original purely electronic model [52, 57, 61] supplemented by the addition of spin couplings to the lattice degrees of freedom [61, 68]:

$$H_{\mathrm{SF}} = H_{\mathrm{Hopp}} + H_{\mathrm{Hund}} + H_{\mathrm{Heis}} + H_{\mathrm{SL}} + H_{\mathrm{Stiff}}. \tag{3.1}$$

$H_{\text{Hopp}}$ is the three-orbitals ($d_{xz}$, $d_{yz}$, $d_{xy}$) tight-binding Fe-Fe hopping of electrons, with the hopping amplitudes selected to reproduce ARPES experiments [56]. These amplitudes can be found in Eqs.(A.3-A.5) and Table A.1 of Appendix A. The average density of electrons per iron and per orbital is $n=4/3$ in the undoped limit [56] and its value in the doped case is controlled via a chemical potential included in $H_{\text{Hopp}}$ [68]. The Hund interaction is standard: $H_{\text{Hund}}=-J_{\text{H}} \sum_{\mathbf{i},\alpha} \mathbf{S_i} \cdot \mathbf{s}_{\mathbf{i},\alpha}$, with $\mathbf{S_i}$ the localized spin at site $\mathbf{i}$ (with magnitude 1) and $\mathbf{s}_{\mathbf{i},\alpha}$ the itinerant spin corresponding to orbital $\alpha$ at the same site [120]. $H_{\text{Heis}}$ contains the Heisenberg interaction among the localized spins involving both nearest-neighbors (NN) and next-NN (NNN) interactions with respective couplings $J_{\text{NN}}$ and $J_{\text{NNN}}$, and a ratio $J_{\text{NNN}}/J_{\text{NN}} = 2/3$ (any ratio larger than $1/2$ would have been equally effective to favor "striped" spin order). For specific details see Sec. 3.3 below. Having NN and NNN Heisenberg interactions of comparable magnitude arise from having comparable NN and NNN hoppings, caused by the geometry of the material since this is mediated via the As atoms, and NN and NNN hopings cover roughly the same distance.

The coupling between the spin and lattice degrees of freedom is given by $H_{\text{SL}}=$ $-g_{66} \sum_{\mathbf{i}} \Psi_{\mathbf{i}} \epsilon_{66}(\mathbf{i})$ [36, 75], where $g_{66}$ is the spin-lattice coupling [84]. The spin nematic order parameter is defined as

$$\Psi_{\mathbf{i}} = \mathbf{S_i} \cdot \mathbf{S_{i+y}} - \mathbf{S_i} \cdot \mathbf{S_{i+x}}, \tag{3.2}$$

where $\mathbf{x}$ and $\mathbf{y}$ are unit vectors along the $x$ and $y$ axes, respectively. This order parameter becomes 2 in the perfect ($\pi$,0) state. The lattice $\epsilon_{66}(\mathbf{i})$ degree of freedom related to the tetragonal to orthorhombic distortion has a more complex definition in terms of the positions of the As or Se atoms, and its precise definition can be found in Ref. [79]. $H_{\text{Stiff}}$ is the lattice stiffness given by a Lennard-Jones potential that speeds up convergence, as previously discussed [68].

Note that the lattice-orbital coupling term, $H_{\text{OL}}=-\lambda \sum_{\mathbf{i}} \Phi_{\mathbf{i}} \epsilon_{66}(\mathbf{i})$ [68], with the orbital nematic order parameter defined as

$$\Phi_{\mathbf{i}} = n_{\mathbf{i},xz} - n_{\mathbf{i},yz}, \tag{3.3}$$

where $n_{xz}$ and $n_{yz}$ are the number operators for the orbitals indicated, is omitted because previous work indicated that $\lambda$ induces a (small) nematic phase with $T_S > T_N$ directly in the parent compounds [68, 79]. Since the goal of the present effort is to study the 122 family, characterized by $T_S = T_N$ in the undoped case, then this term is not included to reduce the number of parameters.
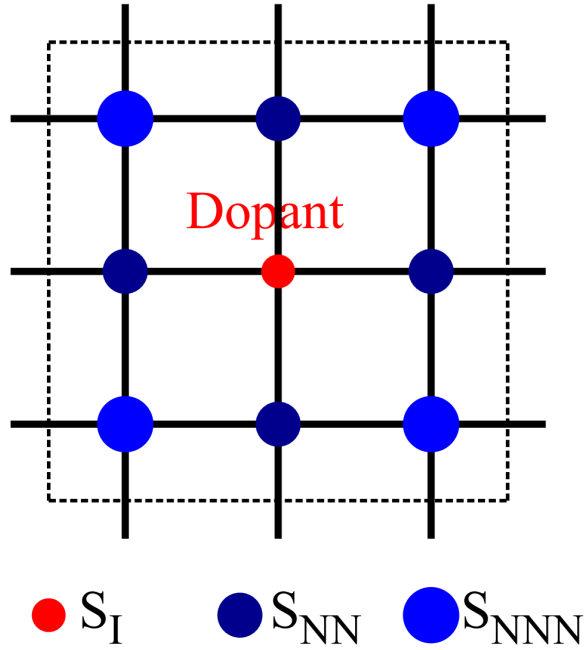


**Figure 3.1:** *Internal structure of dopant sites.* Sketch shows the location of a dopant where the magnitude of the localized spin, $S_I$, is reduced from the original value $S$. In addition, the neighboring localized spins are also assumed to be affected by the presence of the dopant. The four immediate nearest-neighbors have a new localized spin magnitude $S_{NN}$, while the four next nearest-neighbors have a new localized spin magnitude $S_{NNN}$, such that $S_I \leq S_{NN} \leq S_{NNN} \leq S$ ($S$ is the undoped localized spin magnitude, assumed to be 1 in this publication unless otherwise stated).

We also wish to clarify that when varying the global chemical potential, thus modifying the electronic density, we assume that all couplings are unaffected. In particular, since the orbitals that induce the localized spins are assumed to be weakly affected by modifications in the position of the Fermi level, then there is no obvious reason to modify $J_{NN}$ and $J_{NNN}$ with increasing electron doping. This is similar as in studies of manganites via the double-exchange model where with doping the couplings of the $t_{2g}$ sector are assumed to be fixed [82].

### 3.2.2 Quenched Disorder and Dilution

On-site diagonal disorder is introduced through an impurity potential $I_I(\mathbf{i}_d)$ by adding this same value of potential to $N_I$ randomly selected sites $\mathbf{i}_d$ where transition metal atoms replace Fe. The density of impurity atoms $x$ is defined as $x = N_I/N$, where $N$ is the total number of lattice sites. In addition, the value of the localized spin at the impurity site, $S_I$, is reduced since, for example, Co dopants in $BaFe_2As_2$ are non-magnetic [121]. This effectively reduces the local Hund coupling $J_{H,I}$ and the spin-lattice coupling $g_{66}(i)$ at the impurity sites. We also will study the effect of extending the spatial range of the impurity by reducing the values of the localized spins to $S_{NN}$ ($S_{NNN}$) at the NN (NNN) of the impurity sites with the corresponding effective decrease in $J_H$ and $g_{66}$ at those sites (see Fig. 3.1). Thus, off-diagonal isotropic disorder results from the effective reduction of the Heisenberg couplings at the bonds connecting the impurity sites and their neighbors [120]. Note that off-diagonal disorder could also be introduced in the eight hopping amplitudes present in $H_{Hopp}$ [68] but for simplicity we decided not to consider hopping disorder at this time.

## 3.3 Methods

The Hamiltonian in Eq.(3.1) was studied via Monte Carlo methods explained in Ref. [82] and Ch. 7 of Ref. [85] and are applied to *(i)* the localized (assumed classical) spin degrees of freedom $\mathbf{S_i}$ and *(ii)* the atomic displacements that determine the local orthorhombic lattice distortion $\epsilon_{66}(\mathbf{i})$ [68, 79]. For each Monte Carlo configuration of spins and atomic positions the remaining quantum fermionic Hamiltonian is diagonalized. The simulations are performed at various temperatures, dopings, and disorder configurations and local and long-range observables are measured. Note that with the exact diagonalization technique results can be obtained comfortably only on up to $8 \times 8$ lattices, which may be too small to provide meaningful data at the low rates of doping relevant in the pnictides. For this reason we have also used the Traveling Cluster Approximation (See Ref. [86] and Ref. [87]) where a larger lattice ($64 \times 64$ sites in most of this effort) can be studied by performing the MC updates via a traveling cluster centered at consecutive sites $\mathbf{i}$, with a size substantially smaller than the full lattice size of the entire system. Twisted boundary conditions were

also used (See Ref. [89] and Ref. [61]) to obtain (almost) a continuum range of momenta. For simplicity, most couplings are fixed to values used successfully before [61]: $J_{\mathrm{H}}$=0.1 eV, $J_{\mathrm{NN}}$=0.012 eV, and $J_{\mathrm{NNN}}$=0.008 eV. The dimensionless version of the spin-lattice coupling $\tilde{g}_{66}$ is fixed to 0.16 as in Ref. [79]. The focus of the publication is on the values for the parameters associated with disorder and the corresponding physical results, as discussed in the sections below.

An important technical detail is that to improve numerical convergence, and to better mimic real materials that often display an easy-axis direction for spin orientation, we have introduced a small anisotropy in the $x$ component of the super-exchange interaction so that the actual Heisenberg interaction is:

$$
\begin{aligned}
H_{\mathrm{Heis}} = J_{\mathrm{NN}} \sum_{\langle \mathbf{ij} \rangle} (\mathbf{S_i} \cdot \mathbf{S_j} + \delta S_\mathbf{i}^x S_\mathbf{j}^x) \\
+ J_{\mathrm{NNN}} \sum_{\langle\langle \mathbf{im} \rangle\rangle} (\mathbf{S_i} \cdot \mathbf{S_m} + \delta S_\mathbf{i}^x S_\mathbf{m}^x),
\end{aligned}
\tag{3.4}
$$

with $\delta = 0.1$. This anisotropy slightly raises $T_N$, but the magnetic susceptibility $\chi_S$ becomes much sharper at the transition temperatures, facilitating an accurate determination of $T_N$. It is important to clarify that the easy-axis anisotropy affects the direction in which the spins order, but by no means breaks explicitly the $C_4$ lattice rotational invariance that is related to nematicity via its spontaneous breaking. In other words, we have checked explicitly that perfect $(\pi,0)$ and $(0,\pi)$ localized spins configurations have identical energy if their spins are oriented along the same axis, either the easy-axis which minimizes the global energy or any other. Of course if, say, $(\pi,0)$ is oriented along the $x$ axis and $(0,\pi)$ along the $z$ axis then there is an energy difference, but as long as the spin orientations are the same then the expected degeneracies are present. In fact, previously theoretical studies of nematicity have been performed even in the extreme Ising limit [122].

The Monte Carlo simulations with the TCA procedure were mainly performed using $64 \times 64$ square lattices [123]. Typically 5,000 MC steps were devoted to thermalization and 10,000 to 25,000 steps for measurements at each temperature, doping, and disorder configuration. The results presented below arise from averages over five different disorder

configurations. The expectation values of observables remain stable upon the addition of extra configurations due to self-averaging. The magnetic transition was determined by the behavior of the magnetic susceptibility defined as

$$\chi_{S(\pi,0)} = N\beta\langle S(\pi,0) - \langle S(\pi,0)\rangle\rangle^2, \tag{3.5}$$

where $\beta = 1/k_B T$, $N$ is the number of lattice sites, and $S(\pi,0)$ is the magnetic structure factor at wavevector $(\pi,0)$ obtained via the Fourier transform of the real-space spin-spin correlations measured in the MC simulations. The structural transition is determined by the behavior of the lattice susceptibility defined by

$$\chi_\delta = N\beta\langle\delta - \langle\delta\rangle\rangle^2, \tag{3.6}$$

where $\delta = \frac{(a_x - a_y)}{(a_x + a_y)}$, and $a_i$ is the lattice constant along the $i = x$ or $y$ directions. These lattice constants are determined from the orthorhombic displacements $\epsilon_{66}(\mathbf{i})$ [68].

## 3.4  Results

Our first task is to understand the effect of doping and disorder on the magnetic and structural transitions. For this purpose, we studied the evolution of $T_N$ and $T_S$ vs. doping concentration under different disorder setups.

### 3.4.1  Clean limit

Consider first the "clean limit". The red squares in Fig. 3.2 show the evolution of $T_N$ and $T_S$ when the electronic doping does *not* introduce disorder. In this case $T_N$ is hardly affected and it continues to be equal to $T_S$ for all dopings investigated here. This result indicates that the reduction of $T_N$ and $T_S$, and the stabilization of a nematic phase in between the two transitions observed experimentally upon electron doping [49], does not emerge just from the reduction of Fermi Surface nesting induced by the electronic doping. This conclusion is not surprising if we recall that the undoped $N$-site lattice has $4N$ electrons which means that

for $x = 10\%$ the number of added electrons is $N_e = 0.1N$ and, thus, the percentual change in the electronic density is just $100 \times (0.1N/4N) = 2.5\%$. Such a small percentual variation in the electronic density should not produce substantial modifications in the Fermi Surface, explaining why the changes in nesting are small and, thus, why the critical temperatures are not significantly affected. In fact, we have calculated explicitly the Fermi Surface and confirmed that it hardly changes in the range of doping studied and in the clean limit. Then, disorder and dilution are needed to understand the experiments within the context of the spin fermion model.
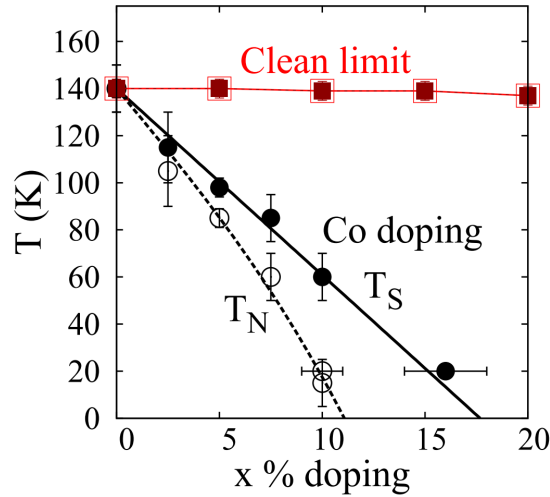


**Figure 3.2:** *Clean limit and effect of Co doping.* The clean limit results (open and solid red points) indicate that $T_S = T_N$ and both are approximately constant in the range studied. For Co doping, the Néel temperature $T_N$ (open circles and black dashed line) and the structural transition temperature $T_S$ (filled circles and black solid line) vs. the percentage of impurities $x$ are shown. The on-site disorder is $I_{\mathrm{I}} = -0.1$ and the off-diagonal disorder is determined by $S_{\mathrm{I}} = 0$, $S_{\mathrm{NN}} = S/4$, and $S_{\mathrm{NNN}} = S/2$. For both sets of curves, i.e. with and without quenched disorder, the density of doped electrons equals $x$ to simulate Co doping. The cluster used has a size $64 \times 64$.

## 3.4.2 Co doping

To study the effect of quenched disorder, let us first focus on Co doping, which nominally introduces one extra electron per dopant. In Fig. 3.2, the Néel and structural transition temperatures are presented for the case where one extra electron is contributed by each

replaced iron atom, which means that $x = n$, where $n$ is the density of added electrons and $x$ is the density of replaced iron atoms. We considered several possible values for the on-site impurity potential and spin values near the impurity (see details discussed below) and we found that the experimental data of Ref. [49] were best reproduced by setting the on-site impurity potential as $I_I = -0.1$ (in eV units) [124] and by using $S_I = 0$ at the impurities since there is evidence that Co doped in $BaFe_2As_2$ is non-magnetic [121]. This effectively sets to zero the Hund coupling $J_{H,I}$ and the spin-lattice coupling $g_{66}(I)$ at the impurity sites. In addition, we also reduced the localized spins to $S/4$ ($S/2$) at the NN (NNN) of the impurity sites with the corresponding effective decreased in $J_H$ and $g_{66}$ at those sites. The overall chemical potential $\mu$ was adjusted so that the density of added impurities equals the density of added electrons, which corresponds to an ideal Co doping [49].
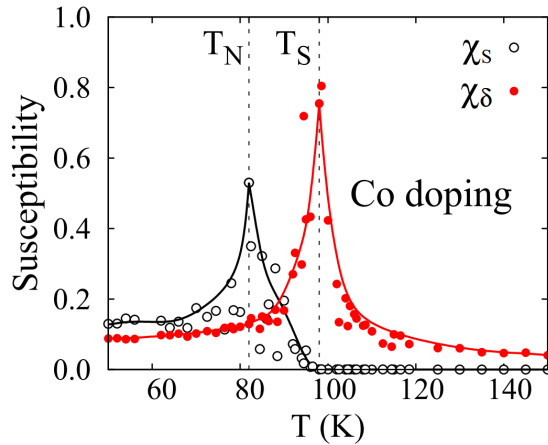


**Figure 3.3:** The magnetic susceptibility (open black symbols) and the lattice susceptibility (filled red symbols) vs. temperature. The sharp peaks indicate the Néel temperature $T_N$ and the structural transition temperature $T_S$ for the case of 5% Co-doping. The on-site disorder is $I_I = -0.1$ and the off-diagonal disorder is defined by $S_I = 0$, $S_{NN} = S/4$, and $S_{NNN} = S/2$. The cluster used is $64 \times 64$.

The black filled (open) circles in Fig. 3.2 show the evolution with impurity doping of the structural (Néel) transition temperatures in the presence of the disorder caused by replacing Fe by Co at random sites. The magnetic dilution induced by doping causes a rapid reduction in $T_S$ and $T_N$, similarly as observed in experiments [49], and remarkably also opens a robust nematic phase for $T_N < T < T_S$ since disorder affects *differently* both transition

temperatures. In fact, the separation between $T_N$ and $T_S$ is very clear in the magnetic and lattice susceptibilities that are displayed for 5% doping, as example, in Fig. 3.3. The magnetic properties of the different phases are also clear by monitoring the behavior of the real-space spin-spin correlation functions presented in Fig. 3.4. In panel (a) for $T = 120$ K $(T > T_S)$ the spin correlations effectively vanish at distances larger than two lattice constants and there is no difference between the results along the $x$ and $y$ axes directions, indicating a paramagnetic ground state. However, at $T = 95$ K $(T_N < T < T_S)$, panel (b), the correlations now display short-range AFM (FM) order along the $x$ ($y$) directions demonstrating the breakdown of the rotational invariance that characterizes the nematic phase, but without developing long-range order as expected. Lowering the temperature to $T = 80$ K $(T < T_N)$, panel (c), now the correlations have developed long range $(\pi, 0)$ order, as expected in the antiferromagnetic ground state. To our knowledge, the results in figures such as Fig. 3.2 provide the largest separation between $T_S$ and $T_N$ ever reported in numerical simulations of realistic models for iron-based superconductors.
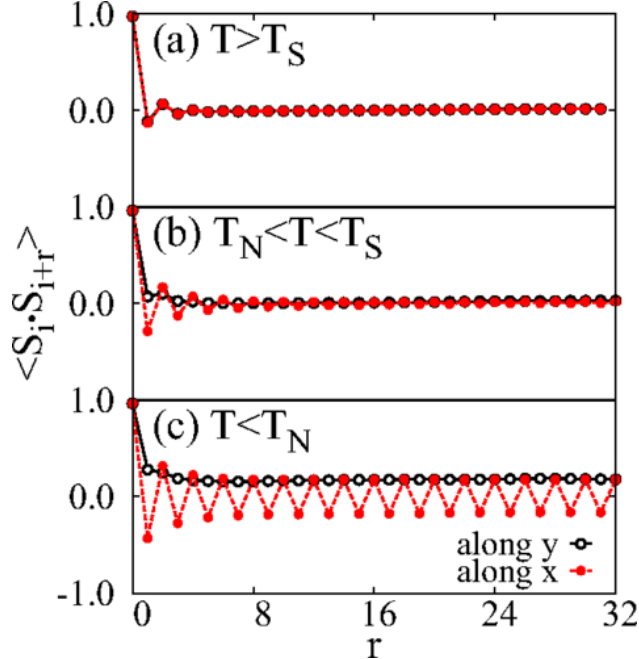
**Figure 3.4:** Real-space spin-spin correlation functions vs. distance on a $64 \times 64$ lattice; (a) corresponds to $T = 120$ K $(T > T_S)$ in the paramagnetic regime, (b) to $T = 95$ K $(T_N < T < T_S)$ in the nematic state, and (c) to $T = 80$ K $(T < T_N)$ in the long-range ordered magnetic state. The AFM correlations along $x$ are indicated with solid circles while the FM correlations along $y$ are denoted with open circles. The results are for 5% Co-doping with off-diagonal disorder set by $S_I = 0$, $S_{NN} = S/4$, and $S_{NNN} = S/2$.

### 3.4.3 Cu doping

Let us consider now the effect of doping with Cu which, nominally, introduces three electrons per doped impurity [49]. For this purpose we increased the chemical potential at a faster rate so that the added density of electrons is $n = 3x$, instead of $n = x$ as for Co doping. The results are shown in Fig. 3.5. When the critical temperatures for both Cu and Co doping are plotted as a function of the density of impurities $x$, in Fig. 3.5(a) it can be seen that the results are approximately *independent* of the kind of dopant. This indicates that the critical temperatures are primarily controlled by the amount of quenched disorder (namely, by the number of impurity sites) rather than by the actual overall electronic density, at least in the range studied. This conclusion is in excellent agreement with the experimental phase diagrams [49] shown, for example, in Fig. 3.6(a), for the case of several transition metal dopants. Thus, working at a fixed electronic density $n$, the values of $T_N$ and $T_S$ are smaller for

the case of Co doping than for the case of Cu-doping, as shown in Fig. 3.5(b), because more Co than Cu impurities have to be added to achieve the same electronic density, underlying the fact that Co doping introduces more disorder than Cu doping at fixed $n$. These results are also in good agreement with the experimental phase diagram in Fig. 3.6(b).
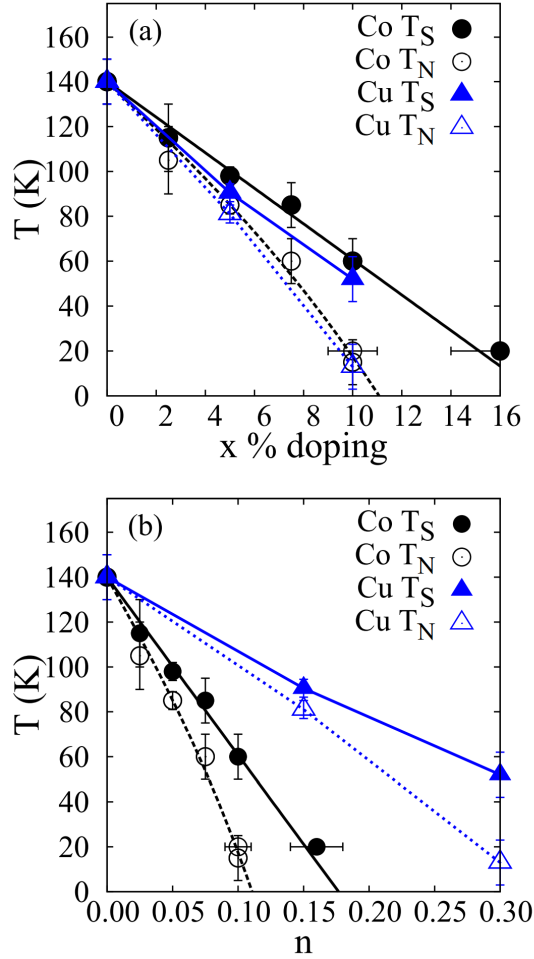


**Figure 3.5:** *Contrast of effects of Cu and Co doping.* The Néel temperatures $T_N$ (dashed lines) and the structural transition temperatures $T_S$ (solid lines) for Co doping (black open and solid circles) and for Cu doping (blue open and solid triangles) are shown. Results are presented first (a) vs. the impurity density $x$ and second (b) vs. the added electronic density $n$. The off-diagonal disorder is set at $S_I = 0$, $S_{NN} = S/4$, and $S_{NNN} = S/2$. The cluster size is $64 \times 64$.
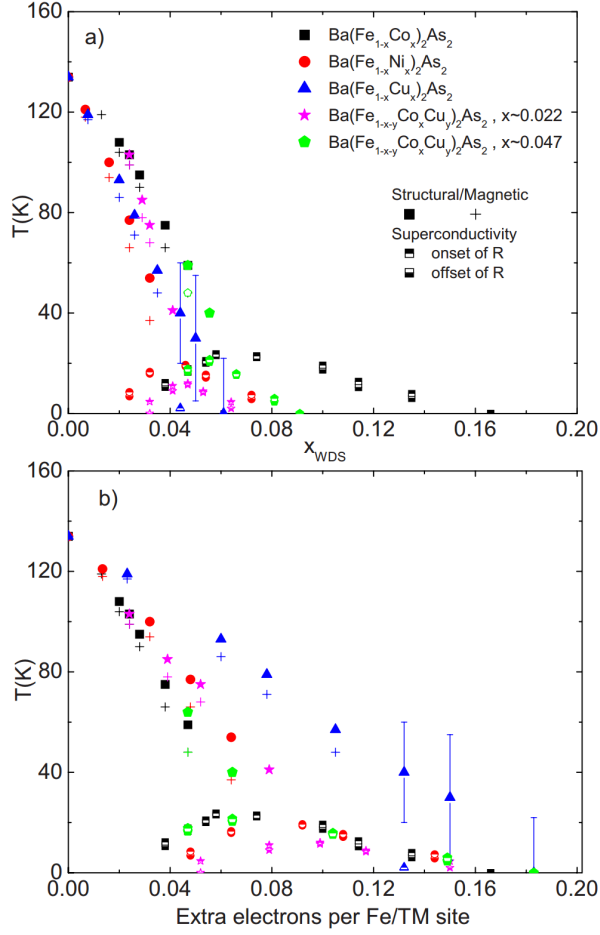
**Figure 3.6:** (a) Temperature (K) vs number of dopants (x) phase diagrams for $Ba(Fe_{1-x}TM_x)_2As_2$ where TM=Co, Ni, Cu, Co/Cu. (b) The same as figure (a) however instead of the x-axis being the added dopants (x), the x-axis is the number of added electrons per Fe/TM. This figure is reproduced from Ref. [49].

### 3.4.4 Dependence on impurity characteristics

Let us consider the dependence of the Néel and the structural transitions temperatures on the local details of the magnetic dilution caused by the disorder. In Fig. 3.7 results for $T_N$ and $T_S$ are shown as a function of impurity doping with the chemical potential set to introduce one electron per dopant. The clean limit data (red squares, case I) is displayed again for the sake of comparison. The blue triangles (case II) are results for $I_I = -0.1$eV and $S_I = S/2$, leaving $S_{NN}$ and $S_{NNN}$ untouched (i.e. equal to $S$). This ultra local magnetic dilution induces effective NN and NNN reductions in the Heisenberg couplings accelerating

the rate of decrease of the critical temperatures. However, the nematic phase is still not stabilized and, thus, it does not reproduce the experimental behavior for the Co-doped parent compound. Reducing $S_I$ to zero, as indicated by the green diamonds in the figure (case III) and keeping $S_{NN}$ and $S_{NNN}$ untouched, slightly increases the rate of reduction of the critical temperatures with doping and stabilizes the nematic phase only after a finite amount of doping $x \sim 10\%$ has been added but in a very narrow range of temperature. The conclusion of cases I, II, and III is that a very local description of the dopant is insufficient to reproduce experiments.
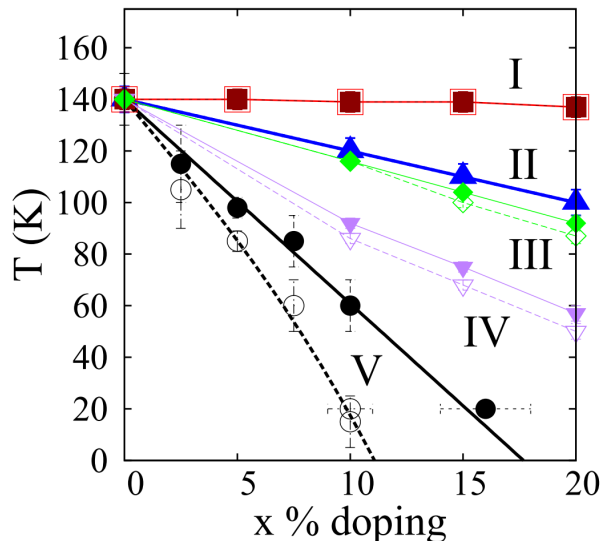


**Figure 3.7:** *Dependence of results with impurity characteristics.* The Néel transition temperature $T_N$ (dashed lines) and the structural transition temperature $T_S$ (solid lines) vs. the percentage of impurities $x$ for different settings of the off-diagonal disorder. Case I corresponds to the clean limit with no impurity sites (red squares). Case II has $S_I=S/2$ and $S_{NN}=S_{NNN}=S$ untouched (blue triangles). This case may be sufficient for Ru doping, which is magnetic. Case III has $S_I=0$ and $S_{NN}=S_{NNN}=S$ untouched (green diamonds). Case IV has $S_I=S/2$, $S_{NN}=0.7S$, and $S_{NNN}=0.9S$ (purple upside-down triangles). Finally, Case V has $S_I=0$, $S_{NN}=S/4$, and $S_{NNN}=S/2$ (black circles). Case V appears to be the best to describe experiments for non-magnetic doping. The density of doped electrons equals $x$ as in Co doping. In all cases the on-site disorder potential is kept fixed at $I_I = -0.1$. The lattice size is $64 \times 64$.

We have found that in order to generate a robust nematic phase upon doping, extended effects of magnetic dilution *must* be considered. The upside-down purple triangles (case IV) in Fig. 3.7 show results for $S_I = S/2$, $S_{NN} = 0.7S$, and $S_{NNN} = 0.9S$. The nematic regime is

still too narrow. But the results for $S_I = 0$ with $S_{NN} = S/4$ and $S_{NNN} = S/2$ (black circles, case V), already shown in Fig. 3.2, indicate that increasing the strength of the extended off-diagonal disorder does induce a faster reduction of the critical temperatures and stabilizes a larger nematic region. Our computer simulations suggest that the range and strength of disorder, specifically the extended magnetic dilution, is crucial for the stabilization of the nematic phase when $T_N = T_S$ in the parent compound.

We have observed that the effect of the on-site impurity potential $I_I$ is weak. In principle, we could have kept the overall chemical potential $\mu$ fixed and control the added electronic density $n$ by merely adjusting the values of the impurity potential. However, this does not induce noticeable changes in the critical temperatures, due to the small overall modifications in the electronic density discussed before. This is not the manner in which doping seems to act in the real electron-doped pnictides. Thus, we believe that working with a fixed value of the impurity potential and adjusting the electronic density with the overall chemical potential allows to study the effects of isotropic quenched disorder and varying electronic density in a more controlled and independent way.
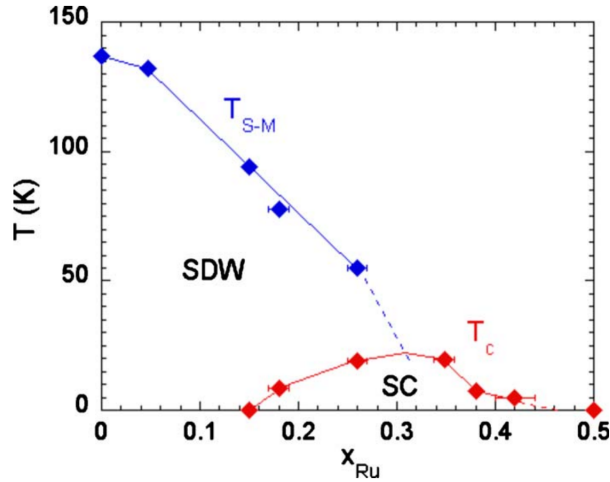


**Figure 3.8:** Phase diagram of $Ba(Fe_{1x}Ru_x)_2As_2$ showing the structural-magnetic transition $T_{S-M}$ (blue) and critical temperatures $T_c$ (red) versus Ru content $x_{Ru}$. Values of $T_c$ are taken at the midpoint of superconducting transitions. This figure is a reproduction from Ref [102].

Considering the negligible effect on the critical temperatures caused by pure electronic doping (clean limit) and, by extension, the on-site impurity potential, the results in

Fig. 3.7 shed light on the case of isovalent doping in which Fe is replaced by Ru. This procedure introduces disorder but, at least nominally, no electronic doping. Experimental efforts have observed that in this case $T_N$ and $T_S$ still decrease with doping, despite no apparent changes in the Fermi surface, but at a slower rate than with non-isovalent doping. Moreover, the critical temperatures do not separate from each other, i.e., no nematic phase is stabilized [102]. Our results lend support to the view that the decrease of $T_N$ and $T_S$ observed with Ru-doping is mainly due to the magnetic dilution introduced by doping rather than by more subtle effects on the electronic density which in turn would affect the nesting of the FS [103, 104, 105, 106]. Experiments have determined that doped Ru is magnetic [125], which would translate to larger values of $S_I$, $S_{NN}$, and $S_{NNN}$ in our model. In fact, the blue triangles (case II) in Fig. 3.7 qualitatively capture the slower decrease rate and negligible separation with impurity doping for $T_N$ and $T_S$ experimentally observed for Ru doping [102] shown in Fig. 3.8.

## 3.5    Properties of the Nematic Phase

Having stabilized a robust nematic regime, let us study its properties.

### 3.5.1    Neutron scattering

Considering the importance of neutron scattering experiments in iron superconductors, we studied the electronic doping dependence of the magnetic structure factor $S(\mathbf{k})$ obtained from the Fourier transform of the real-space spin-spin correlation functions displayed in Fig. 3.4. Experiments indicate that the low-temperature magnetic phase below $T_S = T_N$ in the parent compound develops long range AFM (FM) order along the long (short) lattice constant direction in the orthorhombic lattice. This results in a sharp peak at $\mathbf{k} = (\pi, 0)$ (or at $(0, \pi)$ depending on the direction of the AFM order) that forms above the small spin-gap energy [101]. More importantly for our discussion and results, upon electron-doping the $(\pi, 0)$ neutron peak becomes broader along the direction transverse to the AFM order in the whole energy range [101], creating an intriguing transversely elongated ellipse.
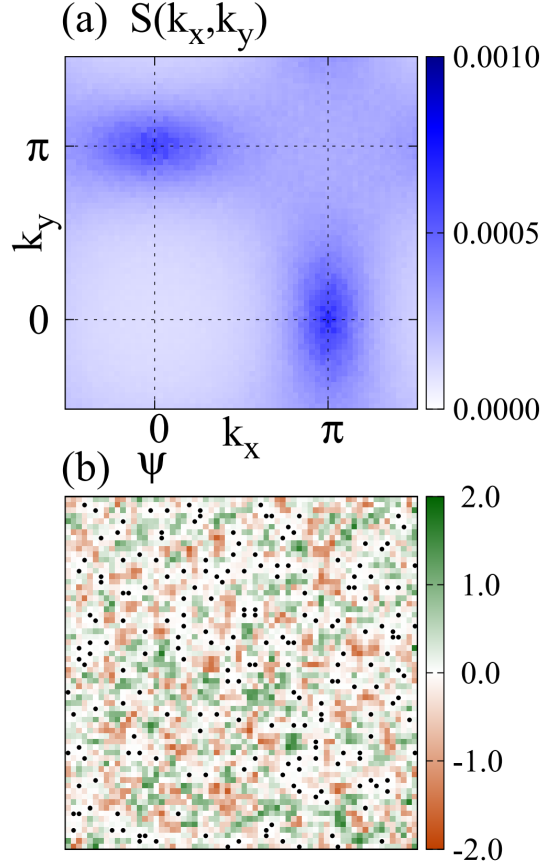
**Figure 3.9:** *Magnetic and nematic order in the paramagnetic regime.* The results are for 5% Co-doping at $T = 120$ K ($T > T_S$) and using a $64 \times 64$ lattice. (a) The magnetic structure factor $S(\mathbf{k})$, showing that the wavevectors $(\pi, 0)$ and $(0, \pi)$ have similar intensity. (b) Monte Carlo snapshot of the spin-nematic order parameter with approximately the same amount of positive (green) and negative (orange) clusters. The impurity sites are indicated by black dots.

The results obtained numerically for 5% Co-doping are shown in Fig. 3.9 for $T = 120$ K ($T > T_S$), i.e. in the paramagnetic phase. In panel (a) peaks in the spin structure factor $S(\mathbf{k})$ (that represents the integral over the whole energy range of the neutron scattering results) with similar intensity at wavevectors $(\pi, 0)$ and $(0, \pi)$ can be observed. Both of these peaks are elongated along the direction transversal to the corresponding spin staggered direction, in agreement with neutron scattering [101]. Our explanation for these results within our spin-fermion model is not associated with Fermi Surface modifications due to electron doping, since the percentual doping is small as already discussed, but instead to the development

of spin-nematic clusters, anchored by the magnetically depleted regions that form at the impurity sites. A Monte Carlo snapshot of the spin-nematic order parameter $\Psi_{\mathbf{i}}$ on a $64 \times 64$ lattice is shown in panel (b) of Fig. 3.9. Since $T > T_S$, patches with $(\pi, 0)$ and $(0, \pi)$ nematic order, indicated with green and orange in the figure, coexist in equal proportion. By eye inspection, we believe that the $(\pi, 0)$ patches tend to be slightly elongated along the $x$ direction, while the $(0, \pi)$ patches are elongated along the $y$ direction. This asymmetry could be the reason for the shape of the peaks in the structure factor displayed in panel (a), since elliptical peaks can be associated to different correlation lengths along the $x$ and $y$ axes. In Fig. 3.9(a) the elliptical $(\pi, 0)$ peak has a correlation length larger along the $x$ axis than the $y$ axis.
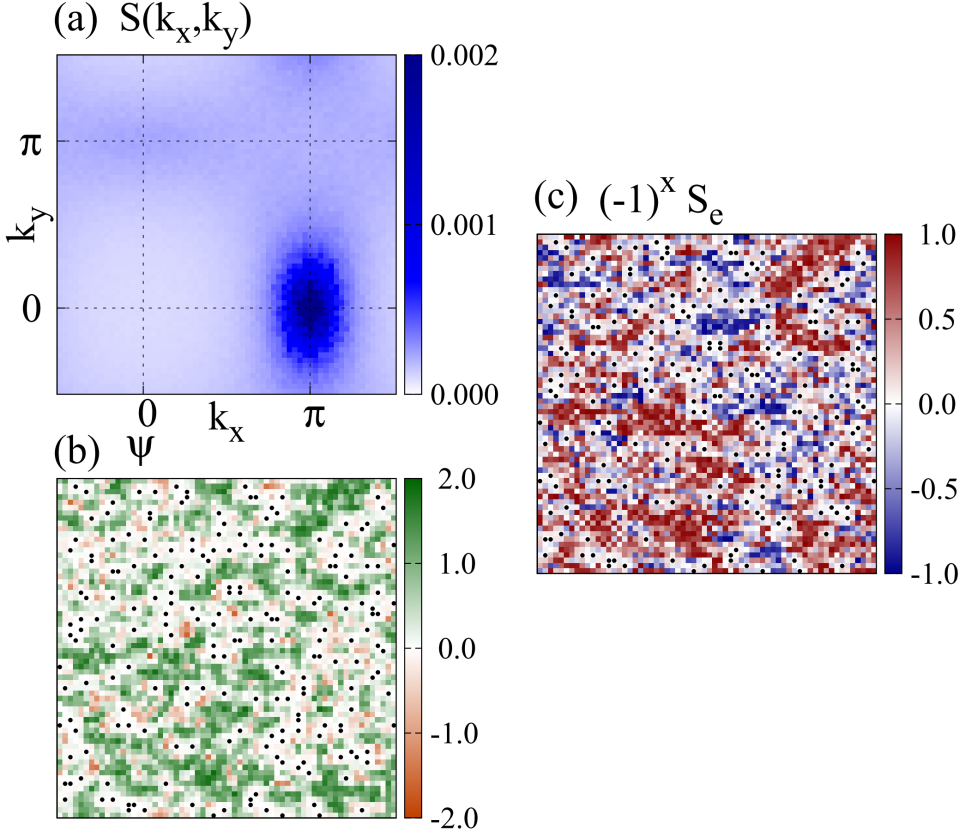
**Figure 3.10:** *Magnetic and nematic order in the nematic regime.* The results are for 5% Co-doping at $T = 95$ K ($T_N < T < T_S$) and using a $64 \times 64$ lattice. (a) The magnetic structure factor $S(\mathbf{k})$ is shown, with clear dominance of the $(\pi, 0)$ state. (b) Monte Carlo snapshot of the spin-nematic order parameter. Impurity sites are indicated by black dots. A positive nematic order (green) dominates, but there are still small pockets of negative order (orange). (c) Monte Carlo snapshot displaying the on-site component along the easy axis, $S_e$, of the localized spin multiplied by the factor $(-1)^{\mathbf{i}_x}$, with $\mathbf{i}_x$ the $x$-axis component of the location of site $\mathbf{i}$. Both the dominant blue and red clusters indicate regions with *local* $(\pi, 0)$ order, but shifted by one lattice spacing. This shift suppresses long-range order when averaged over the whole lattice, but short-range order remains. Impurity sites are denoted as black dots.

The results corresponding to lowering the temperature into the nematic phase ($T = 95$ K) are presented in Fig. 3.10. In this case the subtle effects already observed in the paramagnetic phase are magnified. In panel (a), it is now clear that the peak at $(\pi, 0)$ has developed a much larger weight than the peak at $(0, \pi)$, as expected. Moreover, the elongation along the transversal direction already perceived in the paramagnetic state is now better developed. The Monte Carlo snapshot of the spin-nematic order parameter in panel (b) shows that the

$(\pi, 0)$ (green) regions prevail over the $(0, \pi)$ (orange) regions, indicating that the symmetry under lattice rotations in the nematic phase is spontaneously broken. In addition, now the elongated shape of the $(\pi, 0)$ green clusters along the AFM direction is more clear to the eye. But despite the prevalence of $(\pi, 0)$ clusters the system does not develop long-range magnetic order (compatible with panel (b) of Fig. 3.4). This is because the many $(\pi, 0)$ clusters are actually "out of phase" with each other. This is understood via the visual investigation of Monte Carlo snapshots, as in panel (c) of Fig. 3.10, where it is shown the component of the localized spins along the easy axis, $S_e$, multiplied by a factor $(-1)^{\mathbf{i}_x}$ (see definition in caption; the location of the impurities is indicated with black dots). The abundant red and blue patches all indicate clusters with local $(\pi, 0)$ nematic order, but shifted one with respect to the other by one lattice spacing. The very small regions with $(0, \pi)$ order, as in the orange regions of panel (b), can be barely distinguished in panel (c) with a checkerboard red/blue structure.

### 3.5.2   Scanning Tunneling Microscopy

The real space structure of the $(\pi, 0)$ nematic clusters obtained numerically, with an elongation along the $x$ axis, can be contrasted with Scanning Tunneling Microscopy (STM) measurements. In fact, STM studies of Co-doped $CaFe_2As_2$ at 6% doping [109, 110] have already revealed the existence of unidirectional electronic nanoestructures. These STM structures appear to have an average length of about eight lattice spacings along the AFM direction and it was argued that they may be possibly pinned by the Co atoms. The picture of elongated structures along the $x$ axis is consistent with our results, as shown in panel (b) of Fig. 3.10. However, in our simulation the nematic structures are mainly located in between, rather than on top, the Co dopants. In our case this arises from the fact that the effect of disorder considered here reduces the magnetic interactions at the Co or Cu dopant sites because they are not magnetic.

A recently discussed new perspective is that the nematic state could be a consequence of anisotropic dopant-induced scattering rather than an intrinsic nematic electronic state [108, 126], by studying the anisotropy in the optical spectrum [108] and in the in-plane resistivity [126] varying Co doping in $BaFe_2As_2$. The main argument to attribute the

observed anisotropies to extrinsic effects of Co doping is that the anisotropy increases with doping despite the fact that the spin order weakens and the lattice orthorhombicity diminishes. Our results, by construction, were obtained with impurity profiles that are symmetric under rotations of the lattice, so nematicity is not induced by asymmetric Co doping characteristics. However, we agree with the above described experimental observations that quenched disorder introduced by the dopants is crucial for the stabilization of the nematic phase, otherwise in the "clean limit" there is no difference between $T_S$ and $T_N$ as already explained.

In our simulation, the nematic phase develops because the in-plane dopants allowed the formation of cigar-shaped nematic domains. These domains have shifts in their respective AFM orders, as it can be seen in panel (c) of Fig. 3.10. For the 122 compounds, the dopants enhance the (weak) electronic tendency to nematicity, while according to our previous calculations [79] in the parent compound of materials in the 1111 family, such as ReFeAsO (Re= La, Nd, Sm), a small temperature range of nematicity can be provided by the coupling between the lattice and the orbital degrees of freedom. This view may be supported by studies of the phonon modes in the 1111 materials [127]. Note also that atomic-resolution variable-temperature Scanning Tunneling Spectroscopy experiments performed in NaFeAs, which has $T_S > T_N$, and in LiFeAs, which does not develop neither magnetic order nor a structural transition, indicate that cigar-like nematic domains develop in the nematic phase of NaFeAs regardless of the symmetry of the impurities observed in the samples [97].

## 3.6   Discussion and Conclusions

In the results discussed in this Chapter, the effects of electron doping in materials of the 122 family, such as $BaFe_2As_2$, have been investigated via numerical studies of the spin-fermion model, including charge, orbital, magnetic, and lattice degrees of freedom. These materials are electron doped via the in-plane replacement of iron atoms by transition metals, introducing disorder and dilution effects in the iron layers. The results of our study suggest that the experimentally observed reduction of the magnetic and structural transition temperatures upon doping, in such a manner that $T_N < T_S$, is primarily triggered

by the influence of disorder/dilution associated with the chemical substitution of magnetic Fe atoms by non-magnetic dopants such as Co [121] and Cu [128] as can be seen in Fig. 3.6. More specifically, reducing the magnitude of the localized spins at and near the dopants rapidly reduces the values of both transition critical temperatures. A "patchy" nematic phase is stabilized, which is characterized by a majority of clusters with $(\pi, 0)$ order. These patches have out-of-phase magnetic order separated by non-magnetic regions anchored by the impurities. While the tendency to nematicity is already a property of the purely electronic spin-fermion model, as already discussed in previous studies [79], the present spin-fermion model investigations suggest that for the 122 materials this fragile tendency would not materialize into a robust nematic phase without the influence of disorder/dilution. Compatible with this conclusion, $BaFe_2(As_{1-x}P_x)_2$ (considered among the "cleanest" of doped pnictides since, for example, quantum oscillations were observed [129]) has a splitting between $T_S$ and $T_N$ which is very small (if any).

Note that a mere change in chemical potential to increase the electronic doping, without adding quenched disorder/dilution effects, does *not* stabilize a nematic regime in our model and induces a very small decrease in the transition temperatures. This suggests that nesting effects may not play a major role in the opening of a robust nematic window with doping in 122 materials. Our results can also rationalize the slower decrease of the critical temperatures, and lack of separation between $T_N$ and $T_S$, observed upon Ru doping. In this case experiments have shown that Ru dopants in 122 materials are magnetic [125], contrary to the non-magnetic nature of Co and Cu dopants. Thus, in our study the values of the Hund and Heisenberg couplings would have to be only slightly reduced at the impurity sites. As shown in Fig. 3.7, this will reduce the rate of decrease, as well as the separation, of $T_N$ and $T_S$. The same effect may explain why $T_N = T_S$ and the decrease rate is slower in hole doped systems where the holes are introduced by replacing Ba atoms reducing the effects of disorder/dilution directly in the iron layers.

In addition, the observed clusters are elongated along the AFM direction, results compatible with observations in STM experiments. Within the spin-fermion model, the cigar-like shape of the clusters arises because the nearest-neighbor couplings are AFM and, thus, fluctuations are expected to be larger along the FM (frustrated) direction which reduces

the associated correlation length. Another consequence of this behavior is the oval shape observed for the weight distribution of the magnetic structure factor around the momenta $(\pi, 0)$ and $(0, \pi)$ for $T > T_N$, in agreement with the distribution observed in the electron-doped case in neutron scattering experiments.

In summary, this chapter reports the first computational study of a realistic model for pnictides that reproduces the rapid drop of $T_N$ and $T_S$ with the chemical replacement of Fe by transition metal elements such as Co or Cu. Since disorder and dilution affect differently $T_N$ and $T_S$, a robust nematic regime is stabilized. The key ingredient is the introduction of impurity profiles that affect several neighbors around the location of the dopant. Fermi Surface nesting effects were found to be too small to be the main source responsible for the fast drop of critical temperatures, at least in our model. In real systems it is conceivable that a combination of Fermi Surface nesting effects and disorder/dilution effects could be simultaneously at play. Our results are also compatible with neutron scattering and also with Scanning Tunneling Microscopy. Considering the present results for doped systems, together with the previously reported results for the parent compounds in Ch. 2 and Ref. [79], it can be concluded that the spin-fermion model captures the essence of the magnetic properties of the pnictide iron superconductors. This, however, is not true of the iron chalcogenide, FeTe, whose magnetic order and structural distortion are different. In the next Chapter, a spin fermion model will be proposed that can reproduce these properties through a symmetry argument similar to the one used to capture the properties of the pnictides.

# Chapter 4

# Bicollinear Magnetic order and Monoclinic Lattice Distortion in Iron Telluride

This chapter is a modified version of PHYSICAL REVIEW LETTERS 117, 117201 (2016) [43, 130].

## 4.1   Introduction

The chalcogenide FeTe is an unusual member of the iron-based superconductors family [12, 70, 131, 132]. Angle-resolved photoemission (ARPES) [133] for FeTe revealed substantial mass renormalizations indicative of electrons that are more strongly interacting than in pnictides (see also Ref. [134]). The absence of Fermi surface (FS) nesting instabilities was also established [135, 136]. Moreover, using single-crystal neutron diffraction, "bicollinear" magnetism was reported in FeTe [41, 137]. This exotic antiferromagnetic (AFM) state is known as the E-phase in manganites [82]. Phenomenological approaches rationalize the bicollinear state based on Heisenberg $J_1$-$J_2$-$J_3$ models [138] if the furthest distance coupling $J_3$ is assumed to be robust. Effective spin models [138, 139] are certainly valid descriptions after the lattice distortion occurs, but they do not illuminate the fundamental reasons for the bicollinear state stability [140, 141, 142].

Upon cooling, experimentally the bicollinear state is reached via a robust first-order phase transition [41, 137, 143, 144], with a concomitant tetragonal ($\mathcal{T}_{\mathrm{etra}}$) to monoclinic ($\mathcal{M}_{\mathrm{ono}}$) lattice distortion. The reported distortions in $\mathrm{Fe}_{1.076}\mathrm{Te}$ and $\mathrm{Fe}_{1.068}\mathrm{Te}$ are $\delta_M = |a_M - b_M|/(a_M + b_M) \sim 0.007$ [41, 137] ($a_M$ and $b_M$ are the low temperature lattice parameters in the $\mathcal{M}_{\mathrm{ono}}$ notation). This distortion is comparable to the orthorhombic ($\mathcal{O}_{\mathrm{rth}}$) lattice distortion in $\mathrm{BaFe}_2\mathrm{As}_2$ [145] $\delta_O = |a_O - b_O|/(a_O + b_O) \sim 0.004$ (now with $a_O$ and $b_O$ the low temperature lattice parameters in the $\mathcal{O}_{\mathrm{rth}}$ notation). Since the lattice is considered a "passenger" in the pnictides, it may be suspected that it also plays a secondary role for chalcogenides [146].

Contrary to this reasoning, here we argue that the lattice may play a more fundamental role in FeTe than previously anticipated. Specifically, we construct a spin-fermion (SF) model where lattice and spins are coupled in a manner that includes the $\mathcal{M}_{\mathrm{ono}}$ distortion of FeTe. Using Monte Carlo techniques, we found a strong first-order $\mathcal{T}_{\mathrm{etra}}$ to $\mathcal{M}_{\mathrm{ono}}$ lattice transition, as in experiments [41, 137]. Moreover, the bicollinear magnetic order spontaneously arises at the same critical temperature. All this is achieved with a (dimensionless) spin-lattice coupling $\tilde{g}_{12} \gtrsim 0.10 - 0.25$ (defined in Appendix E) that is not strong. Surprisingly, we also find the same puzzling *reversed* anisotropy in the low temperature resistivity recently reported [147, 148], with the AFM direction more resistive than the ferromagnetic (FM), contrary to results in pnictides (See Fig. 4.1).
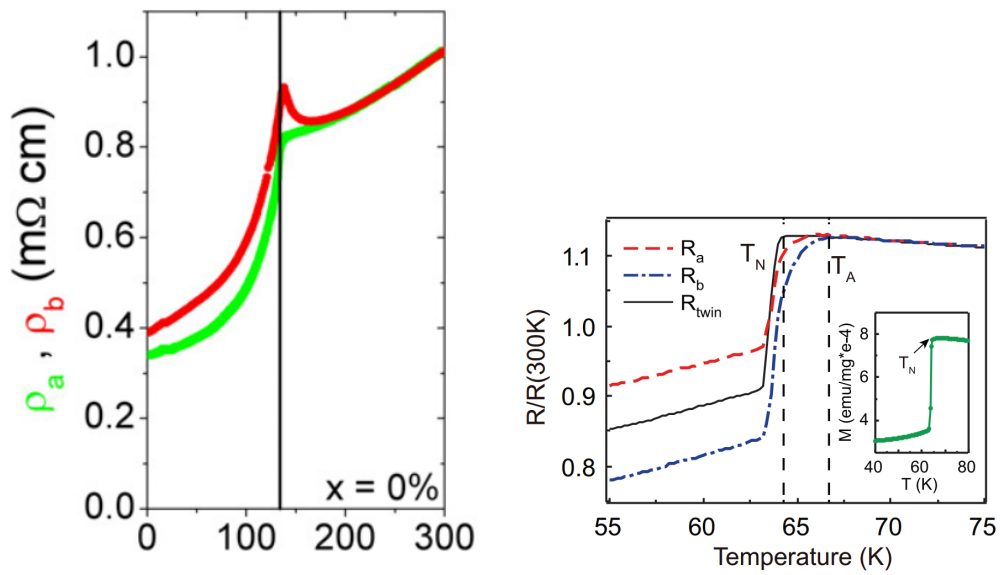
**Figure 4.1:** (Left) Plot Showing the resistance measured along the AFM($\rho_a$ in green) and FM($\rho_b$ in red) directions for $BaFe_2As_2$. This figure is reproduced from Ref. [71]. (Right) Plot showing the Resistance(T)/Resistance(300K) vs Temperature along the AFM(red) and FM (blue) directions as well as for the twinned sample (black). This demonstrates the resistance anisotropy for FeTe. The inset shows the magnetization measurement used to find $T_N$. This figure is reproduced from Ref. [148].

We also include the spin-lattice coupling $\tilde{g}_{66}$ that favors orthorhombicity, although in this case the crystal's geometry – with nearest-neighbors (NN) and next-NN (NNN) hoppings of similar strength and associated FS nesting – already favors the concomitant $(\pi, 0)$ collinear magnetism even without the lattice. Our analysis interpolates between (collinear) pnictides and (bicollinear) chalcogenides using the *same* hopping amplitudes because band structure calculations give similar results for both. In fact, the high temperature regime displays a FS with the canonical hole-electron pockets, naively suggesting that only $\mathcal{O}_{\mathrm{rth}}$ and $(\pi, 0)$ spin order could be stabilized. However, our calculations show that strong first-order transitions can induce a low-temperature state with no precursors at high temperatures.

The presence of both itinerant and localized characteristics in neutron experiments for $Fe_{1.1}Te$ [149] suggests that the SF model provides a proper framework. While we cannot fully incorporate the electronic interactions, the Hund coupling of the SF model mimics a Hubbard $U$ by reducing double occupancy at each orbital [136]. In these respects, our study has the same accuracy as in the successful description of manganites [82, 150].
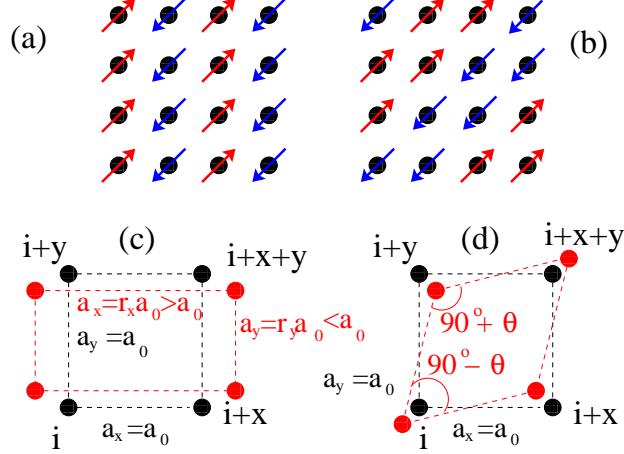
**Figure 4.2:** (a) The collinear $(\pi, 0)$ AFM ordered state; (b) the bicollinear $(\pi/2, -\pi/2)$ AFM ordered state; (c) schematic drawing of the Fe lattice equilibrium position in the $\mathcal{T}_{\text{etra}}$ (black symbols) and $\mathcal{O}_{\text{rth}}$ (red symbols) phases (four Fe's are indicated with filled circles and labeled by their site index $\mathbf{i}$); (d) Same as (c) but for the $\mathcal{M}_{\text{ono}}$ case.

## 4.2  Model

The SF Hamiltonian used here is based on the original purely electronic model [52, 61], supplemented by couplings to the lattice degrees of freedom [68, 79] similar to Sec. 3.2, however, a new term as been added to address the $B_{2g}$ spin-lattice coupling:

$$H_{\text{SF}} = H_{\text{Hopp}} + H_{\text{Hund}} + H_{\text{Heis}} + H_{\text{Stiff}} + H_{\text{SLO}} + H_{\text{SLM}}. \tag{4.1}$$

$H_{\text{Hopp}}$ is the three-orbital ($d_{xz}$, $d_{yz}$, $d_{xy}$) tight-binding Fe-Fe hopping of electrons, with hopping amplitudes selected to reproduce ARPES data [see Eqs. A.3-A.5 and Table A.1 of Appendix A]. The undoped-limit average electronic density per iron and per orbital is $n=4/3$ [56] and a chemical potential in $H_{\text{Hopp}}$ [68] controls its value. The Hund interaction is $H_{\text{Hund}}=-J_{\text{H}} \sum_{\mathbf{i},\alpha} \mathbf{S_i} \cdot \mathbf{s}_{\mathbf{i},\alpha}$, where $\mathbf{S_i}$ are localized spins at site $\mathbf{i}$ and $\mathbf{s}_{\mathbf{i},\alpha}$ are itinerant spins corresponding to orbital $\alpha$ at the same site [151]. Electrons in the non-itinerant orbitals $d_{x^2-y^2}$ and $d_{3z^2-r^2}$ are assumed to have hopping amplitudes smaller than for the itinerants, thus effectively increasing their Hubbard $U$ to bandwidth $W$ ratio. For this reason, a strong coupling expansion generates $H_{\text{Heis}}$ that contains the NN and NNN Heisenberg interactions among those localized spins, with respective couplings $J_{\text{NN}}$ and $J_{\text{NNN}}$, and ratio $J_{\text{NNN}}/J_{\text{NN}}$ $= 2/3$ [152]. The NN and NNN Heisenberg couplings are comparable because Fe-Fe hopping

occurs via Te atoms at the center of Fe plaquettes [153]. However, we will show that $J_{\mathrm{NN}}$ and $J_{\mathrm{NNN}}$ are not crucial for our main conclusions. Finally, $H_{\mathrm{Stiff}}$ is the lattice stiffness (Lennard-Jones potential) to speed up convergence [68, 79].

Previous SF model investigations addressed the $\mathcal{T}_{\mathrm{etra}}-\mathcal{O}_{\mathrm{rth}}$ transition as in SrFe$_2$As$_2$ [79]. The coupling of the spins with the $\mathcal{O}_{\mathrm{rth}}$ lattice distortion [79] is given by $H_{\mathrm{SLO}}= -g_{66}\sum_{\mathbf{i}}\Psi_{\mathbf{i}}^{NN}\epsilon_{66}(\mathbf{i})$ [35, 75], where $g_{66}$ is the canonical $\mathcal{O}_{\mathrm{rth}}$ spin-lattice coupling [84] and the spin NN nematic order parameter is

$$\Psi_{\mathbf{i}}^{NN} = \frac{1}{2}\mathbf{S}_{\mathbf{i}} \cdot (\mathbf{S}_{\mathbf{i+y}} + \mathbf{S}_{\mathbf{i-y}} - \mathbf{S}_{\mathbf{i+x}} - \mathbf{S}_{\mathbf{i-x}}), \tag{4.2}$$

where $\mathbf{x}$ and $\mathbf{y}$ are unit vectors along the $x$ and $y$ axes, respectively.

$\Psi_{\mathbf{i}}^{NN}$ is 2 in the perfect $(\pi,0)$ state shown in Fig. 4.2(a). $\epsilon_{66}(\mathbf{i})$ is the lattice $\mathcal{O}_{\mathrm{rth}}$ strain defined in terms of the positions of the As, Se or Te atoms with respect to their neighboring Fe. Its precise definition is [79]

$$\epsilon_{66}(\mathbf{i}) = \frac{1}{4\sqrt{2}}\sum_{\nu=1}^{4}(|\delta_{\mathbf{i},\nu}^{y}| - |\delta_{\mathbf{i},\nu}^{x}|), \tag{4.3}$$

where $\delta_{\mathbf{i},\nu} = (\delta_{\mathbf{i},\nu}^{x}, \delta_{\mathbf{i},\nu}^{y})$ ($\nu=1,...,4$) is the distance between Fe at $\mathbf{i}$ and one of its four neighbors As or Te (Fig. E.1). The As/Te atoms move locally from their equilibrium position only along the $\hat{x}$ and $\hat{y}$ directions since the displacements along the $\hat{z}$ direction do not couple to the orthorhombic lattice distortion. Both $\Psi_{\mathbf{i}}^{NN}$ and $\epsilon_{66}(\mathbf{i})$ transform as the $B_{1\mathrm{g}}$ representation of the $D_{4\mathrm{h}}$ group.

The crucial novel term $H_{\mathrm{SLM}}=-g_{12}\sum_{\mathbf{i}}\Psi_{\mathbf{i}}^{NNN}\epsilon_{12}(\mathbf{i})$ introduced here provides the coupling between the spin and the $\mathcal{M}_{\mathrm{ono}}$ lattice distortion [154], with strength $g_{12}$. The spin NNN nematic order parameter is

$$\Psi_{\mathbf{i}}^{NNN} = \frac{1}{2}\mathbf{S}_{\mathbf{i}} \cdot (\mathbf{S}_{\mathbf{i+x+y}} + \mathbf{S}_{\mathbf{i-x-y}} - \mathbf{S}_{\mathbf{i+x-y}} - \mathbf{S}_{\mathbf{i-x+y}}). \tag{4.4}$$
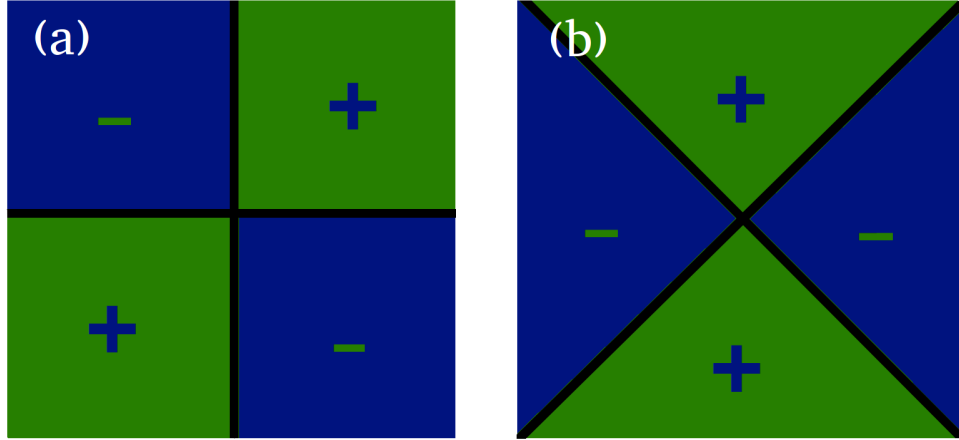
**Figure 4.3:** (a) Example of the $B_{2g}$ representation of the $D_{4h}$ group. (b) Example of the $B_{1g}$ representation of the $D_{4h}$ group.

$\Psi_{\mathbf{i}}^{NNN}$ becomes 2 in the perfect $(\frac{\pi}{2}, -\frac{\pi}{2})$ state of Fig. 4.2(b) [155]. $\epsilon_{12}(\mathbf{i})$ is the lattice $\mathcal{M}_{\text{ono}}$ strain defined in terms of the Fe-Te/As distances $\delta_{\mathbf{i}, \nu}$ as

$$\epsilon_{12}(\mathbf{i}) = \frac{1}{8}(|\delta_{\mathbf{i},2}| + |\delta_{\mathbf{i},4}| - |\delta_{\mathbf{i},1}| - |\delta_{\mathbf{i},3}|). \tag{4.5}$$

$\epsilon_{12}(\mathbf{i})$ transforms as the $B_{2g}$ representation. For this reason we must use $\Psi_{\mathbf{i}}^{NNN}$, that also transforms as $B_{2g}$, in $H_{\text{SLM}}$ so that it is invariant under the $D_{4h}$ group (See Fig. 4.3(a)). This simple symmetry argument is the reason for why the bicollinear state is stabilized by the monoclinic distortion. As mentioned previously in Sec. 2.2, $B_{1g}$ transformations can be described by $\frac{\pi}{2}$ rotations that lead to a change of sign in the order parameter (See Fig. 4.3(b)). $B_{2g}$ transformations also lead to a change in sign upon $\frac{\pi}{2}$ rotations about the $\hat{z}$ axis, but they differ from $B_{1g}$ because they are even under reflections on a plane along the diagonal directions of the Fe plaquette as shown in Fig. 4.3(a).

$H_{\text{SF}}$ was studied with the same Monte Carlo (MC) procedure employed in [79] (see also Appendix E and Ref. [156]). Here only a detailed description of the new lattice coupling $\tilde{g}_{12}$ will be provided. During the simulation the As/Te atoms can move locally away from their equilibrium positions on the $x$-$y$ plane, while the Fe atoms can move globally in two ways: (i) via an $\mathcal{O}_{\text{rth}}$ distortion characterized by a global displacement $(r_x, r_y)$ from the equilibrium position $(x_i^{(0)}, y_i^{(0)})$ of each iron with $r_\alpha = 1 + \Delta_\alpha$ ($\Delta_\alpha \ll 1$; $\alpha = x$ or $y$) [Fig. 4.2 (c)], and (ii)

via a $\mathcal{M}_{\mathrm{ono}}$ distortion where the angle between two orthogonal Fe-Fe bonds is allowed to change globally to $90^o + \theta$ with the four angles in the $\mathcal{M}_{\mathrm{ono}}$ plaquette adding to $360^o$ so that the next angle in the plaquette becomes $90^o - \theta$, with $\theta$ a small angle [Fig. 4.2 (d)]. In addition, the localized (assumed classical) spins $\mathbf{S_i}$ and atomic displacements $(\delta_{\mathbf{i},\nu}^x, \delta_{\mathbf{i},\nu}^y)$ that determine the $\mathcal{O}_{\mathrm{rth}}$ or $\mathcal{M}_{\mathrm{ono}}$ lattice distortion $\epsilon_{66}(\mathbf{i})$ [68, 79] and $\epsilon_{12}(\mathbf{i})$ are also MC evaluated. In Appendix E the spin and lattice susceptibilities $\chi_{S(k_x,k_y)}$, $\chi_{\delta_O}$, and $\chi_{\delta_M}$, and the dimensionless couplings $\tilde{g}_{66}$ and $\tilde{g}_{12}$ are defined.
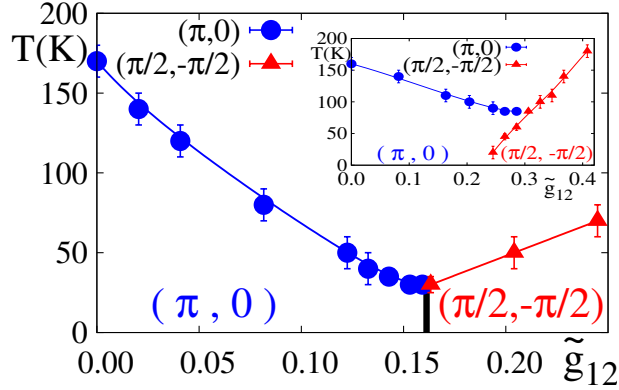


**Figure 4.4:** Phase diagram along the straight line from $(\tilde{g}_{12}, \tilde{g}_{66}) = (0, 0.24)$ to $(0.24, 0)$, at $J_{\mathrm{H}}$=0.1 eV and $J_{\mathrm{NN}}$=$J_{\mathrm{NNN}}$=0. *Inset:* same phase diagram but along the straight line from $(\tilde{g}_{12}, \tilde{g}_{66}) = (0, 0.16)$ to $(0.40, 0)$, at $J_{\mathrm{H}}$=0.1 eV, $J_{\mathrm{NN}}$=0.012 eV, and $J_{\mathrm{NNN}}$=0.008 eV. Blue circles (red triangles) denote $T_{\mathrm{O}}$ ($T_{\mathrm{M}}$), the transition temperatures to the $\mathcal{O}_{\mathrm{rth}}$/collinear ($\mathcal{M}_{\mathrm{ono}}$/bicollinear) phase.

## 4.3 Results

In real chalcogenides, both $B_{1\mathrm{g}}$ and $B_{2\mathrm{g}}$ magnetic fluctuations should be present and the magnitude of their respective couplings to $\mathcal{O}_{\mathrm{rth}}$ and $\mathcal{M}_{\mathrm{ono}}$ distortions depends on doping, replacing Te by Se, or iron excess as in $Fe_{1+y}$Te. In addition, weak $B_{2\mathrm{g}}$ fluctuations may also exist in pnictides.

For this reason, our study will address the MC phase diagrams varying temperatures and couplings in a wide range. Consider first the case $J_{\mathrm{NN}} = J_{\mathrm{NNN}} = 0$. One of our most important results is in Fig. 4.4. At the left, a realistic $T_{\mathrm{O}}^{max} \approx 170$ K is obtained for the transition to the collinear/$\mathcal{O}_{\mathrm{rth}}$ state, with an $\mathcal{O}_{\mathrm{rth}}$ distortion $\delta_O \approx 0.004 - 0.008$, compatible

with experiments [41, 137] and previous studies [79]. As $\tilde{g}_{12}$ increases and $\tilde{g}_{66}$ linearly decreases, then $T_O^{max}$ naturally decreases. When $\tilde{g}_{12} \approx 0.16$ and $\tilde{g}_{66} \approx 0.08$, remarkably now the FeTe bicollinear/$\mathcal{M}_{ono}$ phase appears at $T_M$ (red triangles). At the right in Fig. 4.4 the critical temperature is $\sim 70$ K similar to FeTe experiments [157]. Moreover, in the range shown, the monoclinic lattice distortions are small (for explicit values see Fig. G.3) [158].

Bicollinear order is stabilized because with increasing $\tilde{g}_{12}$ the nematic order parameter $\Psi_\mathbf{i}^{NNN}$ in $H_{SLM}$ becomes nonzero to lower the energy. In each odd-even site sublattice, $\Psi_\mathbf{i}^{NNN}$ favors a state with parallel spins along one diagonal direction and antiparallel in the other (equivalent to the collinear order but rotated by $45^o$). The parallel locking of the two independent spin sublattices leads to the state in Fig. 4.2(b) (or rotated ones).

As already explained, the purely fermionic SF model develops a collinear $(\pi, 0)$ tendency because of FS nesting in the tight-binding sector [61]. Since spin and lattice are linearly coupled, an $\mathcal{O}_{rth}$ distortion is induced even for an infinitesimal $\tilde{g}_{66}$. On the other hand, regardless of $\tilde{g}_{66}$, the coupling $\tilde{g}_{12}$ needed to stabilize the bicollinear/$\mathcal{M}_{ono}$ state is *finite* because it must first "fight" against the $(\pi, 0)$ order. However, in practice this critical coupling is small $\sim 0.1$-$0.25$ and within experimental range.

To analyze the universality of the Fig. 4.4 phase diagram we also investigated the effect of adding NN and NNN Heisenberg couplings along the line from $(\tilde{g}_{12}, \tilde{g}_{66}) = (0, 0.16)$ to $(0.40, 0)$ (inset of Fig. 4.4). Qualitatively the results are similar.

At $(0.40, 0)$ in the inset, the largest value of $\tilde{g}_{12}$ considered here, the $\mathcal{M}_{ono}$ distortion is $\delta_M \approx 0.004$ still compatible with experiments [41, 137]. One interesting difference, though, between the two cases is the appearance of an intermediate region at $\tilde{g}_{12} \approx 0.28$ in Fig. 4.4(inset) where upon heating a transition $\mathcal{M}_{ono}$ to $\mathcal{O}_{rth}$ is reached before the system eventually becomes paramagnetic. Experimentally in $Fe_{1+y}Te$ an intermediate $\mathcal{O}_{rth}$ phase with incommensurate magnetic order indeed exists between the $\mathcal{T}_{etra}$ and $\mathcal{M}_{ono}$ phases [154, 157] with $T_O \approx 60$ K and $T_M \approx 50$ K, at $y \approx 0.13$. Our finite lattices do not have enough resolution to study the subtle incommensurate magnetism but we conjecture that adding Fe to FeTe may effectively increase the spin-lattice coupling to reach the inset intermediate regime.
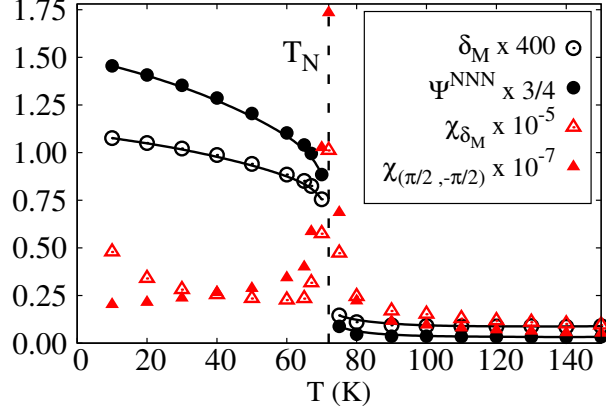
**Figure 4.5:** Filled (open) circles indicate the bicollinear AFM order parameter $\Psi^{NNN}$ (the $\mathcal{M}_{\mathrm{ono}}$ lattice distortion $\delta_M$) at $\tilde{g}_{12} = 0.24$, $\tilde{g}_{66} = 0$, $J_{\mathrm{H}} = 0.1$ eV, and $J_{\mathrm{NN}} = J_{\mathrm{NNN}} = 0$. Magnetic and lattice susceptibilities, $\chi_{(\pi/2,-\pi/2)}$ and $\chi_{\delta_M}$, are also shown (filled and open triangles, respectively). $T_{\mathrm{N}}$ denotes the first-order Néel temperature.

Another interesting result found here is that the bicollinear/$\mathcal{M}_{\mathrm{ono}}$ phase transition is strongly first order, as in experiments [41, 137], as indicated by the order parameters discontinuities in Fig. 4.5 and by the MC-time evolution histogram Fig. 4.6(a). At high temperature $(\pi, 0)$ fluctuations first develop (as implied by the inset of Fig. 4.4), leading to a free energy local minimum. However, upon further cooling the bicollinear minimum with a different symmetry also develops and eventually a crossing occurs with first-order characteristics because one local state cannot evolve smoothly into the other.

Remarkably, the correct behavior for the resistivity anisotropy of FeTe [147, 148] is also observed here (details in Appendix F and I ). In the $(\pi, 0)$ phase, FS nesting opens a pseudogap for the $yz$ orbital [61, 79, 159]. Because this orbital relates to electronic hopping along the ferromagnetic $y$-axis, then the FM resistivity is the largest in pnictides (See Fig. 4.1(Left)). However, the *reversed* anisotropy with lower resistance along the FM direction (open circles) was found in the bicollinear phase Fig. 4.6(b) (the technique used is explained in Appendix F). This can be compared to the experimental results in Fig. 4.1(Right) which shows the same *reversed* anisotropy for FeTe [148]. Moreover, this reversed effect is amplified as $J_{\mathrm{H}}$ increases. The key clues to explain the effect are now clear: (i) an electron hopping along the plaquette diagonal in the AFM direction pays an energy $J_{\mathrm{H}}$, but the hopping along the plaquette diagonal FM direction does not; (ii) because FS nesting does not involve wavevectors such as $(\pi/2, -\pi/2)$, then pseudogaps are not created due to

66

nesting as in pnictides. Then, in essence, the reversed resistance found here is characteristic of large Hund coupling materials [160], such as manganites [82], where it is also known that the AFM direction is more resistive than the FM direction.
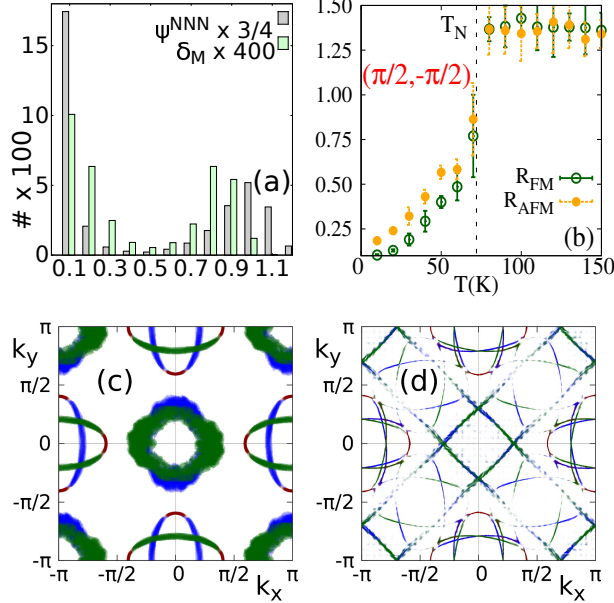


**Figure 4.6:** (a) Histogram of the MC time evolution of $\Psi^{NNN}$ and $\delta_M$, at the critical temperature of Fig. 4.5 ($T = 72$ K), illustrating its bimodal character compatible with first-order characteristics. (b) Resistance ($h/2e^2$ units) vs. temperature in the bicollinear state ($\tilde{g}_{12} = 0.24$, $\tilde{g}_{66} = 0$, $J_H = 0.2$ eV, no Heisenberg terms). Filled (open) symbols denote resistivities along the AFM (FM) direction. (c,d) Symmetrized Fermi surface ($\tilde{g}_{12} = 0.24$, $\tilde{g}_{66} = 0$, $J_H = 0.2$ eV, no Heisenberg terms). (c) is in the high temperature paramagnetic phase ($T = 360$ K); (d) is in the bicollinear phase ($T = 10$ K). The FS orbital composition notation is blue ($xz$), green ($yz$), and red ($xy$). In the non-symmetrized FS (not shown) a gap opens along the AFM diagonal direction in the $xz$ and $yz$ orbitals, compatible with the resistivity results.

A paradox of FeTe is that first principles studies predict FS nesting and, thus, $(\pi, 0)$ order as in pnictides. For this reason, we calculated the FS at couplings where the ground state is $\mathcal{M}_{\text{ono}}$. Figure 4.6 (c) shows the FS in the high temperature $\mathcal{T}_{\text{etra}}$ state. It is similar to that of the iron pnictides, suggesting $(\pi, 0)$ order upon cooling (the $\Gamma$ centered features are blurry because of how a shallow pocket is affected by temperature). However, because of the sharp first-order transition the $\mathcal{M}_{\text{ono}}$ state reached at low temperature has a peculiar FS [Fig. 4.6 (d)]: while the electron pockets are similar, the squarish $\Gamma$ hole pocket is different from that of pnictides. In addition "shadow bands" at $(\pm\frac{\pi}{2}, \pm\frac{\pi}{2})$ develop, as in ARPES [135], indicative of couplings stronger than for pnictides [161].

## 4.4  Discussion

Using computational techniques applied to the SF model including a spin-lattice $\mathcal{M}_{\mathrm{ono}}$ distortion in the $B_{2\mathrm{g}}$ channel, we showed that the puzzling phenomenology of FeTe is well reproduced. This includes the presence of bicollinear magnetic order, $\mathcal{M}_{\mathrm{ono}}$ lattice distortions, a strong first-order $\mathcal{T}_{\mathrm{etra}}$-$\mathcal{M}_{\mathrm{ono}}$ transition, nested Fermi surfaces at high temperature naively favoring collinear order, and last but not least also the low-temperature reversed anisotropic resistances between the AFM and FM directions. Moreover, all this is achieved with spin-lattice dimensionless couplings less than 1, and with associated small lattice distortions $\delta_M \sim 10^{-3}$. While in pnictides the resistance anisotropy is related to FS nesting and a $yz$ orbital pseudogap [159], in chalcogenides the strength of the Hund coupling is crucial. To our knowledge, the spin-lattice interaction discussed here provides the first comprehensive explanation of the challenging experimental properties of FeTe. In these results, the structural and magnetic transitions are simultaneous. This is not surprising considering that in Ref. [79] an orbital-lattice coupling was necessary to separate the two. In the following chapter it will be shown that a $B_{2g}$ orbital-lattice coupling can be added to the spin fermion model to stabilize a $B_{2g}$ nematic phase.

# Chapter 5

# Possible Bicollinear Nematic State with Monoclinic Lattice Distortions in Iron Telluride Compounds

This chapter is a modified version of PHYSICAL REVIEW B 96, 035144 (2017) [162, 163].

## 5.1 Introduction

The theoretical understanding of high critical temperature superconductivity in iron compounds has evolved from its early qualitative developments based on Fermi surface nesting to more quantitative efforts incorporating the role of electronic correlations [12, 23, 36, 70, 114, 131]. In particular, experts have focused on several complex regimes including electronic nematicity [35, 71, 75], an interesting state observed in several high critical temperature pnictide superconductors [10, 30, 164, 165]. Upon cooling, this nematic phase is reached at a temperature $T_S$, concomitantly with a structural phase transition from a tetragonal to an orthorhombic lattice. Upon further cooling a magnetically ordered phase is stabilized at a lower temperature $T_N$. The orthorhombic nematic phase between $T_S$ and $T_N$ exhibits a reduced symmetry under rotations from $C_4$ to $C_2$. This is also observed in the

magnetic and orbital degrees of freedom leading to nonzero magnetic and orbital "nematic" order parameters. Experimental investigations have shown that this nematic phase occurs in the parent compounds of the 1111 pnictides [30]. Since the orthorhombic lattice distortion $\delta_O = |a_O - b_O|/(a_O + b_O) \sim 0.004$ [145] is small ($a_O$ and $b_O$ are the lattice parameters in the orthorhombic notation), it is often argued that the lattice plays the role of a "passenger" in the nematic transition, which is believed to be driven by either the magnetic or orbital degrees of freedom. In addition, it is interesting to notice that the structural transition occurs simultaneously with the Néel temperature in several other iron-based materials. For example, members of the 122 family need to be electron doped, with the chemical replacement occurring directly on the FeAs planes, to develop the nematic phase [10, 164, 165]. Hole doping, or electron doping via chemical substitution away from the FeAs planes, fails to establish nematicity [101, 166].

In the chalcogenides, the parent compound FeTe exhibits an unexpected "bicollinear" magnetic state [41, 82, 137], shown in panels (a,b) of Fig. 5.1, whose $T_N$ coincides with the $T_S$ of a structural transition to a phase with a monoclinic lattice distortion, as shown in panel (d) of the same figure. This joint transition is strongly first order [137, 143, 144]. The reported lattice distortions in $Fe_{1.076}Te$ and $Fe_{1.068}Te$ are $\delta_M = |a_M - b_M|/(a_M + b_M) \sim 0.007$ [137] ($a_M$ and $b_M$ are the low-temperature lattice parameters in the monoclinic notation) where in Eq. E.7 of Appendix E, it is shown that $\delta_M \approx \frac{\theta}{2}$. Replacing Te with Se the bicollinear magnetic order is eventually lost, the material becomes superconducting, and it develops an orthorhombic nematic phase above its superconducting critical temperature. In recent theoretical work, using a spin-fermion model we explained the bicollinear magnetic order using symmetry considerations as a consequence of the monoclinic distortion [43, 132, 167]. Based on this reasoning, the role of the lattice in the case of FeTe appears more important than previously anticipated.

The aim of the present work is to argue that the pnictides and chalcogenides could potentially behave more symmetrically with regards to the presence of a nematic state. As expressed above, the pnictides either already have nematicity without doping, as in the 1111 compounds, or develop nematicity after doping as in the Co-doped 122 compounds. Based on symmetry arguments, the presence of a nematic regime is theoretically understood as

follows. In these materials the magnetic ground state has wavevector $(\pi, 0)$, with staggered spins along the $x$-axis and parallel spins along the $y$-axis. However, the $(0, \pi)$ state should have the same energy by symmetry. In cases of two-fold degeneracy in the ground state, it was predicted that an Ising transition could occur upon cooling [168], with an order parameter that breaks lattice rotational invariance and involves only short-range magnetic correlations. Upon further cooling, the O(3) full symmetry breaking process is possible.

Our main observation here is that the bicollinear state shown in Fig. 5.1 (a) with wavevector $\mathbf{k_1} = (\pi/2, -\pi/2)$ has a partner, displayed in Fig. 5.1 (b), with identical energy but $\mathbf{k_2} = (\pi/2, \pi/2)$ [169]. Then, the same Ising-O(3) rationale expressed above for the $(\pi, 0) - (0, \pi)$ degeneracy can be repeated for bicollinear states: starting at high temperature both spin structure factors $S(\mathbf{k})$ will start growing with equal strength upon cooling at the wavevectors $\mathbf{k_1}$ and $\mathbf{k_2}$. By analogy with the pnictides, it is possible that at a critical nematic temperature $T_S$ an asymmetry develops such that $S(\mathbf{k_1}) > S(\mathbf{k_2})$, and then at a lower temperature $T_N$, $S(\mathbf{k_2})$ drops to zero while $S(\mathbf{k_1})$ grows like the volume.

While no nematic phase with these characteristics has been reported yet in materials of the FeTe family with the bicollinear spin order, the present study provides computational evidence that there are Hamiltonians with spin- and orbital-lattice coupling that display this new nematic behavior, if the couplings strengths are properly tuned. While our many-body tools do not allow us to predict what specific material may display this phenomenon, our symmetry arguments and concrete simulation results are offered as motivation for the experimental search for this exotic bicollinear-nematic state.

Previous numerical studies of spin-fermion models for pnictides with spin, orbital, and lattice degrees of freedom provided indications that the structural transition is due to the coupling between the lattice and spins [79]. Thus, in these regards the lattice follows the spins. But the spin-lattice coupling leads to $T_S = T_N$ and, then, the establishment of a nematic phase with $T_S > T_N$ requires a more subtle mechanism. Investigations by our group have shown that the nematic regime can be achieved by the addition of an orbital-lattice coupling [79] (or by the introduction of in-plane magnetic disorder, namely by replacing iron by non-magnetic atoms [98, 170]). Based on this previous research, here a coupling between the monoclinic lattice distortion and an *orbital* nematic parameter with $B_{2g}$ symmetry will

71
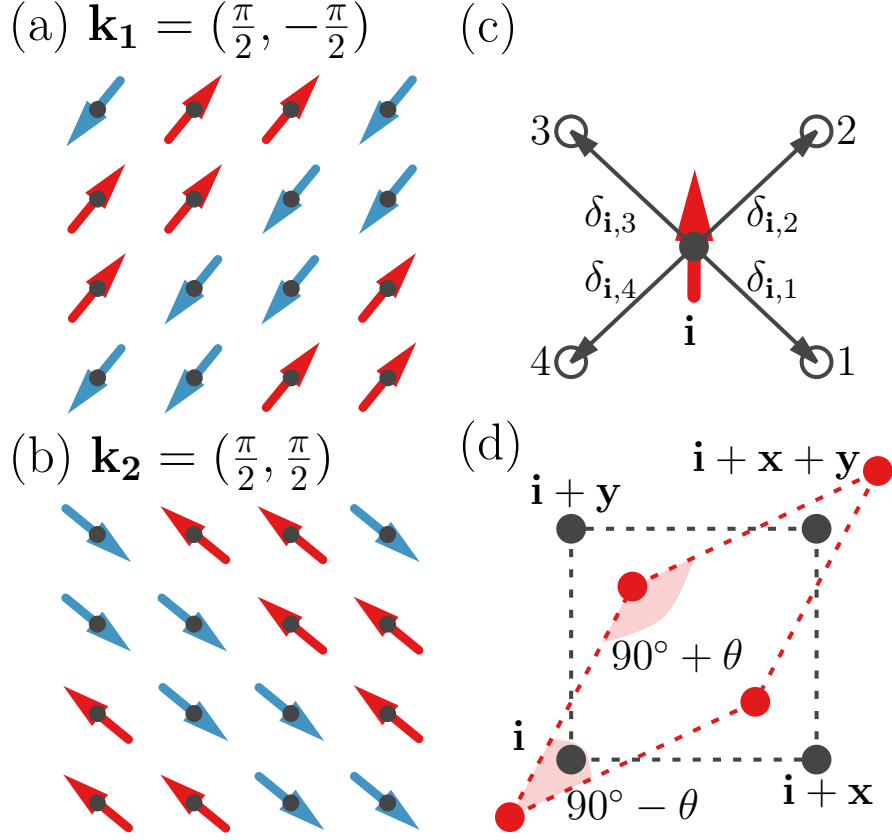
**Figure 5.1:** (a) The bicollinear antiferromagnetic spin order with wavevector $(\pi/2, -\pi/2)$. (b) same as (a) but for the state lattice-rotated by 90 degrees with wavevector $(\pi/2, \pi/2)$. (c) Schematic drawing of an iron atom at site $\mathbf{i}$ (filled symbol) and its four Te neighbors (open symbols), projected in the $x$-$y$ plane in their equilibrium position. The distances $\delta_{\mathbf{i},\nu}$ between the irons at site $\mathbf{i}$ and its four neighboring Te atoms are indicated as well. The localized spin $\mathbf{S_i}$ is also sketched. (d) Schematic drawing of the Fe lattice equilibrium position in the tetragonal phase (black symbols and lines) and in the monoclinic phase (red symbols and lines). Four Fe atoms are indicated with filled symbols and labeled by their lattice site index.

be added to the spin-fermion model that already has the spin-lattice coupling previously developed to study FeTe (See Ch. 4) .

This chapter is organized as follows. In Section 5.2 the model is described including the new term that must be incorporated in order to stabilize a bicollinear-nematic state. In Section 5.3 we provide an explanation of the numerical approach that allows for the parallelization of the Monte Carlo procedure and the concomitant use of clusters of reasonable size for our purposes. The main results showing the stabilization of the new nematic state are presented in Section 5.4. The discussion, including possible physical realizations, is in Section 5.5, with brief conclusions in Section 5.6.

## 5.2 Model

The spin-fermion (SF) Hamiltonian used here is an extension of Sect. 4.2, supplemented by a new $B_{2g}$ orbital-lattice coupling. The $B_{1g}$ spin-lattice coupling which stabilizes the orthorhombic/collinear state, was not included since as can be seen in Ch. 4, it competes with the bicollinear state. The Hamiltonian used is thus given by:

$$H_{\text{SF}} = H_{\text{Hopp}} + H_{\text{Hund}} + H_{\text{Heis}} + H_{\text{Stiff}} + H_{\text{SLM}} + H_{\text{OLM}}. \tag{5.1}$$

More detail on the Hamiltonian can be found in Appendix A and E. $H_{\text{Hopp}}$ represents the three-orbitals ($d_{xz}$, $d_{yz}$, $d_{xy}$) tight-binding Fe-Fe hopping of electrons, with the hopping amplitudes selected to reproduce photoemission data [see Eqs. A.3-A.5 and Table A.1 of Appendix A]. In the undoped-limit the average electronic density per iron and per orbital is set to $n=4/3$ [56] and a chemical potential in $H_{\text{Hopp}}$ [68] controls its value. The on-site Hund interaction is $H_{\text{Hund}}=-J_{\text{H}} \sum_{\mathbf{i},\alpha} \mathbf{S}_{\mathbf{i}} \cdot \mathbf{s}_{\mathbf{i},\alpha}$, where $\mathbf{S}_{\mathbf{i}}$ are the localized spins at site $\mathbf{i}$ and $\mathbf{s}_{\mathbf{i},\alpha}$ are spins corresponding to orbital $\alpha$ of the itinerant fermions at the same site. For computational simplicity, the localized spins are assumed classical and of norm one [151]. $H_{\text{Heis}}$ contains the nearest neighbor (NN) and next-NN (NNN) Heisenberg interactions among the localized spins, with respective couplings $J_{\text{NN}}$ and $J_{\text{NNN}}$. As explained before [61, 79], both NN and NNN are in principle needed because of the geometry of the problem, where in each layer the

Te atoms (or As, Se, P) are at the centers of iron plaquettes as seen from above. However, in our previous study of FeTe [43] we observed that the experimental value of $T_N$ for FeTe could be obtained by simply setting $J_{\mathrm{NN}} = J_{\mathrm{NNN}} = 0$. This is due to the fact that the intersite spin-spin couplings favor either checkerboard ($J_{\mathrm{NN}}$) or collinear ($J_{\mathrm{NNN}}$) magnetic configurations and in order to obtain a bicollinear ground state it is necessary to use a larger value of the spin-lattice coupling $\tilde{g}_{12}$ which, in turn, increases $T_N$ [171]. $H_{\mathrm{Stiff}}$ is the lattice stiffness given by a Lennard-Jones potential to speed up convergence [68] (full expression can be found in Appendix A).

In the previous chapter, a crucial term was introduced [43] to describe FeTe properly. This term has the form $H_{\mathrm{SLM}} = -g_{12} \sum_{\mathbf{i}} \Psi_{NNN}(\mathbf{i}) \epsilon_{12}(\mathbf{i})$ and it provides a coupling between the localized spins and the monoclinic $\mathcal{M}_{\mathrm{ono}}$ lattice distortions [112]. The coupling constant strength is $g_{12}$ and the spin NNN nematic order parameter is defined as

$$\Psi_{NNN}(\mathbf{i}) = \frac{1}{2} \mathbf{S_i} \cdot (\mathbf{S_{i+x+y}} + \mathbf{S_{i-x-y}} - \mathbf{S_{i+x-y}} - \mathbf{S_{i-x+y}}), \tag{5.2}$$

where $\mathbf{i} \pm \mu \pm \nu$ indicates the four NNN sites to $\mathbf{i}$, with $\mu = \pm \mathbf{x}$ and $\nu = \pm \mathbf{y}$ representing unit vectors along the $x$ and $y$ axes, respectively. Note that $\Psi_{NNN}(\mathbf{i})$ has the value 2 (-2) in the perfect bicollinear states shown in Figs. 5.1 (a) and (b), respectively characterized by a peak at wavevectors $(\pi/2, -\pi/2)$ and $(\pi/2, \pi/2)$ in the magnetic structure factor. $\epsilon_{12}(\mathbf{i})$ is the lattice $\mathcal{M}_{\mathrm{ono}}$ strain defined in terms of the Fe-Te distances $\delta_{\mathbf{i},\nu}$ as

$$\epsilon_{12}(\mathbf{i}) = \frac{1}{8}(|\delta_{\mathbf{i},2}| + |\delta_{\mathbf{i},4}| - |\delta_{\mathbf{i},1}| - |\delta_{\mathbf{i},3}|), \tag{5.3}$$

where $\delta_{\mathbf{i},\nu} = (\delta_{\mathbf{i},\nu}^x, \delta_{\mathbf{i},\nu}^y)$ ($\nu$=1,...,4) is the distance between Fe at site $\mathbf{i}$ and each of its four Te neighbors (see panel (c) of Fig. 5.1 and also Fig. E.1). As in previous simulations, the Te atoms are allowed to move locally from their equilibrium position only along the $x$ and $y$ directions since the $z$ direction does not couple to the monoclinic lattice distortion. It is important to notice that both $\Psi_{NNN}(\mathbf{i})$ and $\epsilon_{12}(\mathbf{i})$ transform according to the $B_{2g}$ representation of the $D_{4\mathrm{h}}$ symmetry group, which means that the spin-lattice term of the Hamiltonian transforms as $A_{1g}$ as expected. As the spin-lattice coupling $g_{12}$ grows and

induces a monoclinic $\mathcal{M}_{\mathrm{ono}}$ distortion, $\Psi_{NNN}$ develops a nonzero expectation value leading to the bicollinear spin state order as explained in Sec. 4.3.

The Hamiltonian as described thus far is the same as employed in Sec. 4.2 and leads to a first-order phase transition where both the monoclinic lattice and the bicollinear spin orders develop simultaneously. Thus, no bicollinear-nematic state was found in the studies presented in the previous chapter. Based on previous investigations of pnictides using the spin-fermion model [79], it is natural to introduce a coupling between the lattice and the *orbital* degree of freedom in order to induce nematicity. As mentioned in Sec. 4.2, this requires care with regards to the symmetry of the operators needed for this new term. The monoclinic orbital-nematic order parameter is defined as

$$\Phi_{B_{2g}}(\mathbf{i}) = n_{\mathbf{i},XZ} - n_{\mathbf{i},YZ} = \sum_\sigma (c^\dagger_{\mathbf{i},xz,\sigma} c_{\mathbf{i},yz,\sigma} - c^\dagger_{\mathbf{i},yz,\sigma} c_{\mathbf{i},xz,\sigma}), \tag{5.4}$$

where $n_{\mathbf{i},\beta} = \sum_\sigma c^\dagger_{\mathbf{i},\beta,\sigma} c_{\mathbf{i},\beta,\sigma}$ ($\beta = XZ, YZ$), and the $B_{2g}$ orbital basis is related to the $B_{1g}$ orbital basis by

$$c_{\mathbf{i},XZ,\sigma} = \frac{1}{\sqrt{2}}(c_{\mathbf{i},xz,\sigma} + c_{\mathbf{i},yz,\sigma}) \tag{5.5}$$

and

$$c_{\mathbf{i},YZ,\sigma} = \frac{1}{\sqrt{2}}(c_{\mathbf{i},xz,\sigma} - c_{\mathbf{i},yz,\sigma}). \tag{5.6}$$

Notice that the $x$ and $y$ axes point along nearest-neighbor irons, i.e. along the sides of the plaquette formed by four irons, while the $X, Y$ axes point along next nearest-neighbor iron, i.e. along the diagonals of the iron plaquette. The $Z$ and $z$ axis coincide and they are perpendicular to the plane formed by the iron layer.

The new term in the Hamiltonian $H_{\mathrm{OLM}}$ that couples the $B_{2g}$ orbital and lattice order parameters is given by

$$H_{\mathrm{OLM}} = -\lambda_{12} \sum_{\mathbf{i}} \Phi_{B_{2g}}(\mathbf{i}) \epsilon_{12}(\mathbf{i}). \tag{5.7}$$

Because the monoclinic lattice distortion $\epsilon_{12}(\mathbf{i})$ transforms as the $B_{2g}$ representation of $D_{4h}$, it must be coupled to an orbital order parameter that also transforms as $B_{2g}$, which is why

$\Phi_{B_{2g}}(\mathbf{i})$ was constructed. This ensures that $H_{\mathrm{OLM}}$ is invariant under the $D_{4\mathrm{h}}$ symmetry group.

The full $H_{\mathrm{SF}}$ was studied here with the same Monte Carlo (MC) procedure employed in [79], supplemented with the recently developed "Parallel Traveling Cluster Approximation (PTCA)" [87], described in the next section. The values for the couplings $J_{\mathrm{H}} = 0.1$ eV, $J_{\mathrm{NN}} = J_{\mathrm{NNN}} = 0$, and $\tilde{g}_{12} = \frac{2g_{12}}{\sqrt{kW}} = 0.24$ were chosen because they provide $T_N = T_S = 70$ K for $\lambda_{12} = 0$ [43], which is the transition temperature experimentally observed in FeTe. The coupling strength $\tilde{g}_{12}$ is the dimensionless version of the spin-lattice coupling, employing $W = 3$ eV as the bandwidth of the tight-binding term and $k$ as the constant that appears in $H_{\mathrm{Stiff}}$ [79]. Since these couplings were discussed extensively before, in the present effort we will instead focus on a careful description of the new dimensionless monoclinic orbital-lattice coupling $\tilde{\lambda}_{12} = \frac{2\lambda_{12}}{\sqrt{kW}}$ and its effects.

During the simulation the Te atoms are allowed to move locally away from their equilibrium positions within the $x$-$y$ plane. The Fe atoms can move globally via a monoclinic distortion $\mathcal{M}_{\mathrm{ono}}$ where the angle between two orthogonal Fe-Fe bonds is allowed to change globally to $90^o + \theta$ with the four angles in the iron plaquette adding to $360^o$, so that the next angle in the plaquette becomes $90^o - \theta$, with $\theta$ as a small angle (see Fig. 5.1 (d)). In addition, the localized spins $\mathbf{S_i}$ and atomic displacements $(\delta_{\mathbf{i},\nu}^x, \delta_{\mathbf{i},\nu}^y)$ that determine the value of the local $\mathcal{M}_{\mathrm{ono}}$ lattice distortion $\epsilon_{12}(\mathbf{i})$ [43] (see Fig. 5.1 (c)) are evaluated via a standard Monte Carlo procedure.

## 5.3    Methods: the Parallel Traveling Cluster Approximation

To access the lattice sizes needed to study the existence of a monoclinic nematic phase we implemented the Parallel Traveling Cluster Approximation (PTCA) [87] which is a parallelization improvement over the traveling cluster approximation (TCA) previously introduced [86]. PTCA allows parallelization in order to use multiple CPU cores and by this procedure we can reach lattices as large as $32 \times 32$. To perform a Monte Carlo update

of one of the local variables – either the localized spin $\mathbf{S_i}$ at the iron site $\mathbf{i}$ or the local distortion of the Fe-Te bonds joining the Fe atom at site $\mathbf{i}$ with its four Te neighbors – an $8 \times 8$ traveling cluster is constructed around site $\mathbf{i}$ and the Hamiltonian is diagonalized only inside that cluster to decide whether the update is accepted. The algorithm is parallelized by dividing the lattice into four quadrants with $16 \times 16$ sites, one per different CPU core. Then, each CPU generates traveling $8 \times 8$ clusters around the sites belonging to its quadrant, see Fig. 5.2 for an illustration, and these clusters are then simultaneously diagonalized.
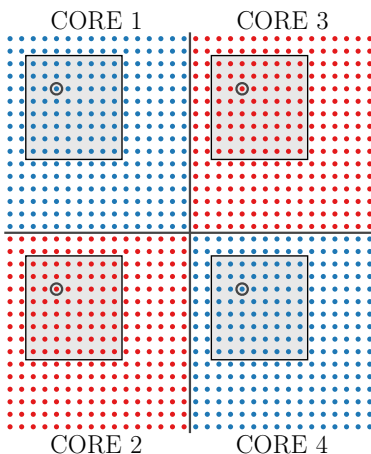


**Figure 5.2:** Diagram of the PTCA set-up used to sample the local spin and lattice variables. The lattice is divided into four quadrants and each of four processors generates traveling clusters (indicated with $8 \times 8$ squares) and proposes updates for the sites (indicated by small open circles) inside one quadrant.

To update the global monoclinic lattice distortion given by the angles in the rhombus formed by the four irons shown in Fig. 5.1 (d) an extra new modification in the PTCA was introduced. The $32 \times 32$ sites lattice was divided into 16 clusters with $8 \times 8$ sites each as shown in Fig. 5.3. Each of four CPU cores was devoted to diagonalize four of the clusters as indicated in the figure. The same update is proposed in all the clusters which are simultaneously diagonalized. Then, all the eigenvalues are collected in one of the cores in order to calculate the probability of the Monte Carlo update and decide whether the update is accepted or rejected.

For thermalization typically 5,000 Monte Carlo steps were used, while 10,000 to 25,000 steps were performed in between measurements for each set of parameters and temperatures. The spin-spin correlation functions in real space were measured and the magnetic structure
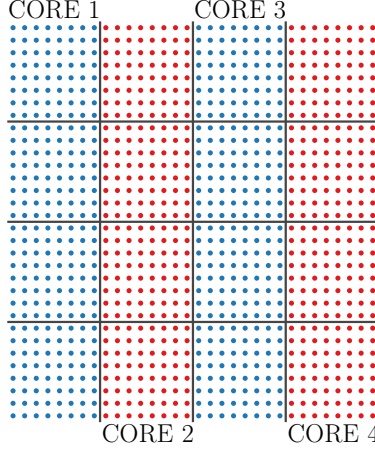
**Figure 5.3:** Diagram of the PTCA set-up used to sample the global lattice distortion variables. The lattice is divided into sixteen clusters. Each of the four processors diagonalizes four of the clusters.

factor $S(k_x, k_y)$ was calculated via their Fourier transform. Notice that in the bicollinear state the magnetic structure factor diverges for $(k_x, k_y) = (\pi/2, \pi/2)$ or $(\pi/2, -\pi/2)$. The Néel temperature $T_N$ is obtained from the magnetic susceptibility for a given wavevector which is given by

$$\chi_{S(k_x,k_y)} = N\beta\langle S(k_x, k_y) - \langle S(k_x, k_y)\rangle\rangle^2, \tag{5.8}$$

where $\beta = 1/k_B T$ and $N$ is the number of lattice sites. We also calculated the numerical derivative of $S(\pi/2, \pi/2)$ with respect to temperature to double-check the value of $T_N$. The monoclinic structural transition temperature, $T_S$, was obtained by calculating the structural susceptibility given by

$$\chi_{\delta_M} = N\beta\langle \delta_M - \langle \delta_M\rangle\rangle^2, \tag{5.9}$$

where $\delta_M \approx \theta/2$ and $\theta$ is the deviation from $90^o$ of the angle of the lattice plaquette as shown in Fig. 5.1 (d) [43]. $T_S$ was also obtained from the numerical derivative of $\delta_M$ as a function of temperature and from monitoring the behavior of the spin-nematic and orbital-nematic order parameters, $\Psi_{NNN}(\mathbf{i})$ and $\Phi_{B_{2g}}(\mathbf{i})$ respectively, introduced in the previous section and their associated susceptibilities.

## 5.4  Results

In previous work [43] we found that the magneto-structural transition experimentally observed in FeTe with $T_S = T_N = 70$ K, was reproduced by setting $J_{\mathrm{H}} = 0.1$ eV, $J_{\mathrm{NN}} = J_{\mathrm{NNN}} = 0$, and $\tilde{g}_{12} = 0.24$. In the present study we keep fixed the values of these parameters while we vary the orbital-lattice coupling $\tilde{\lambda}_{12}$ to investigate whether a nematic phase can be stabilized and obtain the phase diagram varying the orbital-lattice coupling and temperature.

### 5.4.1  Special case $\tilde{\lambda}_{12} = 1$

In agreement with the behavior reported before for the spin-fermion model in the case of the pnictides with $(\pi, 0)$ spin order [79], in the bicollinear case studied here it was indeed also observed that the novel bicollinear nematic region becomes stable by increasing the value of the orbital-lattice coupling. Another similarity with the case of the collinear state [79] is that the addition of the orbital-lattice coupling $\tilde{\lambda}_{12}$ turns the first order magnetic transition into a second order one. The temperature width of nematicity remains narrow, as in many previous investigations, and robust values of $\tilde{\lambda}_{12}$ are required. Nevertheless, this is sufficient to demonstrate the matter-of-principle existence of the bicollinear-nematic state discussed in this publication. For clarity, first let us address in detail the largest value of the coupling that we studied which was $\tilde{\lambda}_{12} = 1$.

In Fig. 5.4 the magnetic susceptibility $\chi_{S(\pi/2,\pi/2)}$ versus temperature is shown. A clear maximum at $T_N = 165$ K indicates the magnetic transition to the bicollinear state with long-range order. The monoclinic lattice susceptibility is also shown. Interestingly, this quantity has a sharp peak at a clearly larger temperature $T_S = 193$ K, where the structural transition from tetragonal to monoclinic takes place, indicating that a bicollinear-nematic state does indeed occur.

In Fig. 5.5 the magnetic structure factor at wavevector $(\pi/2, \pi/2)$ is displayed. The $T_N$ from the susceptibility, shown with a dashed line, should occur when the rate of increase of the order parameter is maximized. This has been verified by performing a spline fit of the $S(\pi/2, \pi/2)$ points obtained from the Monte Carlo simulation and taking the numerical
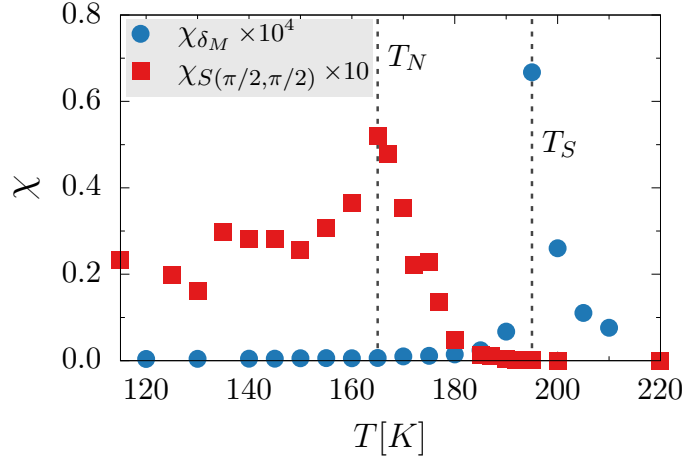
**Figure 5.4:** Magnetic susceptibility $\chi_S$ (squares) and monoclinic lattice susceptibility $\chi_{\delta_M}$ (circles) evaluated using the PTCA algorithm at $\tilde{\lambda}_{12} = 1$ employing a $32 \times 32$ sites cluster. In this plot, and other plots of susceptibilities shown below, the fluctuations between subsequent temperatures are more indicative of the error bars than the intrinsic errors bars of individual points, which for this reason are not shown.

derivative. The monoclinic lattice order parameter $\delta_M$ is also presented in Fig. 5.5. The structural transition temperature is displayed with a dashed line as well. We also verified that the maximum in the lattice susceptibility from Fig. 5.4 coincides with the maximum rate of change in the lattice order parameter via a spline fit of the Monte Carlo data.
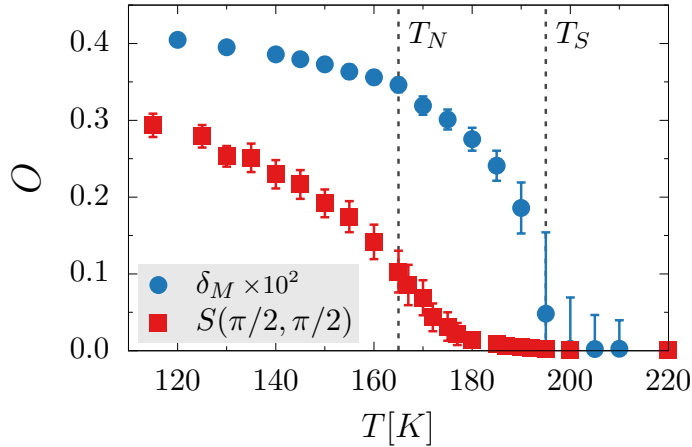


**Figure 5.5:** Magnetic spin structure factor $S(\pi/2, \pi/2)$ (squares) and monoclinic lattice order parameter $\delta_M$ (circles) evaluated using the PTCA algorithm for $\tilde{\lambda}_{12} = 1$ on a $32 \times 32$ sites cluster.

In between the two transition temperatures $T_N$ and $T_S$, a nematic phase is stabilized. In this phase both short-range orbital and spin nematic order develop as it can be seen in

Fig. 5.6, where in panel (a) the susceptibilities associated with various order parameters are presented. It can be observed that the orbital-nematic and spin-nematic susceptibilities have maxima at $T_S$ as does the structural susceptibility. This confirms the presence of a monoclinic nematic phase characterized by orbital-nematic and spin-nematic orders. These properties are also reflected in the behavior of the respective order parameters shown in panel (b) of the figure.
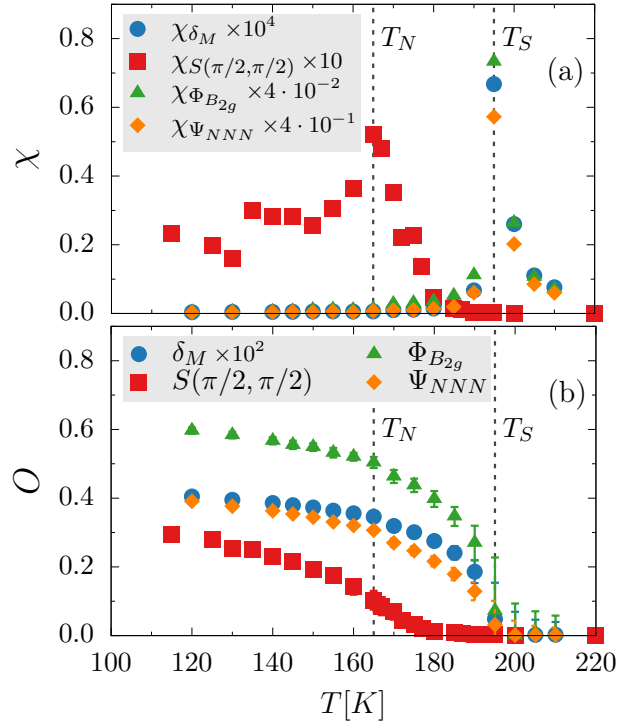


**Figure 5.6:** (a) Magnetic susceptibility $\chi_{S(\pi/2,\pi/2)}$ (red squares) with a maximum at $T_N = 165$ K (dashed line), and the monoclinic lattice susceptibility $\chi_{\delta_M}$ (blue circles), spin-nematic susceptibility $\chi_\Psi$ (orange diamonds), and orbital-nematic susceptibility $\chi_\Phi$ (green triangles) all with a maximum at $T_S = 193$ K. The susceptibilities were calculated at $\tilde{\lambda}_{12} = 1$ using $32 \times 32$ lattices. (b) Monte Carlo measured order parameters associated to (a). Shown are the magnetic structure factor $S(\pi/2, \pi/2)$ (red squares), monoclinic lattice distortion $\delta_M$ (blue circles), spin-nematic order parameter $\Psi_{NNN}$ (orange diamonds), and orbital-nematic order parameter $\Phi_{B_{2g}}$ (green triangles). The transition temperatures were obtained from the susceptibilities in (a) and via numerical derivatives in (b). Both procedures give the same result.

Performing spline fits of the order parameters and taking numerical derivatives, the critical temperatures obtained from the susceptibilities were reproduced. It is important to notice that the lattice distortions $\delta_M \sim 10^{-3}$ are quantitatively similar to those reported

in FeTe experiments while, as shown in Fig. 5.6 (b), the orbital and spin nematic order parameters develop values an order of magnitude larger. Thus, the strength of the orbital-lattice coupling used still leads to small lattice distortions but appears to generate robust magnetic and orbital short-range order inducing substantial anisotropic effects in these observables.

## 5.4.2 Special case $\tilde{\lambda}_{12} = 0.85$

As the value of the orbital-lattice coupling is reduced the separation between the magnetic and the structural transitions decreases. In panel (a) of Fig. 5.7 the magnetic and structural susceptibilities at $\tilde{\lambda}_{12} = 0.85$ obtained from Monte Carlo simulations are presented. In this case $T_N = 145$ K while $T_S = 147$ K. The orbital- and spin-nematic order parameters also have a maximum susceptibility at $T_S$ (not shown for simplicity). The magnetic and structural order parameters are shown in panel (b) of Fig. 5.7 and their qualitative behavior is in agreement with panel (a). The indicated transition temperatures have been obtained from numerical fits of the order parameters and their derivatives as described in the previous subsection. This case $\tilde{\lambda}_{12} = 0.85$ is close to the limit of our numerical accuracy. In principle, it is possible that simulations using larger systems and with far more statistics may unveil a very narrow bicollinear nematic state even for small values of $\tilde{\lambda}_{12}$. However, for our qualitative purposes simply showing the stability of the new proposed phase in any range of $\tilde{\lambda}_{12}$ is sufficient.

## 5.4.3 Phase Diagram

The phase diagram obtained as a function of the orbital-lattice coupling $\tilde{\lambda}_{12}$ and temperature is presented in Fig. 5.8. It can be seen that the region with $B_{2g}$ nematicity can be stabilized at robust values of the orbital-lattice coupling. While a very narrow nematic phase may exist at smaller values of this coupling, numerically we have been able to resolve the separation between the two critical temperatures only for $\tilde{\lambda}_{12} \geq 0.75$. As described in the previous sections, the separation between $T_N$ and $T_S$ monotonically increases with $\tilde{\lambda}_{12}$.
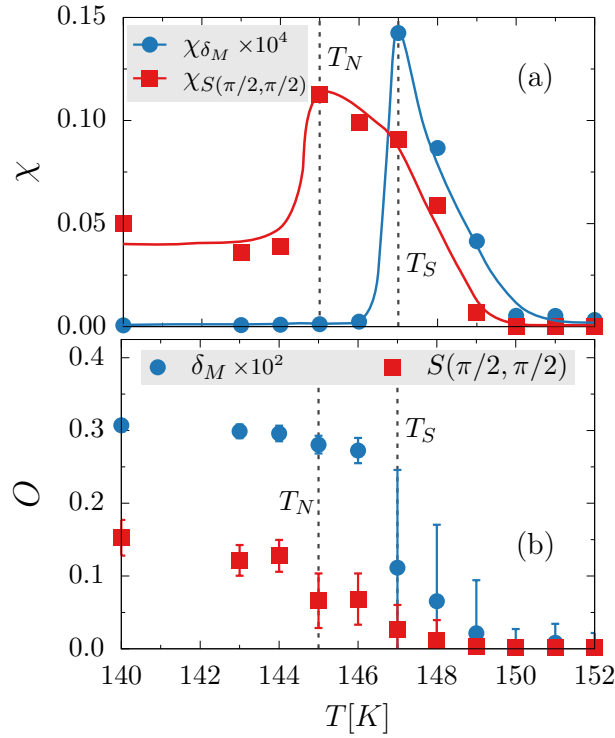
**Figure 5.7:** (a) Susceptibilities associated with the magnetic spin structure factor $S(\pi/2, \pi/2)$ (squares) and with the monoclinic lattice distortion (circles) using $\tilde{\lambda}_{12} = 0.85$ and a $32 \times 32$ cluster. Solid lines are guides to the eye. (b) Spin structure factor $S(\pi/2, \pi/2)$ (squares) and monoclinic lattice order parameter $\delta_M$ (circles) for the same $\tilde{\lambda}_{12}$ and cluster size as in (a).
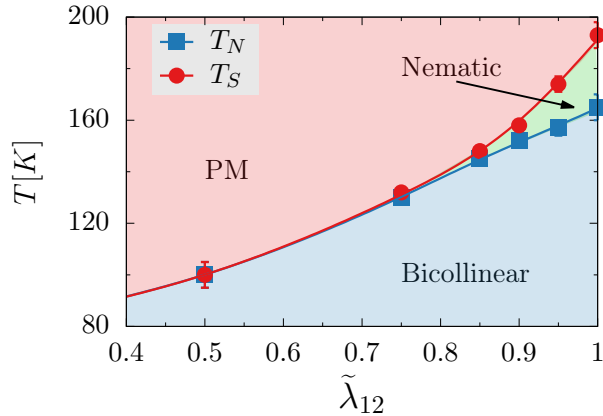


**Figure 5.8:** Phase diagram varying temperature and $\tilde{\lambda}_{12}$, for $\tilde{g}_{12} = 0.24$, $J_{\mathrm{H}} = 0.1$ eV, and $J_{\mathrm{NN}} = J_{\mathrm{NNN}} = 0.0$. Note the narrow temperature width of stability of the bicollinear-nematic state, similarly as it occurs for the more standard $(\pi, 0) - (0, \pi)$ nematic state [79]. For values of $\tilde{\lambda}_{12}$ smaller than 0.75, our numerical accuracy does not allow us to distinguish between $T_N$ and $T_S$.

## 5.5 Discussion and Possible Physical Realizations

Our results have illustrated the possible existence of a nematic phase involving bicollinear short-range order, using as explicit example a computational study of the spin-fermion model incorporating the lattice distortions corresponding to the iron telluride family. Previously the results in Ch. 4 showed that the addition to the electronic spin-fermion model for pnictides of a coupling between a spin-nematic order parameter with $B_{2g}$ symmetry and the monoclinic distortions of the iron lattice does induce the monoclinic and spin bicollinear state experimentally observed in FeTe. That result was remarkable because the spin-fermion model contains a tight-binding term that favors the $(\pi, 0)$ and $(0, \pi)$ collinear states that arise from the nesting of the Fermi surface in weak coupling. However, the $\tilde{g}_{12}$ spin-lattice interaction, when sufficiently strong, can overcome these tendencies and stabilize the monoclinic bicollinear state.

Here, we have included an additional orbital-lattice term with coupling strength $\tilde{\lambda}_{12}$, involving the monoclinic lattice strain coupled to an orbital order parameter with $B_{2g}$ symmetry. By this procedure we have shown that a novel nematic phase characterized by the breakdown of the lattice rotational symmetry between the two possible diagonal directions of the spin bicollinear state can be induced. In this new nematic phase, short-range spin- and orbital-nematic order develop accompanied by a lattice monoclinic distortion.

The model Hamiltonian studied here only allows us to show explicitly, as a matter of principle, that indeed the bicollinear-nematic state described above does occur in computational studies once all of the many degrees of freedom and couplings are properly incorporated. But it is difficult to predict on what specific material this subtle state will be realized in practice, thus we can only discuss some scenarios qualitatively. The possible splitting of $T_N$ and $T_S$ by electron doping was raised in Ref. [75]. However, spin-fermion model studies including doping but not quenched disorder (i.e. in the "clean" limit from Sec. 3.4) did not detect such a split, at least in the doping range studied (See Fig. 3.2). Another generic qualitative observation is that in the pnictides nematicity is observed for the 1111 compounds even in the undoped limit [30]. Thus, to find the $B_{2g}$ nematic phase discussed here it may be necessary to synthesize materials with intercalated FeTe planes.

However, in our opinion the most likely scenario to stabilize the proposed bicollinear-nematic regime in variations of the FeTe compound is by the chemical replacement of iron by other transition metal elements, thus simultaneously modifying the electronic density as well as the amount of quenched disorder. In pnictides, replacing Fe by Co, Ni, or Cu indeed leads to a wide nematic region. The previously mentioned computational investigations using the spin-fermion model with doping and disorder(See Ch. 3) clearly showed that indeed by this procedure a $(\pi, 0)$ nematic temperature range can be induced even in cases where $T_N$ and $T_S$ coincide in a first-order transition for the undoped parent compound, as in the 122 family. Disorder plays a more important role than doping in this split [98], as observed experimentally as well [49]. To our knowledge the experimental investigations of (Fe,$X$)Te, with $X$ another transition metal element, are very limited. We are aware of three main lines of investigations and conclusions:

*(i)* Copper doping of FeTe was studied in [172, 173] for two Cu concentrations using single crystals. For the case $Fe_{1.06}Cu_{0.04}Te$ the presence of strain was detected at 41 K upon cooling [172]. At lower temperatures approximately 36 K nearly-commensurate long-range bicollinear magnetic order occurs. The presence of two transitions seems in agreement with our prediction of bicollinear nematicity. However, in [172] it was argued that between 36 K and 41 K the lattice distortion could be orthorhombic as in pnictides. The possible competition with orthorhombic tendencies was theoretically addressed and reported in Ch. 4 with further details added in Appendix G. This competition adds an extra complication to the detection of the here predicted bicollinear-nematic state. For the case $FeCu_{0.1}Te$ only cluster glass behavior was found below 22 K, presumably due to disorder [172]. Note that this glassy state could be nematic.

*(ii)* The case of Ni doping was reported for the compounds $Fe_{1.1-x}Ni_xTe$ with $x = 0, 0.02, 0.04, 0.08$, and 0.12 [174]. Magnetization studies show that $T_N$ decreases with increasing $x$ up to 0.04, while for $x = 0.08, 0.12$ a possible spin glass transition was reported. In fact, neutron diffraction at $x = 0.12$ found neither structural nor magnetic transitions at low temperatures. Since this study focused on long-range magnetic order, the presence of bicollinear nematicity is still possible.

*(iii)* Cobalt doping has also been recently studied via single crystals of $Fe_{1+y-x}Co_xTe$ with $x = 0, 0.01, 0.04, 0.07, 0.09,$ and $0.11$ [175]. In the range up to $x = 0.07$ the antiferromagnetic transition systematically decreases. For $x = 0.09$ and larger the long-range order transition disappears.

As a partial summary, the available experimental literature on $(Fe,X)Te$ does not conclusively show neither the presence nor absence of bicollinear-nematicity, and more work is needed to clarify this matter now in the light of our present study. For example, in the context of pnictides the pioneering studies of $Ba(Fe_{1-x}Co_x)_2As_2$ [71] reported the resistivities vs. temperature along the $a$ and $b$ axes, highlighting their different behavior and substantial differences particularly below $x = 0.07$. Similar careful studies in the Te context must be performed but focusing on the temperature evolution of the resistivities along and perpendicular to the main spin diagonals in the bicollinear state, as already performed for FeTe [147, 148]. In addition, recent inelastic neutron scattering studies of nematicity in $BaFe_{1.935}Ni_{0.065}As_2$ [176] focused on the temperature dependence of the intensity of the peaks at $(\pi, 0)$ and $(0, \pi)$, reporting their split at $T_S$ with cooling, followed by a collapse to zero of the $(0, \pi)$ intensity at $T_N$. Similar studies for $X$-doped FeTe ($X$=Cu,Ni,Co) should be carried for the temperature dependence of the neutron intensities corresponding to the $(\pi/2, \pi/2)$ and $(\pi/2, -\pi/2)$ wavevectors.

We also would like to point out that our work confirms that magnetoelastic effects tend to stabilize the bicollinear state while in the absence of this kind of coupling $Q$ plaquette or orthogonal double stripe order could be stabilized, which may be the case in FeTe with excess iron [142, 177]. In addition, in a recent publication [178] a double-stage nematic bond-ordering above the bicollinear state was proposed, but this effect would be difficult to study numerically due to the narrow range of the nematic phase.

## 5.6 Conclusions

In this Chapter, based on simple symmetry observations and a concrete model Hamiltonian numerical simulation, we have argued that the exotic bicollinear state known to be stable in FeTe admits a possible nematic state above the antiferromagnetic critical temperature. In

other words, as discussed in the previous section, via chemical substitution it is conceivable that a split of the first-order transition of FeTe could be generated. Upon cooling, this would induce first a $T_S$, where the $B_{2g}$ monoclinic distortion is stabilized and short-range spin and orbital order develops breaking the lattice rotational invariance, and second a $T_N$ at a lower temperature, where long-range bicollinear order is fully stabilized. Experimentally finding this new exotic state not only would confirm the theoretical prediction outlined here, but it would allow us to investigate to what extend nematic fluctuations are needed to induce superconductivity.

# Chapter 6

# Summary

This manuscript presented numerical results that reproduce several important properties on the iron based superconductors. This was accomplished by applying Monte Carlo techniques to spin fermion models that were developed to include the relevant degrees of freedom. In Ch. 2, an experimentally observed diverging nematic susceptibility was reproduced numerically and explained analytically via a Ginzburg-Landau formalism. For the 122 compounds, electron doping and disorder where decoupled and studied separately in Ch. 3. There, it was found that disorder is the driving force that suppresses the magnetic order more quickly than the orthorhombic distortion leading to the nematic phase. In Ch. 4 the bicollinear magnetic order together with the monoclinic structural distortion observed in FeTe was stabilized through the addition of a $B_{2g}$ spin-lattice coupling. As an extension of these results, a $B_{2g}$ nematic phase was predicted and established numerically via the addition of a $B_{2g}$ orbital-lattice coupling as demonstrated in Ch. 5.

# Bibliography

[1] Ouboter, R. (1997). Heike Kamerlingh Onnes discovery of superconductivity. *Scientific American*, 276(3):98–103. 1

[2] Bardeen, J., Cooper, L. N., and Schrieffer, J. R. (1957). Theory of superconductivity. *Phys. Rev.*, 108:1175–1204. 1

[3] Steglich, F., Aarts, J., Bredl, C. D., Lieke, W., Meschede, D., Franz, W., and Schäfer, H. (1979). Superconductivity in the presence of strong Pauli paramagnetism: $Cecu_2si_2$. *Phys. Rev. Lett.*, 43:1892–1896. 1

[4] Bednorz, J. G. and Müller, K. A. (1986). Possible high $T_c$ superconductivity in the BaLaCuO system. *Zeitschrift für Physik B Condensed Matter*, 64(2):189–193. 1

[5] Tokura, Y., Takagi, H., and Uchida, S. (1989). A superconducting copper oxide compound with electrons as the charge carriers. *Nature*, 337(6205):345–347. 2

[6] Barišić, N., Chan, M. K., Li, Y., Yu, G., Zhao, X., Dressel, M., Smontara, A., and Greven, M. (2013). Universal sheet resistance and revised phase diagram of the cuprate high-temperature superconductors. *Proceedings of the National Academy of Sciences*, 110(30):12235–12240. ix, 3

[7] Lumsden, M. and Christianson, A. (2010). Magnetism in Fe-based superconductors. *Journal of Physics: Condensed Matter*, 22(20):203–203. ix, 3

[8] Schilling, A., Cantoni, M., Guo, J. D., and Ott, H. R. (1993). Superconductivity above 130 K in the Hg-Ba-Ca-Cu-O system. *Nature*, 363(6424):56–58. 2

[9] Kamihara, Y., Hiramatsu, H., Hirano, M., Kawamura, R., Yanagi, H., Kamiya, T., and Hosono, H. (2006). Iron-based layered superconductor: LaOFeP. *Journal of the American Chemical Society*, 128(31):10012–10013. 2, 8

[10] Kasahara, S., Shi, H. J., Hashimoto, K., Tonegawa, S., Mizukami, Y., Shibauchi, T., Sugimoto, K., Fukuda, T., Terashima, T., Nevidomskyy, A. H., and Matsuda, Y. (2012). Electronic nematicity above the structural and superconducting transition in $BaFe_2(As_{1-x}P_x)_2$. *Nature*, 486(7403):382–385. ix, 4, 26, 69, 70, 120

[11] Blomberg, E. C., Tanatar, M. A., Fernandes, R. M., Mazin, I. I., Shen, B., Wen, H.-H., Johannes, M. D., Schmalian, J., and Prozorov, R. (2013). Sign-reversal of the in-plane resistivity anisotropy in hole-doped iron pnictides. *Nature Communications*, 4(1914). ix, 4

[12] Dai, P., Hu, J., and Dagotto, E. (2012). Magnetism and its microscopic origin in iron-based high-temperature superconductors. *Nature Physics*, 8(10):709–718. x, 5, 7, 13, 17, 35, 58, 69

[13] Brouet, V., Jensen, M. F., Lin, P.-H., Taleb-Ibrahimi, A., Le Fèvre, P., Bertran, F., Lin, C.-H., Ku, W., Forget, A., and Colson, D. (2012). Impact of the two Fe unit cell on the electronic structure measured by ARPES in iron pnictides. *Phys. Rev. B*, 86:075123. 4

[14] Tokura, Y. and Nagaosa, N. (2000). Orbital physics in transition-metal oxides. *Science*, 288(5465):462–468. x, 5

[15] Perry, J. K., Tahir-Kheli, J., and Goddard, W. A. (2001). Antiferromagnetic band structure of $La_2CuO_4$: Becke-3–Lee-Yang-Parr calculations. *Phys. Rev. B*, 63:144510. x, 6

[16] Vildosola, V., Pourovskii, L., Arita, R., Biermann, S., and Georges, A. (2008). Bandwidth and Fermi surface of iron oxypnictides: Covalency and sensitivity to structural changes. *Phys. Rev. B*, 78:064518. x, 6, 13

[17] Hashimoto, M., Vishik, I. M., He, R.-H., Devereaux, T. P., and Shen, Z.-X. (2014). Energy gaps in high-transition-temperature cuprate superconductors. *Nature Physics*, 10:483–495. x, 7

[18] Graser, S., Kemper, A. F., Maier, T. A., Cheng, H.-P., Hirschfeld, P. J., and Scalapino, D. J. (2010). Spin fluctuations and superconductivity in a three-dimensional tight-binding model for $BaFe_2As_2$. *Phys. Rev. B*, 81:214503. x, 7, 13, 14

[19] Buhler, C., Yunoki, S., and Moreo, A. (2000). Magnetic domains and stripes in a spin-fermion model for cuprates. *Phys. Rev. Lett.*, 84:2690–2693. 6, 15

[20] Feiner, L. F., Jefferson, J. H., and Raimondi, R. (1996). Effective single-band models for the high-$T_c$ cuprates. I. coulomb interactions. *Phys. Rev. B*, 53:8751–8773. 6

[21] Boeri, L., Dolgov, O. V., and Golubov, A. A. (2008). Is LaFeAsO$_{1-x}$F$_x$ an electron-phonon superconductor? *Phys. Rev. Lett.*, 101:026403. 6, 13, 26

[22] Yi, M., Lu, D., Chu, J.-H., Analytis, J. G., Sorini, A. P., Kemper, A. F., Moritz, B., Mo, S.-K., Moore, R. G., Hashimoto, M., Lee, W.-S., Hussain, Z., Devereaux, T. P., Fisher, I. R., and Shen, Z.-X. (2011). Symmetry-breaking orbital anisotropy observed for detwinned Ba(Fe$_{1-x}$Co$_x$)$_2$As$_2$ above the spin density wave transition. *Proceedings of the National Academy of Sciences*, 108(17):6878–6883. 6, 19

[23] Hirschfeld, P., Korshunov, M., and Mazin, I. (2011). Gap symmetry and structure of Fe-based superconductors. *Reports on Progress in Physics*, 74(12):124508. x, 7, 8, 69

[24] Hu, J. and Ding, H. (2012). Local antiferromagnetic exchange and collaborative Fermi surface as key ingredients of high temperature superconductors. *Scientific Reports*, 2(381). x, 7

[25] Tsuei, C. and Kirtley, J. (1997). Tricrystal tunneling evidence for d-wave pairing symmetry in cuprate superconductors. *Journal of Alloys and Compounds*, 250(1):615–618. 8

[26] Kontani, H. and Yamakawa, Y. (2014). Linear response theory for shear modulus $C_{66}$ and Raman quadrupole susceptibility: Evidence for nematic orbital fluctuations in Fe-based superconductors. *Phys. Rev. Lett.*, 113:047001. 8, 9

[27] Christianson, A. D., Goremychkin, E. A., Osborn, R., Rosenkranz, S., Lumsden, M. D., Malliakas, C. D., Todorov, I. S., Claus, H., Chung, D. Y., Kanatzidis, M. G., Bewley, R. I., and Guidi, T. (2008). Unconventional superconductivity in Ba$_0$.6K$_0$.4Fe$_2$As$_2$ from inelastic neutron scattering. *Nature*, 456:930–932. 8

[28] Ding, H., Richard, P., Nakayama, K., Sugawara, K., Arakane, T., Sekiba, Y., Takayama, A., Souma, S., Sato, T., Takahashi, T., Wang, Z., Dai, X., Fang, Z., Chen, G. F., Luo, J. L.,

and Wang, N. L. (2008). Observation of Fermi surface dependent nodeless superconducting gaps in $Ba_{0.6}K_{0.4}Fe_2As_2$. *Europhysics Letters*, 83(4):47001. 8

[29] Terashima, T., Kimata, M., Kurita, N., Satsukawa, H., Harada, A., Hazama, K., Imai, M., Sato, A., Kihou, K., Lee, C.-H., Kito, H., Eisaki, H., Iyo, A., Saito, T., Fukazawa, H., Kohori, Y., Harima, H., and Uji, S. (2010). Fermi surface and mass enhancement in $KFe_2As_2$ from de Haasvan Alphen effect measurements. *Journal of the Physical Society of Japan*, 79(5):053702. 8

[30] de la Cruz, C., Huang, Q., Lynn, J. W., Li, J., II, W. R., Zarestky, J. L., Mook, H. A., Chen, G. F., Luo, J. L., Wang, N. L., and Dai, P. (2008). Magnetic order close to superconductivity in the iron-based layered $LaO_{1-x}F_xFeAs$ systems. *Nature*, 453:899–902. 8, 35, 69, 70, 84

[31] Fang, C., Yao, H., Tsai, W.-F., Hu, J., and Kivelson, S. A. (2008). Theory of electron nematic order in LaFeAsO. *Phys. Rev. B*, 77:224509. 8, 9, 17, 33

[32] Tanatar, M. A., Blomberg, E. C., Kreyssig, A., Kim, M. G., Ni, N., Thaler, A., Bud'ko, S. L., Canfield, P. C., Goldman, A. I., Mazin, I. I., and Prozorov, R. (2010). Uniaxial-strain mechanical detwinning of $CaFe_2As_2$ and $BaFe_2As_2$ crystals: Optical and transport study. *Phys. Rev. B*, 81:184508. 8

[33] Kontani, H., Inoue, Y., Saito, T., Yamakawa, Y., and Onari, S. (2012). Orbital fluctuation theory in iron-based superconductors: s++-wave superconductivity, structure transition, and impurity-induced nematic order. *Solid State Communications*, 152(8):718 –727. 8, 17, 20, 33, 34, 35

[34] Kontani, H., Saito, T., and Onari, S. (2011). Origin of orthorhombic transition, magnetic transition, and shear-modulus softening in iron pnictide superconductors: Analysis based on the orbital fluctuations theory. *Phys. Rev. B*, 84:024528. 8, 9, 17, 20, 33, 34, 35

[35] Fernandes, R. M. and Schmalian, J. (2012). Manifestations of nematic degrees of freedom in the magnetic, elastic, and superconducting properties of the iron pnictides. *Superconductor Science and Technology*, 25(8):084005. xi, 9, 10, 62, 69, 120

[36] Fernandes, R. M., Chubukov, A. V., and Schmalian, J. (2014). What drives nematic order in iron-based superconductors? *Nature Physics*, 10:97–104. 9, 17, 20, 33, 37, 69

[37] Krüger, F., Kumar, S., Zaanen, J., and van den Brink, J. (2009). Spin-orbital frustrations and anomalous metallic state in iron-pnictide superconductors. *Phys. Rev. B*, 79:054504. 9

[38] Lv, W., Wu, J., and Phillips, P. (2009). Orbital ordering induces structural phase transition and the resistivity anomaly in iron pnictides. *Phys. Rev. B*, 80:224506. 9, 17

[39] Hsu, F.-C., Luo, J.-Y., Yeh, K.-W., Chen, T.-K., Huang, T.-W., Wu, P. M., Lee, Y.-C., Huang, Y.-L., Chu, Y.-Y., Yan, D.-C., and Wu, M.-K. (2008). Superconductivity in the PbO-type structure -FeSe. *Proceedings of the National Academy of Sciences*, 105(38):14262–14264. 10

[40] Mizuguchi, Y. and Takano, Y. (2010). Review of Fe chalcogenides as the simplest Fe-based superconductor. *Journal of the Physical Society of Japan*, 79(10):102001. 11

[41] Li, S., de la Cruz, C., Huang, Q., Chen, Y., Lynn, J. W., Hu, J., Huang, Y.-L., Hsu, F.-C., Yeh, K.-W., Wu, M.-K., and Dai, P. (2009). First-order magnetic and structural phase transitions in $Fe_{1+y}Se_xTe_{1-x}$. *Phys. Rev. B*, 79:054503. xxi, 11, 58, 59, 65, 66, 70, 132, 140, 145

[42] Liu, T. J., Hu, J., Qian, B., Fobes, D., Mao, Z. Q., Bao, W., Reehuis, M., Kimber, S. A. J., Proke, K., Matas, S., Argyriou, D. N., Hiess, A., Rotaru, A., Pham, H., Spinu, L., Qiu, Y., Thampy, V., Savici, A. T., Rodriguez, J. A., and Broholm, C. (2010). From $(\pi,0)$ magnetic order to superconductivity with $(\pi,\pi)$ magnetic resonance in $Fe_{1.02}Te_{1x}Se_x$. *Nature Materials*, 9:718–720. xi, 11, 12

[43] Bishop, C. B., Moreo, A., and Dagotto, E. (2016). Bicollinear antiferromagnetic order, monoclinic distortion, and reversed resistivity anisotropy in FeTe as a result of spin-lattice coupling. *Phys. Rev. Lett.*, 117:117201. 11, 58, 70, 74, 76, 78, 79, 106

[44] Dagotto, E. (1994). Correlated electrons in high-temperature superconductors. *Rev. Mod. Phys.*, 66:763–840. 13

[45] Dong, J., Zhang, H. J.,Xu, G., Li, Z., Li, G., Hu, W. Z., Chen, G. F., Dai, X., Luo, J. L., Fang, Z. and Wang, N. L.(2010). Competing orders and spin-density-wave instability in $La(O_{1-x}F_x)FeAs$. *Europhysics Letters*, 83(2):27006. 13

[46] Si, Q. and Abrahams, E. (2008). Strong correlations and magnetic frustration in the high $T_c$ iron pnictides. *Phys. Rev. Lett.*, 101:076401. 13, 33

[47] Applegate, R., Oitmaa, J., and Singh, R. R. P. (2010). Spin waves in $J_{1a}-J_{1b}-J_2$ orthorhombic square-lattice Heisenberg models: Application to iron pnictide materials. *Phys. Rev. B*, 81:024505. 13

[48] Seo, K., Bernevig, B. A., and Hu, J. (2008). Pairing symmetry in a two-orbital exchange coupling model of oxypnictides. *Phys. Rev. Lett.*, 101:206404. 13

[49] Ni, N., Thaler, A., Yan, J. Q., Kracher, A., Colombier, E., Bud'ko, S. L., Canfield, P. C., and Hannahs, S. T. (2010). Temperature versus doping phase diagrams for $Ba(Fe_{1-x}TM_x)_2As_2(TM = Ni, Cu, Cu/Co)$ single crystals. *Phys. Rev. B*, 82:024519. xv, 13, 33, 34, 35, 41, 43, 45, 47, 85

[50] Khasanov, R., Zhou, H., Amato, A., Guguchia, Z., Morenzoni, E., Dong, X., Zhang, G., and Zhao, Z. (2016). Proximity-induced superconductivity within the insulating $(Li_{0.84}Fe_{0.16})OH$ layers in $(Li_{0.84}Fe_{0.16})OHFe_{0.98}Se$. *Phys. Rev. B*, 93:224512. 13

[51] Gretarsson, H., Lupascu, A., Kim, J., Casa, D., Gog, T., Wu, W., Julian, S. R., Xu, Z. J., Wen, J. S., Gu, G. D., Yuan, R. H., Chen, Z. G., Wang, N.-L., Khim, S., Kim, K. H., Ishikado, M., Jarrige, I., Shamoto, S., Chu, J.-H., Fisher, I. R., and Kim, Y.-J. (2011). Revealing the dual nature of magnetism in iron pnictides and iron chalcogenides using x-ray emission spectroscopy. *Phys. Rev. B*, 84:100509. 13, 35

[52] Yin, W.-G., Lee, C.-C., and Ku, W. (2010). Unified picture for magnetic correlations in iron-based superconductors. *Phys. Rev. Lett.*, 105:107004. 13, 15, 19, 35, 36, 61

[53] Johannes, M. D. and Mazin, I. I. (2009). Microscopic origin of magnetism and magnetic interactions in ferropnictides. *Phys. Rev. B*, 79:220510. 13

[54] Daghofer, M., Moreo, A., Riera, J. A., Arrigoni, E., Scalapino, D. J., and Dagotto, E. (2008). Model for the magnetic order and pairing channels in Fe pnictide superconductors. *Phys. Rev. Lett.*, 101:237004. 13

[55] Moreo, A., Daghofer, M., Riera, J. A., and Dagotto, E. (2009). Properties of a two-orbital model for oxypnictide superconductors: Magnetic order, $B_{2g}$ spin-singlet pairing channel, and its nodal structure. *Phys. Rev. B*, 79:134502. 13, 14

[56] Daghofer, M., Nicholson, A., Moreo, A., and Dagotto, E. (2010). Three orbital model for the iron-based superconductors. *Phys. Rev. B*, 81:014511. 14, 15, 19, 35, 37, 61, 73, 117, 136

[57] Lv, W., Krüger, F., and Phillips, P. (2010). Orbital ordering and unfrustrated $(\pi, 0)$ magnetism from degenerate double exchange in the iron pnictides. *Phys. Rev. B*, 82:045125. 14, 15, 19, 35, 36

[58] Raghu, S., Qi, X.-L., Liu, C.-X., Scalapino, D. J., and Zhang, S.-C. (2008). Minimal two-band model of the superconducting iron oxypnictides. *Phys. Rev. B*, 77:220503. 14

[59] Zhang, X. and Dagotto, E. (2011). Anisotropy of the optical conductivity of a pnictide superconductor from the undoped three-orbital Hubbard model. *Phys. Rev. B*, 84:132505. 15

[60] Fisher, I. R., Degiorgi, L., and Shen, Z. X. (2011). In-plane electronic anisotropy of underdoped '122' Fe-arsenide superconductors revealed by measurements of detwinned single crystals. *Reports on Progress in Physics*, 74(12):124506. 15, 17, 18

[61] Liang, S., Alvarez, G., Şen, C., Moreo, A., and Dagotto, E. (2012). Anisotropy of electrical transport in pnictide superconductors studied using Monte Carlo simulations of the spin-fermion model. *Phys. Rev. Lett.*, 109:047001. 15, 19, 20, 21, 26, 35, 36, 40, 61, 65, 66, 73, 110, 120, 121, 130, 133, 136, 137, 144

[62] Zener, C. (1951). Interaction between the *d*-shells in the transition metals. II. ferromagnetic compounds of manganese with perovskite structure. *Phys. Rev.*, 82:403–405. 15

[63] Anderson, P. W. and Hasegawa, H. (1955). Considerations on double exchange. *Phys. Rev.*, 100:675–681. 15

[64] Müller-Hartmann, E. and Dagotto, E. (1996). Electronic hamiltonian for transition-metal oxide compounds. *Phys. Rev. B*, 54:R6819–R6822. 15

[65] Yunoki, S., Hu, J., Malvezzi, A. L., Moreo, A., Furukawa, N., and Dagotto, E. (1998). Phase separation in electronic models for manganites. *Phys. Rev. Lett.*, 80:845–848. 15

[66] Dagotto, E., Yunoki, S., Malvezzi, A. L., Moreo, A., Hu, J., Capponi, S., Poilblanc, D., and Furukawa, N. (1998). Ferromagnetic kondo model for manganites: Phase diagram, charge segregation, and influence of quantum localized spins. *Phys. Rev. B*, 58:6414–6427. 15

[67] Chu, J.-H., Kuo, H.-H., Analytis, J. G., and Fisher, I. R. (2012). Divergent nematic susceptibility in an iron arsenide superconductor. *Science*, 337(6095):710–712.; Kuo, H.-H., Shapiro, M. C., Riggs, S. C., and Fisher, I. R. (2013). Measurement of the elastoresistivity coefficients of the underdoped iron arsenide Ba(Fe$_{0.975}$Co$_{0.025}$)$_2$As$_2$. *Phys. Rev. B*, 88:085113. xii, 16, 18, 23, 25, 26, 32, 33, 120, 121

[68] Liang, S., Mukherjee, A., Patel, N. D., Bishop, C. B., Dagotto, E., and Moreo, A. (2014). Diverging nematic susceptibility, physical meaning of $T^*$ scale, and pseudogap in the spin fermion model for the pnictides. *Phys. Rev. B*, 90:184507. 17, 36, 37, 38, 39, 41, 61, 62, 64, 73, 74, 97

[69] For the research project presented in this chapter and published in Ref. [68], my contributions were as follows. I was responsible for helping to alter the code and then submit the code to the compute cluster. Afterwards, I would perform analysis on the resulting data and run programs to calculate observables. Plotting many of the final results that I had submitted was also part of my contribution. Then in collaboration, we interpreted the results. The parameter space is large and consists of Temperature, $\alpha$, $g$, and $\lambda$, and I was also part of the discussion regarding which area of the parameter space to explore. I was also involved in the checking the Ginzburg-Landau analytical analysis and then I fit the equations to the numerical results. 17

[70] Johnston, D. C. (2010). The puzzle of high temperature superconductivity in layered iron pnictides and chalcogenides. *Advances in Physics*, 59(6):803–1061. 17, 58, 69

[71] Chu, J.-H., Analytis, J. G., De Greve, K., McMahon, P. L., Islam, Z., Yamamoto, Y., and Fisher, I. R. (2010). In-plane resistivity anisotropy in an underdoped iron arsenide superconductor. *Science*, 329(5993):824–826. xvi, 17, 18, 33, 60, 69, 86, 145

[72] Fradkin, E., Kivelson, S. A., Lawler, M. J., Eisenstein, J. P., and Mackenzie, A. P. (2010). Nematic Fermi fluids in condensed matter physics. *Annu. Rev. Cond. Mat. Phys.*, 1:153–178. 17

[73] Fernandes, R. M., VanBebber, L. H., Bhattacharya, S., Chandra, P., Keppens, V., Mandrus, D., McGuire, M. A., Sales, B. C., Sefat, A. S., and Schmalian, J. (2010). Effects of nematic fluctuations on the elastic properties of iron arsenide superconductors. *Phys. Rev. Lett.*, 105:157003. 17, 33, 36

[74] Xu, C., Müller, M., and Sachdev, S. (2008). Ising and spin orders in the iron-based superconductors. *Phys. Rev. B*, 78:020501. 17, 33

[75] Fernandes, R. M., Chubukov, A. V., Knolle, J., Eremin, I., and Schmalian, J. (2012). Erratum: Preemptive nematic order, pseudogap, and orbital order in the iron pnictides [Phys. Rev. B 85, 024534 (2012)]. *Phys. Rev. B*, 85:109901. 17, 20, 33, 37, 62, 69, 84

[76] Lee, C.-C., Yin, W.-G., and Ku, W. (2009). Ferro-orbital order and strong magnetic anisotropy in the parent compounds of iron-pnictide superconductors. *Phys. Rev. Lett.*, 103:267001. 17

[77] Chen, C.-C., Moritz, B., van den Brink, J., Devereaux, T. P., and Singh, R. R. P. (2009). Finite-temperature spin dynamics and phase transitions in spin-orbital models. *Phys. Rev. B*, 80:180418.; Chen, C.-C., Maciejko, J., Sorini, A. P., Moritz, B., Singh, R. R. P., and Devereaux, T. P. (2010). Orbital order and spontaneous orthorhombicity in iron pnictides. *Phys. Rev. B*, 82:100504. 17

[78] Lee, W.-C., Lv, W., Tranquada, J. M., and Phillips, P. W. (2012). Impact of dynamic orbital correlations on magnetic excitations in the normal state of iron-based superconductors. *Phys. Rev. B*, 86:094516. 17

[79] Liang, S., Moreo, A., and Dagotto, E. (2013). Nematic state of pnictides stabilized by interplay between spin, orbital, and lattice degrees of freedom. *Phys. Rev. Lett.*, 111:047004. xii, xiii, xix, xxi, 17, 18, 21, 22, 23, 27, 35, 37, 38, 39, 40, 55, 56, 57, 61, 62, 63, 64, 65, 66, 68, 71, 73, 75, 76, 79, 83, 99, 110, 115, 119, 120, 121, 126, 128, 130, 131, 132, 133, 145

[80] $\Delta_{SN}=T_S$-$T_N$ can be regulated by the electron-orbital coupling $\tilde{\lambda}$ leading to a $\Delta_{SN}$ in our model larger than the small values reported for spin systems [see Kamiya, Y., Kawashima, N., and Batista, C. D. (2011). Dimensional crossover in the quasi-two-dimensional ising-O(3) model. *Phys. Rev. B*, 84:214429.; Wysocki, A. L., Belashchenko, K. D., and Antropov, V. P. (2011). Consistent model of magnetism in ferropnictides. *Nature Physics*, 7:485–489.]. 18

[81] Yanagi, Y., Yamakawa, Y. ,Adachi, N., and Ono, Y. (2010). Orbital Order, Structural Transition, and Superconductivity in Iron Pnictides *Journal of the Physical Society of Japan*, 79(12):123707. 20

[82] Dagotto, E., Hotta, T., and Moreo, A. (2001). Colossal magnetoresistant materials: the key role of phase separation. *Physics Reports*, 344(1):1–153. 19, 21, 38, 39, 58, 60, 67, 70, 130, 146

[83] The original definitions of $\Psi$ and $\epsilon$ in [79] have been multiplied by $-1$ so that $\Psi$ and $\epsilon$ are both positive here, as assumed in the GL analysis. 20

[84] The spins in $H_{\mathrm{SL}}$ will only be the localized spins for computational simplicity. 20, 37, 62

[85] Dagotto, E. (2003). pages 125–156. Springer-Verlag Berlin Heidelberg. 21, 39, 100

[86] Kumar, S. and Majumdar, P. (2006). A travelling cluster approximation for lattice fermions strongly coupled to classical degrees of freedom. *The European Physical Journal B - Condensed Matter and Complex Systems*, 50(4):571–579. 21, 36, 39, 76

[87] Mukherjee, A., Patel, N. D., Bishop, C., and Dagotto, E. (2015). Parallelized traveling cluster approximation to study numerically spin-fermion models on large lattices. *Phys. Rev. E*, 91:063303. 21, 36, 39, 76, 111

[88] In unrestricted MC employing the ED method on 8×8 clusters, typically 8,000 thermalization (Th) and up to 100,000 measurement (Ms) steps were used. In restricted MC with ED and 8×8 clusters, the numbers are 8,000 and 20,000 for Th and Ms steps. In restricted MC using TCA+TBC, 4,000 Th and 4,000 Ms steps were employed for a 16×16 cluster with a 4×4 cluster for the MC updates, while for an 8×8 (same MC update cluster) the numbers were 20,000 for Th and 20,000 for Ms steps. 21

[89] Salafranca, J., Alvarez, G., and Dagotto, E. (2009). Electron-lattice coupling and partial nesting as the origin of Fermi arcs in manganites. *Phys. Rev. B*, 80:155133. 21, 36, 40, 133

[90] The value of $k$ comes from Eq. A.12 and is set to $\frac{200eV}{a_0^2}$. This leads to a value of $\frac{1}{\lambda} \approx 250cm^{-1}$ which compares well to the values found in the Raman spectroscopy studies of L. Chauviere et al. Phys. Rev. B 80, 094504 (2009). This also compares well to values found in DFT studies when magnetic moments are added such as L. Boeri et al. Phys. Rev. B 82, 020506(R) (2010) and M. Zbiri et al. Phys. Rev. B 79, 064511 (2009). The equation for conversion to a dimenionless quantity comes from Sec. 5.3 of Ref. [85]. 21

[91] The value of $T^*$ is not the same (but close) for 8×8 and 16×16 lattices due to size effects. Then, the fits for each lattice size are carried out with the $T^*$ of each cluster. xii, 24

[92] Yang, Y.-X., Gallais, Y., Fernandes, R. M., Paul, I., Chauvire, L., Masson, M.-A., Cazayous, M., Sacuto, A., Colson, D., and Forget, A. (2014). Raman scattering as a probe of charge nematic fluctuations in iron based superconductors. *Proceedings of the International Conference on Strongly Correlated Electron Systems*, 3:015001. xiii, 27, 28

[93] Note that in the presence of external strain to detwin crystals, some remaining artificial anisotropy may incorrectly suggest that $(\pi, 0) - (0, \pi)$ are not degenerate above $T_S$ in neutron scattering, leading to the incorrect conclusion that $T_{PG}$ is $T_S$ (for related observations see Dhital, C., Yamani, Z., Tian, W., Zeretsky, J., Sefat, A. S., Wang, Z., Birgeneau, R. J., and Wilson, S. D. (2012). Effect of uniaxial strain on the structural and magnetic phase transitions in $BaFe_2As_2$. *Phys. Rev. Lett.*, 108:087001.; Blomberg, E. C., Kreyssig, A., Tanatar, M. A., Fernandes, R. M., Kim, M. G., Thaler, A., Schmalian, J., Bud'ko, S. L., Canfield, P. C., Goldman, A. I., and Prozorov, R. (2012). Effect of tensile stress on the in-plane resistivity anisotropy in $BaFe_2As_2$. *Phys. Rev. B*, 85:144509.). 30

[94] Our results should be compared against the photoemission experiments reported by Shimojima, T., Sonobe, T., Malaeb, W., Shinada, K., Chainani, A., Shin, S., Yoshida, T., Ideta, S., Fujimori, A., Kumigashira, H., Ono, K., Nakashima, Y., Anzai, H., Arita, M., Ino, A., Namatame, H., Taniguchi, M., Nakajima, M., Uchida, S., Tomioka, Y., Ito, T., Kihou, K., Lee, C. H., Iyo, A., Eisaki, H., Ohgushi, K., Kasahara, S., Terashima, T., Ikeda, H., Shibauchi, T., Matsuda, Y., and Ishizaka, K. (2014). Pseudogap formation above the superconducting dome in iron pnictides. *Phys. Rev. B*, 89:045101. (see for instance their Figure 6). Infrared studies correlating the presence of a pseudogap with antiferromagnetic fluctuations can also be found in Moon, S. J., Schafgans, A. A., Kasahara, S., Shibauchi, T., Terashima, T., Matsuda, Y., Tanatar, M. A., Prozorov, R., Thaler, A., Canfield, P. C., Sefat, A. S., Mandrus, D., and Basov, D. N. (2012). Infrared measurement of the pseudogap of P-doped and Co-doped high-temperature $BaFe_2As_2$ superconductors. *Phys. Rev. Lett.*, 109:027006. 30

[95] Yu, R., Trinh, K. T., Moreo, A., Daghofer, M., Riera, J. A., Haas, S., and Dagotto, E. (2009). Magnetic and metallic state at intermediate Hubbard $U$ coupling in multiorbital models for undoped iron pnictides. *Phys. Rev. B*, 79:104510. 32

[96] Niedziela, J. L., Parshall, D., Lokshin, K. A., Sefat, A. S., Alatas, A., and Egami, T. (2011). Phonon softening near the structural transition in $BaFe_2As_2$ observed by inelastic x-ray scattering. *Phys. Rev. B*, 84:224305. 32, 36

[97] Rosenthal, E. P., Andrade, E. F., Arguello, C. J., Fernandes, R. M., Xing, L. Y., Wang, X. C., Jin, C. Q., Millis, A. J., and Pasupathy, A. N. (2014). Visualization of electron nematicity and unidirectional antiferroic fluctuations at high temperatures in NaFeAs. *Nature Physics*, 10:225–232. 32, 55

[98] Liang, S., Bishop, C. B., Moreo, A., and Dagotto, E. (2015). Isotropic in-plane quenched disorder and dilution induce a robust nematic state in electron-doped pnictides. *Phys. Rev. B*, 92:104512. 33, 71, 85, 102

[99] For the research project that was detailed in this chapter and published in Ref. [98], my contributions were as follows. I was responsible for helping to alter the code and then submit the code to the compute cluster. I was responsible for performing analysis on the resulting data and calculating observables such as susceptibilities and spin-spin correlations. Plotting the final phase diagrams was also part of my contribution. There are many possible types of disorder and degree of quenching that is applied to the classics spins. I was part of the discussion that choose the configuration of parameters that controlled the types of disorder in the model. We then interpreted the results in collaboration. 33

[100] Kuo, H.-H., Chu, J.-H., Riggs, S. C., Yu, L., McMahon, P. L., De Greve, K., Yamamoto, Y., Analytis, J. G., and Fisher, I. R. (2011). Possible origin of the nonmonotonic doping dependence of the in-plane resistivity anisotropy of $Ba(Fe_{1-x}T_x)_2As_2$ ($T =$ Co, Ni and Cu). *Phys. Rev. B*, 84:054540. 33

[101] Chen, X., Dai, P., Feng, D., Xiang, T., and Zhang, F.-C. (2014). Iron-based high transition temperature superconductors. *National Science Review*, 1(3):371. 34, 50, 51, 70

[102] Rullier-Albenque, F., Colson, D., Forget, A., Thuéry, P., and Poissonnet, S. (2010). Hole and electron contributions to the transport properties of $Ba(Fe_{1-x}Ru_x)_2As_2$ single crystals. *Phys. Rev. B*, 81:224503. xv, 34, 49, 50

[103] Vilmercati, P., Mo, S.-K., Fedorov, A., McGuire, M.A., Sefat, A., Sales, B., Mandrus, D., Singh, D., Ku, W., Johnston, S., and Mannella, N. (2016). Nonrigid band shift and

nonmonotonic electronic structure changes upon doping in the normal state of the pnictide high-temperature superconductor $Ba(Fe_{1x}Co_x)_2As_2$ *Phys. Rev. B*, 94:195147. 34, 35, 50

[104] Ideta, S., Yoshida, T., Nishi, I.,Fujimori, A., Kotani, Y., Ono, K., Nakashima, Y., Yamaichi, S., Sasagawa, T., Nakajima, M., Kihou, K., Tomioka, Y., Lee, C. H., Iyo, A., Eisaki, H., Ito, T., Uchida, S., Arit, R. (2013). Dependence of Carrier Doping on the Impurity Potential in Transition-Metal-Substituted FeAs-Based Superconductors *Phys. Rev. Lett.*, 110:107007. 34, 50

[105] Berlijn, T., Lin, C.-H., Garber, W., Ku, W.(2012). Do Transition-Metal Substitutions Dope Carriers in Iron-Based Superconductors?. *Phys. Rev. Lett.*, 108:207003. 34, 50

[106] Wang, L., Berlijn, T., Wang, Y., Lin, C.-H., Hirschfeld, P. J., and Ku, W. (2013). Effects of disordered Ru substitution in BaFe$_2$As$_2$: Possible realization of superdiffusion in real materials. *Phys. Rev. Lett.*, 110:037001. 34, 35, 50

[107] The upper critical temperatures $T_N$ and $T_S$ are mainly regulated by $x$, but there are still differences between different transition metals. For instance, to scale almost exactly these critical temperatures for the cases of Ni and Co, a factor 1.6 is needed to relate the dopant concentrations, as shown in Kuo, H.-H. and Fisher, I. R. (2014). Effect of disorder on the resistivity anisotropy near the electronic nematic phase transition in pure and electron-doped BaFe$_2$As$_2$. *Phys. Rev. Lett.*, 112:227001. In that publication it was also shown that the strain-induced resistivity anisotropy in the tetragonal state is independent of disorder. We will address this subject in future publications. 34

[108] Nakajima, M., Ishida, S., Tomioka, Y., Kihou, K., Lee, C. H., Iyo, A., Ito, T., Kakeshita, T., Eisaki, H., and Uchida, S. (2012). Effect of co doping on the in-plane anisotropy in the optical spectrum of underdoped Ba(Fe$_{1-x}$Co$_x$)$_2$As$_2$. *Phys. Rev. Lett.*, 109:217003. 34, 54

[109] Chuang, T.-M., Allan, M. P., Lee, J., Xie, Y., Ni, N., Bud'ko, S. L., Boebinger, G. S., Canfield, P. C., and Davis, J. C. (2010). Nematic electronic structure in the "parent" state of the iron-based superconductor Ca(Fe$_{1-x}$Co$_x$)$_2$As$_2$. *Science*, 327(5962):181–184. 34, 54

[110] Allan, M. P., Chuang, T.-M., Massee, F., Xie, Y., Ni, N., Bud/'ko, S. L., Boebinger, G. S., Wang, Q., Dessau, D. S., Canfield, P. C., Golden, M. S., and Davis, J. C. (2013). Anisotropic impurity states, quasiparticle scattering and nematic transport in underdoped $Ca(Fe_{1-x}Co_x)_2As_2$. *Nature Physics*, 9:220–224. 34, 54

[111] Iye, T., Julien, M.-H., Mayaffre, H., Horvati, M., Berthier, C., Ishida, K., Ikeda, H., Kasahara, S., Shibauchi, T., and Matsuda, Y. (2015). Emergence of orbital nematicity in the tetragonal phase of $BaFe_2(As_{1x}P_x)_2$. *Journal of the Physical Society of Japan*, 84(4):043705. 34

[112] The importance of disorder near a nematic quantum critical point has been recently remarked in Kuo, H.-H., Chu, J.-H., Palmstrom, J. C., Kivelson, S. A., and Fisher, I. R. (2016). Ubiquitous signatures of nematic quantum criticality in optimally doped Fe-based superconductors. *Science*, 352(6288):958–962. 34, 74

[113] Nie, L., Tarjus, G., and Kivelson, S. A. (2014). Quenched disorder and vestigial nematicity in the pseudogap regime of the cuprates. *Proceedings of the National Academy of Sciences*, 111(22):7980–7985. 34

[114] Dagotto, E. (2013). Colloquium: The unexpected properties of alkali metal iron selenide superconductors. *Rev. Mod. Phys.*, 85:849–867. 35, 69

[115] Bondino, F., Magnano, E., Malvestuto, M., Parmigiani, F., McGuire, M. A., Sefat, A. S., Sales, B. C., Jin, R., Mandrus, D., Plummer, E. W., Singh, D. J., and Mannella, N. (2008). Evidence for strong itinerant spin fluctuations in the normal state of $CeFeAsO_{0.89}F_{0.11}$ iron-oxypnictide superconductors. *Phys. Rev. Lett.*, 101:267001. 35

[116] Schmiedt, J., Brydon, P. M. R., and Timm, C. (2012). Doping dependence of antiferromagnetism in models of the pnictides. *Phys. Rev. B*, 85:214425. 35

[117] Gastiasoro, M. N., Hirschfeld, P. J., and Andersen, B. M. (2014). Origin of electronic dimers in the spin-density wave phase of Fe-based superconductors. *Phys. Rev. B*, 89:100502.; Gastiasoro, M. N., Paul, I., Wang, Y., Hirschfeld, P. J., and Andersen, B. M. (2014). Emergent defect states as a source of resistivity anisotropy in the nematic phase

of iron pnictides. *Phys. Rev. Lett.*, 113:127001.; Wang, Y., Gastiasoro, M. N., Andersen, B. M., Tomić, M., Jeschke, H. O., Valentí, R., Paul, I., and Hirschfeld, P. J. (2015). Effects of Lifshitz transition on charge transport in magnetic phases of Fe-based superconductors. *Phys. Rev. Lett.*, 114:097003. 35

[118] Vavilov, M. G. and Chubukov, A. V. (2011). Phase diagram of iron pnictides if doping acts as a source of disorder. *Phys. Rev. B*, 84:214521. 36

[119] Fernandes, R. M., Vavilov, M. G., and Chubukov, A. V. (2012). Enhancement of $T_c$ by disorder in underdoped iron pnictide superconductors. *Phys. Rev. B*, 85:140512. 36

[120] The magnitude of the localized spins is set to $S_\mathbf{i} = 1$ since the actual value is absorbed into the Hamiltonian parameters. For example if $S_\mathbf{i}$ is changed to a value $S'$ the Hamiltonian parameters related to the site $\mathbf{i}$ change in the following way: $J_{\mathrm{H},\mathbf{i}} = S' J_\mathrm{H}$, $g_\mathbf{i} = S'g$, $J_{\mathrm{NN},\mathbf{i}} = S' J_\mathrm{NN}$ and $J_{\mathrm{NNN},\mathbf{i}} = S' J_\mathrm{NNN}$. 37, 39

[121] Sefat, A. S., Singh, D. J., Jin, R., McGuire, M. A., Sales, B. C., and Mandrus, D. (2009). Renormalized behavior and proximity of $BaCo_2As_2$ to a magnetic quantum critical point. *Phys. Rev. B*, 79:024512. 39, 43, 56

[122] Capati, M., Grilli, M., and Lorenzana, J. (2011). Nematic phase without heisenberg physics in FeAs planes. *Phys. Rev. B*, 84:214520. 40

[123] Smaller, and for some points, larger systems with up to $96 \times 96$ sites where studied to monitor that finite size effects are very small in the $64 \times 64$ clusters used to obtain the results presented here. 40

[124] The value was chosen to simulate the on-site potential reduction with respect to the background Fe potential observed experimentally. See Levy, G., Sutarto, R., Chevrier, D., Regier, T., Blyth, R., Geck, J., Wurmehl, S., Harnagea, L., Wadati, H., Mizokawa, T., Elfimov, I. S., Damascelli, A., and Sawatzky, G. A. (2012). Probing the role of Co substitution in the electronic structure of iron pnictides. *Phys. Rev. Lett.*, 109:077001. 43

[125] Kim, M. G., Soh, J., Lang, J., Dean, M. P. M., Thaler, A., Bud'ko, S. L., Canfield, P. C., Bourret-Courchesne, E., Kreyssig, A., Goldman, A. I., and Birgeneau, R. J. (2013).

Spin polarization of ru in superconducting $Ba(Fe_{0.795}Ru_{0.205})_2As_2$ studied by x-ray resonant magnetic scattering. *Phys. Rev. B*, 88:014424. 50, 56

[126] Ishida, S., Nakajima, M., Liang, T., Kihou, K., Lee, C. H., Iyo, A., Eisaki, H., Kakeshita, T., Tomioka, Y., Ito, T., and Uchida, S. (2013). Anisotropy of the in-plane resistivity of underdoped $Ba(Fe_{1-x}Co_x)_2As_2$ superconductors induced by impurity scattering in the antiferromagnetic orthorhombic phase. *Phys. Rev. Lett.*, 110:207001. 54

[127] Dong, T., Chen, Z. G., Yuan, R. H., Hu, B. F., Cheng, B., and Wang, N. L. (2010). Formation of partial energy gap below the structural phase transition and the rare-earth element-substitution effect on infrared phonons in $Re$FeAsO ($Re =$ La, Nd, and Sm). *Phys. Rev. B*, 82:054522. 55

[128] Singh, D. J. (2009). Electronic structure of $BaCu_2As_2$ and $SrCu_2As_2$: $sp$-band metals. *Phys. Rev. B*, 79:153102. 56

[129] Analytis, J. G., Chu, J.-H., McDonald, R. D., Riggs, S. C., and Fisher, I. R. (2010). Enhanced Fermi-surface nesting in superconducting $BaFe_2(As_{1-x}\mathbf{P}_x)_2$ revealed by the de Haas–van Alphen effect. *Phys. Rev. Lett.*, 105:207004. 56

[130] For the research project that was presented in this chapter and published in Ref. [43], my contributions were as follows. I was solely responsible for writing the Monte Carlo code and submitting it to the compute cluster. I also was involved in creating the order parameters with the $B_{2g}$ representation and calculating the spin coupling renormalization factors. I was responsible for exploring the parameter space that included the Hund couping ($J_H$), the Heisenberg couplings ($J_{NN}$, and $J_{NNN}$), and the spin-lattice couplings ($g_{12}$ and $g_{66}$) to find physically relevant features. This was first done at low temperatures and then expanded for select couplings at high temperatures. I was also responsible for writing and submitting the resistivity code that calculated the anisotropy as well as the code that calculated the Fermi Surface. Because of the amount of resolution to demonstrate the resistance anisotropy and to fill in enough of the Fermi Surface, TBC were needed for both of these calculations. The several different orbital hoppings and directions also made this a non-trivial calculation. I was responsible for creating the final plots as well. 58

[131] Yin, Z. P., Haule, K., and Kotliar, G. (2011). Kinetic frustration and the nature of the magnetic and paramagnetic states in iron pnictides and ironchalcogenides. *Nature Materials*, 10:932–935. 58, 69

[132] Recent results also indicate charge ordering in FeTe: Li, W., Yin, W.-G., Wang, L., He, K., Ma, X., Xue, Q.-K., and Chen, X. (2016). Charge ordering in stoichiometric FeTe: Scanning tunneling microscopy and spectroscopy. *Phys. Rev. B*, 93:041101. 58, 70

[133] Zhang, Y., Chen, F., He, C., Yang, L. X., Xie, B. P., Xie, Y. L., Chen, X. H., Fang, M., Arita, M., Shimada, K., Namatame, H., Taniguchi, M., Hu, J. P., and Feng, D. L. (2010). Strong correlations and spin-density-wave phase induced by a massive spectral weight redistribution in $\alpha$-Fe$_{1.06}$Te. *Phys. Rev. B*, 82:165113. 58

[134] Dai, Y. M., Akrap, A., Schneeloch, J., Zhong, R. D., Liu, T. S., Gu, G. D., Li, Q., and Homes, C. C. (2014). Spectral weight transfer in strongly correlated Fe$_{1.03}$Te. *Phys. Rev. B*, 90:121114. 58

[135] Xia, Y., Qian, D., Wray, L., Hsieh, D., Chen, G. F., Luo, J. L., Wang, N. L., and Hasan, M. Z. (2009). Fermi surface topology and low-lying quasiparticle dynamics of parent Fe$_{1+x}$Te/Se superconductor. *Phys. Rev. Lett.*, 103:037002. 58, 67

[136] The importance of the Hund coupling was also remarked within ARPES by Lin, P.-H., Texier, Y., Taleb-Ibrahimi, A., Le Fèvre, P., Bertran, F., Giannini, E., Grioni, M., and Brouet, V. (2013). Nature of the bad metallic behavior of Fe$_{1.06}$Te inferred from its evolution in the magnetic state. *Phys. Rev. Lett.*, 111:217002. 58, 60

[137] Bao, W., Qiu, Y., Huang, Q., Green, M. A., Zajdel, P., Fitzsimmons, M. R., Zhernenkov, M., Chang, S., Fang, M., Qian, B., Vehstedt, E. K., Yang, J., Pham, H. M., Spinu, L., and Mao, Z. Q. (2009). Tunable $(\delta\pi, \delta\pi)$-type antiferromagnetic order in $\alpha$-Fe(Te,Se) superconductors. *Phys. Rev. Lett.*, 102:247001. xxi, 58, 59, 65, 66, 70, 132, 140, 145

[138] Ma, F., Ji, W., Hu, J., Lu, Z.-Y., and Xiang, T. (2009). First-principles calculations of the electronic structure of tetragonal $\alpha$-FeTe and $\alpha$-FeSe crystals: Evidence for a bicollinear antiferromagnetic order. *Phys. Rev. Lett.*, 102:177003. 58

[139] Fang, C., Bernevig, B. A., and Hu, J. (2009). Theory of magnetic order in $Fe_{1+y}Te_{1-x}Se_x$. *Europhysics Letters*, 86(6):67005. 58

[140] In addition, discrepancies with neutron scattering have been unveiled: Lipscombe, O. J., Chen, G. F., Fang, C., Perring, T. G., Abernathy, D. L., Christianson, A. D., Egami, T., Wang, N., Hu, J., and Dai, P. (2011). Spin waves in the $(\pi, 0)$ magnetically ordered iron chalcogenide $Fe_{1.05}Te$. *Phys. Rev. Lett.*, 106:057004.; Chi, S., Rodriguez-Rivera, J. A., Lynn, J. W., Zhang, C., Phelan, D., Singh, D. K., Paul, R., and Dai, P. (2011). Common origin of the two types of magnetic fluctuations in iron chalcogenides. *Phys. Rev. B*, 84:214407. 58

[141] Hartree-Fock real-space studies of the five orbital Hubbard model without lattice distortions revealed a rich phase diagram (See Luo, Q. and Dagotto, E. (2014). Magnetic phase diagram of a five-orbital hubbard model in the real-space hartree-fock approximation varying the electronic density. *Phys. Rev. B*, 89:045115). Among the plethora of different magnetic states, the E phase was found but in a very small and unrealistic region at large $U$ and $n \sim 5.75$. 58

[142] The lattice degrees of freedom introduced here can be integrated out and generate a biquadratic term that favors bicollinear order, see Ducatman, S., Fernandes, R. M., and Perkins, N. B. (2014). Theory of the evolution of magnetic order in $fe_{1+y}Te$ compounds with increasing interstitial iron. *Phys. Rev. B*, 90:165123. 58, 86

[143] Chen, G. F., Chen, Z. G., Dong, J., Hu, W. Z., Li, G., Zhang, X. D., Zheng, P., Luo, J. L., and Wang, N. L. (2009). Electronic properties of single-crystalline $Fe_{1.05}Te$ and $Fe_{1.03}Se_{0.30}Te_{0.70}$. *Phys. Rev. B*, 79:140509. 59, 70

[144] Fobes, D., Zaliznyak, I. A., Xu, Z., Zhong, R., Gu, G., Tranquada, J. M., Harriger, L., Singh, D., Garlea, V. O., Lumsden, M., and Winn, B. (2014). Ferro-orbital ordering transition in iron telluride $Fe_{1+y}Te$. *Phys. Rev. Lett.*, 112:187202. 59, 70, 109

[145] Huang, Q., Qiu, Y., Bao, W., Green, M. A., Lynn, J. W., Gasparovic, Y. C., Wu, T., Wu, G., and Chen, X. H. (2008). Neutron-diffraction measurements of magnetic order and a structural transition in the parent $BaFe_2As_2$ compound of FeAs-based high-temperature superconductors. *Phys. Rev. Lett.*, 101:257003. xxi, 59, 70, 132, 140

[146] In [144] an electronic delocalization transition was proposed to lift the $xz/yz$ orbital degeneracy leading to ferro-orbital order along the ferromagnetic zigzag chains of the bicollinear state of $Fe_{1+y}Te$. See also Zaliznyak, I., Savici, A. T., Lumsden, M., Tsvelik, A., Hu, R., and Petrovic, C. (2015). Spin-liquid polymorphism in a correlated electron system on the threshold of superconductivity. *Proceedings of the National Academy of Sciences*, 112(33):10316–10320. 59

[147] Liu, L., Mikami, T., Takahashi, M., Ishida, S., Kakeshita, T., Okazaki, K., Fujimori, A., and Uchida, S. (2015). Reversed anisotropy of the in-plane resistivity in the antiferromagnetic phase of iron tellurides. *Phys. Rev. B*, 91:134502. 59, 66, 86, 144

[148] Jiang, J., He, C., Zhang, Y., Xu, M., Ge, Q. Q., Ye, Z. R., Chen, F., Xie, B. P., and Feng, D. L. (2013). Distinct in-plane resistivity anisotropy in a detwinned FeTe single crystal: Evidence for a Hund's metal. *Phys. Rev. B*, 88:115130. xvi, 59, 60, 66, 86, 144

[149] Zaliznyak, I. A., Xu, Z., Tranquada, J. M., Gu, G., Tsvelik, A. M., and Stone, M. B. (2011). Unconventional temperature enhanced magnetism in $Fe_{1.1}Te$. *Phys. Rev. Lett.*, 107:216403. 60

[150] Other ARPES results were interpreted via polarons, as in manganites, also concluding that the lattice plays an important role: Liu, Z. K., He, R.-H., Lu, D. H., Yi, M., Chen, Y. L., Hashimoto, M., Moore, R. G., Mo, S.-K., Nowadnick, E. A., Hu, J., Liu, T. J., Mao, Z. Q., Devereaux, T. P., Hussain, Z., and Shen, Z.-X. (2013). Measurement of coherent polarons in the strongly coupled antiferromagnetically ordered iron-chalcogenide $Fe_{1.02}Te$ using angle-resolved photoemission spectroscopy. *Phys. Rev. Lett.*, 110:037003. Mechanisms relying on Jahn-Teller distortions, double exchange processes and its associated Hund coupling, as in manganites, have also been discussed (see Turner, A. M., Wang, F., and Vishwanath, A. (2009). Kinetic magnetism and orbital order in iron

telluride. *Phys. Rev. B*, 80:224504.; Hirayama, M., Misawa, T., Miyake, T., and Imada, M. (2015). Ab initio studies of magnetism in the iron chalcogenides FeTe and FeSe. *Journal of the Physical Society of Japan*, 84(9):093703. 60

[151] The localized spins' magnitude is set to $S_{\mathbf{i}} = 1$. Its actual value can be absorbed into the Hamiltonian parameters. 61, 73

[152] Any ratio larger than $\frac{1}{2}$ leads to similar results. 61

[153] A complete study of the bicollinear magnetic state requires a five-orbital Hubbard model, plus the lattice, all at finite temperature. Such a formidable challenge is not practical: the SF model is a simplification that allows for the study of structural, orbital, and magnetic effects simultaneously. 62

[154] Rodriguez, E. E., Stock, C., Zajdel, P., Krycka, K. L., Majkrzak, C. F., Zavalij, P., and Green, M. A. (2011). Magnetic-crystallographic phase diagram of the superconducting parent compound $Fe_{1+x}Te$. *Phys. Rev. B*, 84:064403. 62, 65, 142

[155] The degeneracy of the bicollinear states with momentum $\left(\frac{\pi}{2}, \frac{\pi}{2}\right)$ and $\left(\frac{\pi}{2}, -\frac{\pi}{2}\right)$ is broken by the $\mathcal{M}_{\mathrm{ono}}$ distortion. Here we assume that the state with momentum $\left(\frac{\pi}{2}, -\frac{\pi}{2}\right)$ is stabilized. 63

[156] The physical range for $J_{\mathrm{H}}$, $J_{\mathrm{NN}}$, and $J_{\mathrm{NNN}}$ was also extensively discussed before in [61, 79] (see Appendix H as well). 63

[157] Mizuguchi, Y., Hamada, K., Goto, K., Takatsu, H., Kadowaki, H., and Miura, O. (2012). Evolution of two-step structural phase transition in $Fe_{1+d}Te$ detected by low-temperature x-ray diffraction. *Solid State Communications*, 152(12):1047–1051. 65, 142

[158] The low-temperature (10 K) phase diagrams varying $\tilde{g}_{66}$ and $\tilde{g}_{12}$ are also in G [see Fig. G.1 (Fig. G.2) with (without) Heisenberg couplings]: in a broad range of couplings the bicollinear/$\mathcal{M}_{\mathrm{ono}}$ state is spontaneously stabilized. 65

[159] Daghofer, M., Luo, Q.-L., Yu, R., Yao, D. X., Moreo, A., and Dagotto, E. (2010). Orbital-weight redistribution triggered by spin order in the pnictides. *Phys. Rev. B*, 81:180514. 66, 68

[160] Chalcogenides have higher magnetic moments than pnictides, thus likely larger Hund couplings. We also noticed that for $J_H = 0.1$ eV we found that the reversed anisotropy was still there but reduced (see Appendix F). 67

[161] Nesting tendencies, even if not crucial, could potentially lead to phase separation (PS) effects [Sboychakov, A. O., Rozhkov, A. V., Kugel, K. I., Rakhmanov, A. L., and Nori, F. (2013). Electronic phase separation in iron pnictides. *Phys. Rev. B*, 88:195142]. While we checked that PS is not present in our model in the undoped regime studied, it may occur upon doping. 67

[162] Bishop, C. B., Herbrych, J., Dagotto, E., and Moreo, A. (2017). Possible Bicollinear Nematic State with Monoclinic Lattice Distortions in Iron Telluride Compounds. *Phys. Rev. B*, 96:035144. 69, 111

[163] For the research project that was detailed in this chapter and published in Ref. [162], my contributions were as follows. I was solely responsible for writing the Monte Carlo code. This included devising a new method for implementing a parallelized version of the Traveling cluster algorithm. This Hamiltonian includes interactions of neighboring sites and global variables which presented different obstacles than in the test case of Ref. [87]. I submitted the code to the compute cluster and performed analysis on the data to calculate observables. I was responsible for exploring the parameter space of $\lambda_{12}$ and $g_{12}$ to find the $B_{2g}$ nematic state. 69

[164] Rotundu, C. R. and Birgeneau, R. J. (2011). First- and second-order magnetic and structural transitions in $BaFe_{2(1-x)}Co_{2x}As_2$. *Phys. Rev. B*, 84:092501. 69, 70

[165] Zhou, R., Li, Z., Yang, J., Sun, D. L., Lin, C. T., and Zheng, G.-q. (2013). Quantum criticality in electron-doped $BaFe_{2x}Ni_xAs_2$. *Nature Communications*, 4. 69, 70

[166] Saha, S. R., Butch, N. P., Drye, T., Magill, J., Ziemak, S., Kirshenbaum, K., Zavalij, P. Y., Lynn, J. W., and Paglione, J. (2012). Structural collapse and superconductivity in rare-earth-doped $CaFe_2As_2$. *Phys. Rev. B*, 85:024525. 70

[167] Hsin-Hua Lai, Shou-Shu Gong, Wen-Jun Hu, and Qimiao Si, arXiv:1608.08206. 70

[168] Chandra, P., Coleman, P., and Larkin, A. I. (1990). Ising transition in frustrated Heisenberg models. *Phys. Rev. Lett.*, 64:88–91. 71

[169] Notice that the magnetic structure factor for the state in Fig. 5.1(a) [5.1(b)] has peaks at both momentum $(\frac{\pi}{2}, -\frac{\pi}{2})$ and $(-\frac{\pi}{2}, \frac{\pi}{2})$ [$(\frac{\pi}{2}, \frac{\pi}{2})$ and $(-\frac{\pi}{2}, -\frac{\pi}{2})$]. 71

[170] Hoyer, M., Fernandes, R. M., Levchenko, A., and Schmalian, J. (2016). Disorder-promoted $C_4$-symmetric magnetic order in iron-based superconductors. *Phys. Rev. B*, 93:144414. 71

[171] Calculations for $J_{\mathrm{NN}} = 0.012$ eV and $J_{\mathrm{NNN}} = 0.008$ eV were performed and only quantitative changes in the presented results were observed. 74

[172] Wen, J., Xu, Z., Xu, G., Lumsden, M. D., Valdivia, P. N., Bourret-Courchesne, E., Gu, G., Lee, D.-H., Tranquada, J. M., and Birgeneau, R. J. (2012). Magnetic order tuned by cu substitution in $Fe_{1.1-z}Cu_zTe$. *Phys. Rev. B*, 86:024401. 85

[173] Valdivia, P. N., Kim, M. G., Forrest, T. R., Xu, Z., Wang, M., Wu, H., Harringer, L. W., Bourret-Courchesne, E. D., and Birgeneau, R. J. (2015). Copper-substituted iron telluride: A phase diagram. *Phys. Rev. B*, 91:224424. 85

[174] Janaki, J., Geetha Kumary, T., Thirumurugan, N., Mani, A., Das, A., NarasimhaRao, G. V., and Bharathi, A. (2012). Influence of Ni doping on the low temperature properties of layered $Fe_{1+\delta}Te$. *Journal of Superconductivity and Novel Magnetism*, 25(2):209–214. 85

[175] Zhu, Y., Li, L., Yang, Z., Zhang, Z., Yuan, B., Chen, J., Du, H., Sun, Y., and Zhang, Y. (2016). Co-doping effects on the transport and magnetic properties of FeTe. *Journal of Magnetism and Magnetic Materials*, 397:1–5. 86

[176] Zhang, W., Park, J. T., Lu, X., Wei, Y., Ma, X., Hao, L., Dai, P., Meng, Z. Y., Yang, Y.-f., Luo, H., and Li, S. (2016). Effect of nematic order on the low-energy spin fluctuations in detwinned $BaFe_{1.935}Ni_{0.065}As_2$. *Phys. Rev. Lett.*, 117:227003. 86

[177] Ducatman, S., Perkins, N. B., and Chubukov, A. (2012). Magnetism in parent iron chalcogenides: Quantum fluctuations select plaquette order. *Phys. Rev. Lett.*, 109:157206. 86

[178] Zhang, G., Glasbrenner, J. K., Flint, R., Mazin, I. I., and Fernandes, R. M. (2017). Double-stage nematic bond ordering above double stripe magnetism: Application to $BaTi_2Sb_2O$. *Phys. Rev. B*, 95:174402. 86

[179] Ashcroft, Neil, and Mermin, N. David (1976). Solid State Physics. pages 747–750. Saunders College Publishers, Philadelphia. 120

[180] Vergs, J. (1999). Computational implementation of the kubo formula for the static conductance: Application to two-dimensional quantum dots. *Computer Physics Communications*, 118(1):71 – 80. 134

[181] Tanatar, M. A., Böhmer, A. E., Timmons, E. I., Schütt, M., Drachuck, G., Taufour, V., Kothapalli, K., Kreyssig, A., Bud'ko, S. L., Canfield, P. C., Fernandes, R. M., and Prozorov, R. (2016). Origin of the resistivity anisotropy in the nematic phase of FeSe. *Phys. Rev. Lett.*, 117:127001. 144

[182] Notice that in the bicollinear phase illustrated in Fig. 4.2, the AFM direction is $x - y$. 145

# Appendices

# Appendix A

# Full Spin-Fermion Hamiltonian with B$_{1g}$ Lattice Couplings

The full Hamiltonian of the spin-fermion model with lattice interactions incorporated is here provided.

The same Hamiltonian was also used in Ref. [79]. The model is given by:

$$H_{\text{SF}} = H_{\text{Hopp}} + H_{\text{Hund}} + H_{\text{Heis}} + H_{\text{SLO}} + H_{\text{OLO}} + H_{\text{Stiff}}. \tag{A.1}$$

The hopping component is made of three contributions,

$$H_{\text{Hopp}} = H_{xz,yz} + H_{xy} + H_{xz,yz;xy}. \tag{A.2}$$

The first term involves the $xz$ and $yz$ orbitals:

$$H_{xz,yz} = \{-t_1 \sum_{\mathbf{i},\sigma} (d^\dagger_{\mathbf{i},xz,\sigma} d_{\mathbf{i}+\hat{y},xz,\sigma} + d^\dagger_{\mathbf{i},yz,\sigma} d_{\mathbf{i}+\hat{x},yz,\sigma})$$

$$- t_2 \sum_{\mathbf{i},\sigma} (d^\dagger_{\mathbf{i},xz,\sigma} d_{\mathbf{i}+\hat{x},xz,\sigma} + d^\dagger_{\mathbf{i},yz,\sigma} d_{\mathbf{i}+\hat{y},yz,\sigma})$$

$$- t_3 \sum_{\mathbf{i},\hat{\mu}\neq\hat{\nu},\sigma} (d^\dagger_{\mathbf{i},xz,\sigma} d_{\mathbf{i}+\hat{\mu}+\hat{\nu},xz,\sigma} + d^\dagger_{\mathbf{i},yz,\sigma} d_{\mathbf{i}+\hat{\mu}+\hat{\nu},yz,\sigma})$$

$$+ t_4 \sum_{\mathbf{i},\sigma} (d^\dagger_{\mathbf{i},xz,\sigma} d_{\mathbf{i}+\hat{x}+\hat{y},yz,\sigma} + d^\dagger_{\mathbf{i},yz,\sigma} d_{\mathbf{i}+\hat{x}+\hat{y},xz,\sigma})$$

$$- t_4 \sum_{\mathbf{i},\sigma} (d^\dagger_{\mathbf{i},xz,\sigma} d_{\mathbf{i}+\hat{x}-\hat{y},yz,\sigma} + d^\dagger_{\mathbf{i},yz,\sigma} d_{\mathbf{i}+\hat{x}-\hat{y},xz,\sigma})$$

$$+ h.c.\} - \mu \sum_{\mathbf{i}} (n_{\mathbf{i},xz} + n_{\mathbf{i},yz}). \tag{A.3}$$

The second term contains the hoppings related with the $xy$ orbital:

$$H_{xy} = t_5 \sum_{\mathbf{i},\hat{\mu},\sigma} (d^\dagger_{\mathbf{i},xy,\sigma} d_{\mathbf{i}+\hat{\mu},xy,\sigma} + h.c.)$$

$$- t_6 \sum_{\mathbf{i},\hat{\mu}\neq\hat{\nu},\sigma} (d^\dagger_{\mathbf{i},xy,\sigma} d_{\mathbf{i}+\hat{\mu}+\hat{\nu},xy,\sigma} + h.c.)$$

$$+ \Delta_{xy} \sum_{\mathbf{i}} n_{\mathbf{i},xy} - \mu \sum_{\mathbf{i}} n_{\mathbf{i},xy}, \tag{A.4}$$

The last hopping term is:

$$
\begin{aligned}
H_{\text{xz,yz;xy}} = & - t_7 \sum_{\mathbf{i},\sigma} [(-1)^{|\mathbf{i}|} d^\dagger_{\mathbf{i},xz,\sigma} d_{\mathbf{i}+\hat{x},xy,\sigma} + h.c.] \\
& - t_7 \sum_{\mathbf{i},\sigma} [(-1)^{|\mathbf{i}|} d^\dagger_{\mathbf{i},xy,\sigma} d_{\mathbf{i}+\hat{x},xz,\sigma} + h.c.] \\
& - t_7 \sum_{\mathbf{i},\sigma} [(-1)^{|\mathbf{i}|} d^\dagger_{\mathbf{i},yz,\sigma} d_{\mathbf{i}+\hat{y},xy,\sigma} + h.c.] \\
& - t_7 \sum_{\mathbf{i},\sigma} [(-1)^{|\mathbf{i}|} d^\dagger_{\mathbf{i},xy,\sigma} d_{\mathbf{i}+\hat{y},yz,\sigma} + h.c.] \\
& - t_8 \sum_{\mathbf{i},\sigma} [(-1)^{|\mathbf{i}|} d^\dagger_{\mathbf{i},xz,\sigma} d_{\mathbf{i}+\hat{x}+\hat{y},xy,\sigma} + h.c.] \\
& + t_8 \sum_{\mathbf{i},\sigma} [(-1)^{|\mathbf{i}|} d^\dagger_{\mathbf{i},xy,\sigma} d_{\mathbf{i}+\hat{x}+\hat{y},xz,\sigma} + h.c.] \\
& - t_8 \sum_{\mathbf{i},\sigma} [(-1)^{|\mathbf{i}|} d^\dagger_{\mathbf{i},xz,\sigma} d_{\mathbf{i}+\hat{x}-\hat{y},xy,\sigma} + h.c.] \\
& + t_8 \sum_{\mathbf{i},\sigma} [(-1)^{|\mathbf{i}|} d^\dagger_{\mathbf{i},xy,\sigma} d_{\mathbf{i}+\hat{x}-\hat{y},xz,y\sigma} + h.c.] \\
& - t_8 \sum_{\mathbf{i},\sigma} [(-1)^{|\mathbf{i}|} d^\dagger_{\mathbf{i},yz,\sigma} d_{\mathbf{i}+\hat{x}+\hat{y},xy,\sigma} + h.c.] \\
& + t_8 \sum_{\mathbf{i},\sigma} [(-1)^{|\mathbf{i}|} d^\dagger_{\mathbf{i},xy,\sigma} d_{\mathbf{i}+\hat{x}+\hat{y},yz,\sigma} + h.c.] \\
& + t_8 \sum_{\mathbf{i},\sigma} [(-1)^{|\mathbf{i}|} d^\dagger_{\mathbf{i},yz,\sigma} d_{\mathbf{i}+\hat{x}-\hat{y},xy,\sigma} + h.c.] \\
& - t_8 \sum_{\mathbf{i},\sigma} [(-1)^{|\mathbf{i}|} d^\dagger_{\mathbf{i},xy,\sigma} d_{\mathbf{i}+\hat{x}-\hat{y},yz,\sigma} + h.c.].
\end{aligned}
\tag{A.5}
$$

In the equations above, the operator $d^\dagger_{\mathbf{i},\alpha,\sigma}$ creates an electron at site $\mathbf{i}$ of the two-dimensional lattice of irons. The orbital index is $\alpha = xz$, $yz$, or $xy$, and the $z$-axis spin projection is $\sigma$. The chemical potential used to regulate the electronic density is $\mu$. The symbols $\hat{x}$ and $\hat{y}$ denote vectors along the axes that join NN atoms. The values of the hoppings $t_i$ are from Ref. [56] and they are reproduced in Table A.1, including also the value of the energy splitting $\Delta_{xy}$.

**Table A.1:** Values of the parameters that appear in the tight-binding portion of the three-orbital model Eqs.(A.3) to (A.5). The overall energy unit is electron volts.

| $t_1$ | $t_2$ | $t_3$ | $t_4$ | $t_5$ | $t_6$ | $t_7$ | $t_8$ | $\Delta_{xy}$ |
|------|------|------|-------|------|------|------|------|-------------|
| 0.02 | 0.06 | 0.03 | −0.01 | 0.2 | 0.3 | −0.2 | 0.1 | 0.4 |

The remaining terms of the Hamiltonian have been briefly discussed in Ch. 2. The symbols $\langle\rangle$ denote NN while $\langle\langle\rangle\rangle$ denote NNN sums. The rest of the notation is standard.

$$H_{\text{Hund}} = -J_{\text{H}} \sum_{\mathbf{i},\alpha} \mathbf{S_i} \cdot \mathbf{s_{i,\alpha}}, \tag{A.6}$$

$$H_{\text{Heis}} = J_{\text{NN}} \sum_{\langle\mathbf{ij}\rangle} \mathbf{S_i} \cdot \mathbf{S_j} + J_{\text{NNN}} \sum_{\langle\langle\mathbf{im}\rangle\rangle} \mathbf{S_i} \cdot \mathbf{S_m}, \tag{A.7}$$

$$\Phi_{\mathbf{i}} = n_{\mathbf{i},xz} - n_{\mathbf{i},yz} \tag{A.8}$$

$$\Psi_{\mathbf{i}} = \sum_{\pm} (\mathbf{S_i} \cdot \mathbf{S_{i\pm y}} - \mathbf{S_i} \cdot \mathbf{S_{i\pm x}})/2 \tag{A.9}$$

$$H_{\text{SLO}} = -g_{66} \sum_{\mathbf{i}} \Psi_{\mathbf{i}} \epsilon_{66}(\mathbf{i}), \tag{A.10}$$

$$H_{\text{OLO}} = -\lambda_{66} \sum_{\mathbf{i}} \Phi_{\mathbf{i}} \epsilon_{66}(\mathbf{i}), \tag{A.11}$$

$$
\begin{aligned}
H_{\text{Stiff}} = \frac{1}{2} k \sum_{\mathbf{i}} \sum_{\nu=1}^{4} (|\mathbf{R}_{Fe-As}^{\mathbf{i}\nu}| - R_0)^2 + \\
+ k' \sum_{<\mathbf{ij}>} [(\frac{a_0}{R_{Fe-Fe}^{\mathbf{ij}}})^{12} - 2(\frac{a_0}{R_{Fe-Fe}^{\mathbf{ij}}})^6].
\end{aligned}
\tag{A.12}
$$

The $\mathcal{O}_{rth}$ strain $\epsilon_{66}(\mathbf{i})$ is defined as:

$$\epsilon_{66}(\mathbf{i}) = \frac{1}{4\sqrt{2}} \sum_{\nu=1}^{4} (|\delta_{\mathbf{i},\nu}^y| - |\delta_{\mathbf{i},\nu}^x|), \tag{A.13}$$

where $\delta_{\mathbf{i},\nu}^x(\delta_{\mathbf{i},\nu}^y)$ is the component along $x$ ($y$) of the distance between the Fe atom at site $\mathbf{i}$ of the lattice and one of its four neighboring As atoms that are labeled by the index

$\nu = 1, 2, 3, 4$. For more details of the notation used see Ref. [79], where the technical aspects on how to simulate an orthorhombic distortion can also be found.

# Appendix B

# Ginzburg-Landau Phenomenological Approach

In this section, the Monte Carlo data gathered for the spin-fermion model will be described via a phenomenological Ginzburg-Landau (GL) approach [179] to provide a more qualitative description of those numerical results. More specifically, the free energy $F$ of the spin-fermion model will be (approximately) written in terms of the spin-nematic order parameter $\Psi$, the orbital-nematic order parameter $\Phi$, and the orthorhombic strain $\epsilon_{66}$, as in GL descriptions. In previous literature a single nematic order parameter was considered without separating its magnetic and orbital character [10, 35, 67]. In addition, it was necessary to formulate assumptions about the order of the nematic and structural transitions. In our case, the MC results in this and previous publications are used as guidance to address this matter at the free energy level. More specifically, a second order magnetic transition was previously reported for the purely electronic system [61]. Thus, the spin-nematic portion of $F$ should display a free energy with a second order phase transition.

With regards to the terms involving $\epsilon_{66}$, the MC results of Ref. [79] showed that the coupling of the spin-nematic order parameter to the lattice leads to a weak first order (or very sharp second order) nematic and structural transition. Naively, this implies that the order $\epsilon_{66}^4$ term should have a negative coefficient. However, since in our numerical simulations a Lennard-Jones potential is used for the elastic term, then the sign of the quartic term is fixed and positive. Considering that the $\epsilon_{66}$ displacements are very small and the transition

is weakly first order at best, then just the harmonic (second order) approximation should be sufficient for $\epsilon_{66}$.

After all these considerations, the free energy is given by:

$$F = \frac{a}{2}\Psi^2 + \frac{b}{4}\Psi^4 + \frac{c}{2}\epsilon_{66}^2 + \frac{e}{2}\Phi^2 + \frac{f}{4}\Phi^4 \tag{B.1}$$

$$- \tilde{g}_{66}\Psi\epsilon_{66} - \tilde{\lambda}_{66}\Phi\epsilon_{66} - h\epsilon_{66}, \tag{B.2}$$

where $a$, $b$, $c$, $e$, and $f$ are the coefficients of the many terms of the three order parameters, while $\tilde{g}_{66}$ and $\tilde{\lambda}_{66}$ are the coupling constants of the lattice with the spin and orbital degrees of freedom, as described in Ch. 2. Since this and previous MC studies [61, 79] showed that there is no long-range orbital order in the ground state of the spin-fermion model, at least in the range of couplings investigated, then a positive quartic term is used for this order parameter. The parameter $h$ denotes an external stress, as explained in Ref. [67]. Note that in principle another term, and associated coupling constant, $\tilde{\alpha}\Psi\Phi$ should be included in $F$. This term will affect the orbital susceptibility and its effects will be described at the end of this Appendix.

As explained in Ch. 2, our MC results indicate that the leading order parameter guiding the results is the spin-nematic $\Psi$. Thus, it is reasonable to assume that only the coefficient $a$ depends on temperature as $a = a_0(T - T^*)$, while other parameters, such as $c = c_0$ (the uncoupled shear elastic modulus) and $e = e_0$, are approximately temperature independent.

For the special case $\tilde{g}_{66} = \tilde{\lambda}_{66} = 0$ the critical temperature $T^*$ for the magnetic transition can be obtained by setting to zero the derivative of $F$ with respect to $\Psi$:

$$\frac{\partial F}{\partial \Psi} = a\Psi + b\Psi^3 = 0. \tag{B.3}$$

Then, for $T \leq T^*$ the order parameter is given by

$$\Psi = \sqrt{\frac{a_0}{b}(T^* - T)}. \tag{B.4}$$

The equation above is valid only when $\Psi$ is small, i.e. close to the transition temperature from below. Additional terms in the free energy would be needed as $T \to 0$ since in that limit $|\Psi| = 2$.

Now consider the case when $\tilde{g}_{66}$ is nonzero, still keeping $\tilde{\lambda}_{66} = 0$. Setting to zero the derivative of $F$ with respect to $\Psi$ and $\epsilon_{66}$ leads to (for $h = 0$):

$$\frac{\partial F}{\partial \epsilon_{66}} = c_0 \epsilon_{66} - \tilde{g}_{66} \Psi = 0, \tag{B.5}$$

$$\frac{\partial F}{\partial \Psi} = a\Psi + b\Psi^3 - \tilde{g}_{66}\epsilon_{66} = 0. \tag{B.6}$$

From Eq.(B.5),

$$\Psi = \frac{c_0}{\tilde{g}_{66}}\epsilon_{66}, \tag{B.7}$$

which reproduces the linear relation obtained numerically before, see Fig. 2.2(b), with a slope now explicitly given in terms of $\tilde{g}_{66}$ and a constant that now can be identified with the bare shear elastic modulus $c_0$.

Solving for $\epsilon_{66}$ in Eq.(B.6) and introducing the result in Eq.(B.5) leads to:

$$\left(a - \frac{\tilde{g}_{66}^2}{c_0}\right)\Psi + b\Psi^3 = 0, \tag{B.8}$$

where it is clear that $a$ becomes renormalized due to the coupling to the lattice. The transition now occurs at a renormalized temperature $T_S$ that satisfies:

$$a_0(T - T_S) = a - \frac{\tilde{g}_{66}^2}{c_0} = a_0(T - T^*) - \frac{\tilde{g}_{66}^2}{c_0}. \tag{B.9}$$

From the expression above, it can be shown that the new nematic transition occurs at

$$T_S = T^* + \frac{\tilde{g}_{66}^2}{a_0 c_0}, \tag{B.10}$$

and clearly $T_S > T^*$. Note that Eq.(B.10) has been obtained in previous GL analysis, but in those studies a generic nematic coupling appeared in the numerator of the second term while here, more specifically, we identify $\tilde{g}_{66}$ with the spin-nematic coupling to the lattice.

Reciprocally, solving for $\Psi$ in Eq.(B.5) and introducing the result in Eq.(B.6) leads to:

$$\frac{a}{\tilde{g}_{66}}[(c_0 - \frac{\tilde{g}_{66}^2}{a})\epsilon_{66} + \frac{bc_0^3}{\tilde{g}_{66}^2 a}\epsilon_{66}^3] = 0, \tag{B.11}$$

where, due to the coupling to the lattice, now the shear constant is renormalized and an effective quartic term is generated for the lattice free energy. The effective shear elastic modulus $c_{66}$ becomes temperature dependent and it is given by:

$$c_{66} = c_0 - \frac{\tilde{g}_{66}^2}{a_0(T - T^*)}, \tag{B.12}$$

that vanishes at $T = T_S$. Thus, the structural transition occurs at the same critical temperature $T_S$ of the nematic transition.

To obtain the spin-nematic susceptibility, the second derivative of $F$ with respect to $\Psi$ and $h$ is set to zero:

$$\frac{\partial^2 F}{\partial h \partial \Psi} = a\frac{\partial \Psi}{\partial h} + 3b\Psi^2\frac{\partial \Psi}{\partial h} - \tilde{g}_{66}\frac{\partial \epsilon_{66}}{\partial h} = 0, \tag{B.13}$$

and then

$$\chi_s = \frac{\partial \Psi}{\partial \epsilon_{66}} = \frac{\frac{\partial \Psi}{\partial h}}{\frac{\partial \epsilon_{66}}{\partial h}} = \frac{\tilde{g}_{66}}{a + 3b\Psi^2} = \frac{\tilde{g}_{66}}{a_0(T - T^*) + 3b\Psi^2}. \tag{B.14}$$

This is an important equation that was used in Ch. 2 to rationalize the MC numerical results. In the range $T \geq T_S$, i.e. when $\Psi = 0$, the spin-nematic susceptibility clearly follows a Curie-Weiss behavior. In practice, it has been observed that $b = a_0 T_S$ to a good approximation.

Consider now the case when the orbital-lattice coupling $\tilde{\lambda}$ is nonzero as well. Now

$$\frac{\partial F}{\partial \epsilon_{66}} = c_0\epsilon_{66} - \tilde{g}_{66}\Psi - \tilde{\lambda}_{66}\Phi = 0, \tag{B.15}$$

$$\frac{\partial F}{\partial \Psi} = a\Psi + b\Psi^3 - \tilde{g}_{66}\epsilon_{66} = 0, \tag{B.16}$$

and a new equation is available:

$$\frac{\partial F}{\partial \Phi} = e_0\Phi + f\Phi^3 - \tilde{\lambda}_{66}\epsilon_{66} = 0. \tag{B.17}$$

Solving for $\Psi$ in Eq.(B.15) leads to:

$$\Psi = \frac{c_0 \epsilon_{66} - \tilde{\lambda}_{66} \Phi}{\tilde{g}_{66}}, \tag{B.18}$$

while solving for $\epsilon_{66}$ in Eq.(B.16) leads to:

$$\epsilon_{66} = \frac{a\Psi + b\Psi^3}{\tilde{g}_{66}}. \tag{B.19}$$

Introducing Eq.(B.19) into Eq.(B.18), $\Phi$ is obtained in terms of $\Psi$ as follows:

$$\Phi = (\frac{c_0}{\tilde{\lambda}_{66}\tilde{g}_{66}})[(a - \frac{\tilde{g}_{66}^2}{c_0})\Psi + b\Psi^3]. \tag{B.20}$$

Introducing Eqs.(B.19) and (B.20) into Eq.(B.17) a renormalized equation for $\Psi$ is obtained:

$$[\frac{e_0 c_0}{\tilde{\lambda}_{66}\tilde{g}_{66}}(a - \frac{\tilde{g}_{66}^2}{c_0}) - \frac{\tilde{\lambda}_{66}a}{\tilde{g}_{66}}]\Psi + [\frac{e_0 c_0}{\tilde{\lambda}_{66}\tilde{g}_{66}}b - \frac{\tilde{\lambda}_{66}b}{\tilde{g}_{66}} + \frac{f c_0^3}{\tilde{\lambda}_{66}^3 \tilde{g}_{66}^3}(a - \frac{\tilde{g}_{66}^2}{c_0})^3]\Psi^3 = 0. \tag{B.21}$$

Then, at $T = T_S$ the effective coefficient of the linear term in $\Psi$ provides the new transition temperature:

$$a_0(T - T_S) = a - \frac{e_0 \tilde{g}_{66}^2}{e_0 c_0 - \tilde{\lambda}_{66}^2}. \tag{B.22}$$

Using that $a = a_0(T - T^*)$, the dependence of the critical temperature with the two coupling constants $\tilde{g}$ and $\tilde{\lambda}$ can be obtained:

$$T_S = T^* + \frac{\tilde{g}_{66}^2}{a_0 c_0 (1 - \frac{\tilde{\lambda}_{66}^2}{c_0 e_0})}. \tag{B.23}$$

This is another interesting formula that nicely describes the MC results, as shown in Ch. 2. Equation(B.23) is a novel result that shows that $T_S$ depends in a different way on the spin-lattice ($\tilde{g}_{66}$) and the orbital-lattice ($\tilde{\lambda}_{66}$) couplings. Moreover, an effective $\tilde{\lambda}_{66}$-dependent elastic modulus $c(\tilde{\lambda}_{66})$ can be defined as

$$c(\tilde{\lambda}_{66}) = c_0 - \frac{\tilde{\lambda}_{66}^2}{e_0}. \tag{B.24}$$

In addition, the effective shear elastic modulus is now given by

$$c_{66} = c_0 - \frac{\tilde{\lambda}_{66}^2}{e_0} - \frac{\tilde{g}_{66}^2}{a_0(T - T^*)},$$ (B.25)

which vanishes at the $T_S$ given by Eq.(B.23).

The spin-nematic susceptibility is still given by Eq.(B.14) with the dependence on $\tilde{\lambda}_{66}$ embedded in the actual values of $\Psi$. The orbital-nematic susceptibility is obtained from Eq.(B.17) as

$$\frac{\partial^2 F}{\partial h \partial \Phi} = (e_0 + 3f\Phi^2)\frac{\partial \Phi}{\partial h} - \tilde{\lambda}_{66}\frac{\partial \epsilon_{66}}{\partial h} = 0.$$ (B.26)

In the absence of an explicit coupling $\tilde{\alpha}$ between the spin-nematic and orbital order parameters, then the orbital-nematic susceptibility becomes:

$$\chi_o = \frac{\partial \Phi}{\partial \epsilon_{66}} = \frac{\frac{\partial \Phi}{\partial h}}{\frac{\partial \epsilon_{66}}{\partial h}} = \frac{\tilde{\lambda}_{66}}{e_0 + 3f\Phi^2}.$$ (B.27)

If a term of the form $\tilde{\alpha}\Psi\Phi$ is added to the free energy, as discussed in Ch. 2, the expressions for the susceptibilities can be obtained for $T \geq T_S$. The orbital susceptibility now displays Curie-Weiss behavior:

$$\chi_o = \frac{\tilde{\lambda}_{66}}{e_0} + \frac{\tilde{\alpha}(\tilde{g}_{66}e_0 + \tilde{\lambda}_{66}\tilde{\alpha})}{a_0 e_0^2[T - (T^* + \frac{\tilde{\alpha}^2}{a_0 e_0})]},$$ (B.28)

while the spin-nematic susceptibility becomes:

$$\chi_s = \frac{\tilde{g}_{66}e_0 + \tilde{\lambda}_{66}\tilde{\alpha}}{a_0 e_0[T - (T^* + \frac{\tilde{\alpha}^2}{a_0 e_0})]},$$ (B.29)

and the structural transition temperature is given by

$$T_S = T^* + \frac{\tilde{\alpha}^2}{a_0 e_0} + \frac{(\tilde{\lambda}_{66}\tilde{\alpha} + e_0\tilde{g}_{66})^2}{a_0 e_0 c_0^2(1 - \frac{\tilde{\lambda}_{66}^2}{e_0 c_0})}.$$ (B.30)

# Appendix C

# Partial and Total Derivatives at $T_S$

The partial derivative in the definition of $\chi_s$ is at constant temperature varying $\epsilon_{66}$ and it is evaluated at equilibrium $\epsilon_{66} = \epsilon_0$. The slopes of the green and blue curves of Fig. 2.2(b) provide this derivative. On the other hand, the results of Fig. 2.2(b) in equilibrium (slope of the red points curve) provide the full derivative $\frac{d\Psi}{d\epsilon_{66}}$. Since $\epsilon_{66}=\epsilon_{66}(T)$, their relation is

$$\frac{d\Psi}{d\epsilon_{66}} = \frac{\partial\Psi}{\partial\epsilon_{66}}|_{\epsilon_0} + \frac{\partial\Psi}{\partial T}|_{\epsilon_0}\frac{\partial T}{\partial\epsilon_{66}}|_{\epsilon_0} = \chi_s + \frac{\frac{\partial\Psi}{\partial T}|_{\epsilon_0}}{\frac{\partial\epsilon_{66}}{\partial T}|_{\epsilon_0}}, \tag{C.1}$$

where $\frac{\partial\Psi}{\partial T}$ is performed at constant $\epsilon_{66}$ and $\frac{\partial\epsilon_{66}}{\partial T}|_{\epsilon_0}$ is performed at constant $\Psi$. In general, the partial and total derivatives of $\Psi$ with respect to $\epsilon$ can differ from one another. However, at small $\tilde{\lambda}_{66}$ the structural transition is weakly first order [79] (or a very sharp second order) and then when $T \approx T_S$ the lattice distortion $\epsilon_{66}$ rapidly jumps from 0 to a finite value. This means that $\frac{\partial\epsilon_{66}}{\partial T}|_{\epsilon_0}$ is very large while $\frac{\partial\Psi}{\partial T}|_{\epsilon_0}$ remains finite since it is performed at fix $\epsilon$. Thus, at $T \approx T_S$, the partial and total derivatives are almost the same. This can be seen in Fig. 2.2(b) of Ch. 2 where the slopes of the green curves at $\epsilon_{66} = 0$, when they cross the equilibrium line, are smaller than the equilibrium slope $K$ but increase with decreasing temperature until it becomes equal to $K$ at $T = T_S$ (red line). The slopes of the blue curves at the finite value of $\epsilon_{66}$ where they cross the equilibrium line are smaller than $K$ and decrease with decreasing temperature.
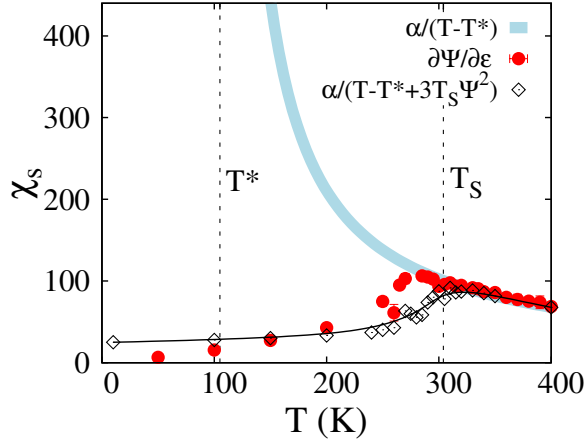
**Figure C.1:** Spin-nematic susceptibility $\chi_s$ vs. temperature $T$ (red circles) obtained from Fig. D.1(b) (at $\tilde{g}_{66}=0.16$ and $\tilde{\lambda}_{66}=0.84$). The standard MC technique on an $8\times8$ cluster with PBC was employed (involving ED of the fermions at every MC step). Also shown are two GL fits, as also employed in Fig. 2.4. The blue (thick) line indicates a divergence at a temperature $T^*$ (lower than $T_S$) characteristic of the electronic sector alone. In the range $T \leq T_S$, the lattice follows the electronic behavior. The black (thin) line and black tilted square points are a fit including the $3T_S\Psi^2$ correction (see text in the previous section of this Suppl. Material). The fitting parameters are $T^* = 105$ K and $T_S = 304$ K. The actual Néel temperature for $\tilde{g}_{66}=0.16$ and $\tilde{\lambda}_{66}=0.84$ is not shown.

# Appendix D

# Spin-nematic Susceptibility at Large $\tilde{\lambda}_{66}$

To investigate in more detail the potential role of orbital order in the spin-nematic susceptibility, simulations were repeated for a robust $\tilde{\lambda}_{66} = 0.84$, keeping the other electron-lattice coupling fixed as $\tilde{g}_{66} = 0.16$. Results are shown in Fig. C.1. The increase of $\tilde{\lambda}_{66}$ substantially increases $T_S$, which is to be expected since now the electron-lattice coupling is larger [79]. However, above $T_S$ still the results can be well fit by a Curie-Weiss law, with a divergence at $T^*$ which is the critical temperature of the purely electronic system, as described in Ch. 2. Even the coefficient $a_0$ in the fit is almost identical to that of the case $\tilde{\lambda}_{66} = 0.12$, in Fig. 2.4. The second fit, with the $3T_S\Psi^2$ correction, is still reasonable. In summary, as long as $\tilde{\lambda}_{66}$ is not increased to such large values that the low-temperature ground state is drastically altered, the computational results can still be analyzed via the GL formalism outlined here and in Ch. 2, with a $T^*$ that originates in the $(\pi, 0)$ magnetic transition of the purely electronic sector.

For completeness, the plots analog to those of Fig. 4.2 but in the present case of $\tilde{\lambda}_{66} = 0.84$ are provided in Fig. D.1.
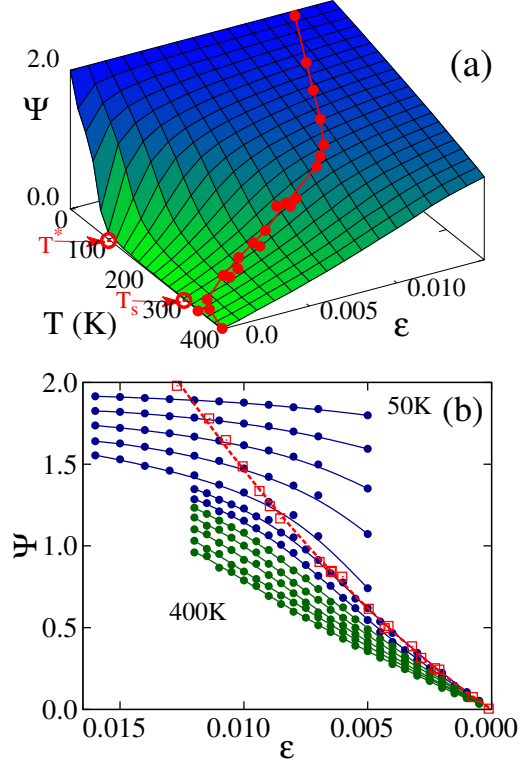
**Figure D.1:** Spin-nematic order parameter from the MC simulations, at $\tilde{g}_{66}$=0.16 and $\tilde{\lambda}_{66}$=0.84. (a) $\Psi$ vs. $T$ and $\epsilon_{66}$, measured at a fixed lattice distortion $\epsilon_{66}$ for each temperature (restricted MC). Shown are the $T^*$ temperature (see text) and $T_S$. Results shown are for an 8×8 cluster with TCA+TBC, but PBC 8×8 clusters with ED give similar results. Red points are the equilibrium values using unrestricted MC with ED and PBC 8×8 clusters. (b) MC results illustrating the relation between $\Psi$ and $\epsilon_{66}$ in unrestricted MC (red) and the restricted MC curves (green/blue), parametric with temperature. Results are obtained with ED/PBC 8×8 clusters. Note that $\Psi$ vs. $\epsilon_{66}$ (red squares) is no longer linear which is expected because Eq.(B.7) is valid only for $\tilde{\lambda}_{66} = 0$ (and approximately valid for small $\tilde{\lambda}_{66}$).

# Appendix E

# Definition and Calculations of Lattice Displacement and Magnetic and Structural Order Parameters

The lattice variables $\delta_{\mathbf{i},\nu} = (\delta_{\mathbf{i},\nu}^x, \delta_{\mathbf{i},\nu}^y)$, with $\nu$ ranging from 1 to 4, that enter in the definition of $\epsilon_{66}$ and $\epsilon_{12}$, the orthorhombic and monoclinic lattice distortions respectively, denote the distances between an Fe atom at site $\mathbf{i}$ (filled circles in Fig. E.1) and one of its four neighboring As or Te atoms (open circles in the figure and labeled by the index $\nu$). The As/Te atoms are allowed to move locally from their equilibrium position, but only along the directions $x$ and $y$ (the $z$ coordinate does not participate in the planar lattice distortions addressed here).

The Hamiltonian $H_{\mathrm{SF}}$ defined in Sect. 4.2 was studied using a Monte Carlo method [61, 82] applied to *(i)* the localized spin degrees of freedom $\mathbf{S_i}$ assumed classical, *(ii)* the atomic displacements $(\delta_{\mathbf{i},\nu}^x, \delta_{\mathbf{i},\nu}^y)$ that determine the local orthorhombic or monoclinic lattice distortions $\epsilon_{66}(\mathbf{i})$ [79] and $\epsilon_{12}(\mathbf{i})$ defined in Eq. 4.5, *(iii)* the global orthorhombic distortion $(r_x, r_y)$, and *(iv)* the global monoclinic distortion $\theta$. As already explained, the As/Te atoms are allowed to move from their equilibrium positions on the $x - y$ plane but the Fe atoms can only move globally in two ways: (i) via a global orthorhombic distortion characterized by a global displacement $(r_x, r_y)$ from the equilibrium position $(x_i^{(0)}, y_i^{(0)})$ of each Fe atom, with $r_\alpha = 1 + \Delta_\alpha$ ($\Delta_\alpha \ll 1$) and $\alpha = x$ or $y$ [see panel (c) of Fig. 4.2]; (ii) via the angle between two orthogonal Fe-Fe bonds which is allowed to change globally to $90^o + \theta$ with the
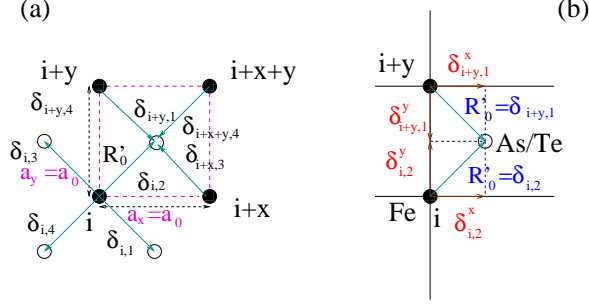
**Figure E.1:** (a) Schematic representation of the equilibrium position of the Fe-Te/As lattice (projected on the $x$-$y$ plane). Four Fe atoms are indicated with filled circles and labeled by their site index $\mathbf{i}$. The open circles indicate the projection of the equilibrium position of the As/Te atoms on the $x$-$y$ plane. The distances between an Fe atom at site $\mathbf{i}$ and its four neighboring As/Te atoms are indicated by $\delta_{\mathbf{i},\nu}$ with $\nu$ running from 1 to 4 (turquoise arrows). In equilibrium $\delta_{\mathbf{i},\nu} = \sqrt{2}a_0/2$. The dashed lines indicate $a_x = a_y = a_0$, the equilibrium distance between neighboring irons. (b) Sketch representing the variables $\delta_{\mathbf{i},\nu}^x$ and $\delta_{\mathbf{i},\nu}^y$ (brown arrows) for labels $(\mathbf{i}, 2)$ and $(\mathbf{i} + \mathbf{y}, 1)$ in the equilibrium configuration. For an illustration of the non-equilibrium $\delta_{\mathbf{i},\nu}$ see [79].

four angles in the monoclinic plaquette adding to $360^o$ so that the following angle in the plaquette becomes $90^o - \theta$, with $\theta$ a small angle [see panel (d) of Fig. 4.2]. After the global distortion the new position of the Fe atom is given by

$$
\begin{cases}
x_i = x_i^{(0)} r_x \cos\theta - y_i^{(0)} r_y \sin\theta \\
y_i = -x_i^{(0)} r_x \sin\theta + y_i^{(0)} r_y \cos\theta.
\end{cases}
\tag{E.1}
$$

When an orthorhombic distortion is stabilized, the variables $\delta_{\mathbf{i},\nu}^s$ satisfy the constrain

$$
2Na_s = \sum_{\mathbf{i}=1}^{N} \sum_{\nu=1}^{4} |\delta_{\mathbf{i},\nu}^s|,
\tag{E.2}
$$

where $N$ is the number of Fe sites, $s = x, y$, and $a_s = a_0 r_s$ is the constant Fe-Fe distance along the $s$ direction which is equal to $a_0$ in the undistorted tetragonal phase as shown in panel (c) of Fig. 4.2). The orthorhombic distortion order parameter $\delta_O$ is then given by

$$
\delta_O = \frac{|a_x - a_y|}{a_x + a_y} = \frac{a_0|r_x - r_y|}{a_0(r_x + r_y)}.
\tag{E.3}
$$

Since $r_s = 1 + \Delta_s$ and $s = x,\, y$, then

$$\delta_O = \frac{|1 + \Delta_x - (1 + \Delta_y)|}{1 + \Delta_x + 1 + \Delta_y} \approx \frac{1}{2}|\Delta_x - \Delta_y|. \tag{E.4}$$

On the other hand, when a monoclinic distortion is stabilized the constraint satisfied by $\delta^s_{\mathbf{i},\nu}$ is given by

$$2N d_{x+y} = \sum_{\mathbf{i}=1}^{N}(|\delta_{\mathbf{i},4}| + |\delta_{\mathbf{i},2}|), \tag{E.5}$$

and

$$2N d_{x-y} = \sum_{\mathbf{i}=1}^{N}(|\delta_{\mathbf{i},3}| + |\delta_{\mathbf{i},1}|), \tag{E.6}$$

where $d_\mu$ is the length of the plaquette's diagonal along the $\mu$ direction of the plaquette formed by four Fe atoms. In the tetragonal phase $d_\mu = \sqrt{2}a_0$ while in the monoclinic phase $d_\mu = \sqrt{2}a_0\sqrt{1 - \cos(90^o \pm \theta)}$ with the plus (minus) sign for $\mu = x - y$ ($x + y$) [see panel (d) of Fig. 4.2]. The monoclinic distortion order parameter $\delta_M$ is then given by

$$\delta_M = \frac{|d_{x+y} - d_{x-y}|}{d_{x+y} + d_{x-y}} =$$

$$\frac{\sqrt{2}a_0|(1 - \sin\theta)^{1/2} - (1 + \sin\theta)^{1/2}|}{\sqrt{2}a_0((1 - \sin\theta)^{1/2} + (1 + \sin\theta)^{1/2})} \approx \frac{\theta}{2}. \tag{E.7}$$

In summary, Monte Carlo simulations are performed on the values for the lattice variables $r_x$, $r_y$, $\theta$, and $\delta^s_{\mathbf{i},\nu}$, and also on the localized spin variables $\mathbf{S_i}$.

For each fixed Monte Carlo configuration of spins, atomic positions and global distortions, the remaining quantum fermionic Hamiltonian is diagonalized. The simulations were performed varying the temperature $T$ and the spin-lattice dimensionless couplings $\tilde{g}_{66}$ and $\tilde{g}_{12}$. The latter are defined by $\tilde{g}_{66} = \frac{2g_{66}}{\sqrt{kW}}$ and $\tilde{g}_{12} = \frac{2g_{12}}{\sqrt{kW}}$ where $W = 3$ eV is the bandwidth of the tight-binding portion of the Hamiltonian and $k$ is a constant that appears in $H_{\text{Stiff}}$ (for details see [79]). The range of values explored for these dimensionless coupling constants was chosen so that the orthorhombic and monoclinic distortions (also dimensionless defined) agree with the experimental values that range from 0.003 to 0.007 [41, 137, 145].

The fermionic exact diagonalization technique results can be obtained comfortably only on up to $8 \times 8$ lattices which is the cluster size used in this work. However, twisted boundary conditions were also used [89] in the evaluation of the resistivities and Fermi surfaces (FS), effectively increasing the lattice size as explained in early efforts [79]. Most couplings were fixed to values used successfully in previous investigations [61] for simplicity: $J_H$=0.1 eV, $J_{NN}$=0.012 eV, and $J_{NNN}$=0.008 eV. However, results for $J_H$=0.2 eV and $J_{NN}=J_{NNN}=0$ were also discussed in Sec. 4.3. As explained there, qualitatively our conclusions do not change whether the Heisenberg interactions between the localized spins are or not included in the study.

In the Monte Carlo simulations typically 5,000 MC lattice sweeps were used for thermalization and 10,000 to 25,000 for measurements, at each temperature and parameter values investigated. In addition to the $B_{2g}$ order parameter, the magnetic transition was also determined from the magnetic susceptibility defined as

$$\chi_{S(k_x,k_y)} = N\beta\langle S(k_x, k_y) - \langle S(k_x, k_y)\rangle\rangle^2, \tag{E.8}$$

where $\beta = 1/k_B T$, $N$ is the number of lattice sites, and $S(k_x, k_y)$ is the magnetic structure factor at wavevector $(k_x, k_y)$ obtained via the Fourier transform of the real-space spin-spin correlations measured in the MC simulations. To study the collinear [bicollinear] AFM state $(k_x, k_y)$ was set to $(\pi, 0)$ $[(\pi/2, -\pi/2)]$.

Besides the lattice order parameter $\delta_O$ given in Eq. E.3, the orthorhombic structural transition was determined from the behavior of the lattice susceptibility defined as

$$\chi_{\delta_O} = N\beta\langle \delta_O - \langle \delta_O\rangle\rangle^2. \tag{E.9}$$

Reciprocally, the monoclinic structural transition was studied via its order parameter, i.e. the monoclinic distortion $\delta_M$ given in Eq. E.7, and also through the lattice susceptibility defined as

$$\chi_{\delta_M} = N\beta\langle \delta_M - \langle \delta_M\rangle\rangle^2. \tag{E.10}$$

# Appendix F

# Resistivity Calculation

The method used in Sec. 4.3 to calculate the resistivity is based on the computational implementation of the Kubo formula for DC conductance described in Ref. [180]. According to Eq. 8 in Ref. [180] the conductance $G$ is given by:

$$
G_{\vec{\nu}} = \lim_{\omega \to 0} \frac{< \hat{I}_{\vec{\nu}} >}{V} =
$$
$$
- e^2 \hbar \pi \lim_{\omega \to 0} \sum_{\alpha\beta} | < \psi_\alpha | \hat{v}_{\vec{\nu}} | \psi_\beta > |^2 \frac{f_\alpha - f_\beta}{\epsilon_\alpha - \epsilon_\beta} \delta(\epsilon_\alpha - \epsilon_\beta - \hbar\omega), \quad \text{(F.1)}
$$

where $f_\alpha = (1 + e^{\beta(\epsilon_\alpha - \mu)})^{-1}$ is the Fermi distribution for each occupied eigenstate $|\psi_\alpha >$ and $\hat{v}_{\vec{\nu}}$ is the velocity operator whose definition in terms of the fermionic operators is provided below. The product of the last two factors in the conductance $G$ can be simplified using a Taylor expansion ($\Delta(\epsilon) = \epsilon_\alpha - \epsilon_\beta$):

$$
\lim_{\omega \to 0} \frac{f_\alpha - f_\beta}{\epsilon_\alpha - \epsilon_\beta} \delta(\epsilon_\alpha - \epsilon_\beta - \hbar\omega)
$$
$$
\approx \lim_{\Delta(\epsilon) \to 0} \frac{(1 + e^{\beta(\epsilon - \mu + \Delta(\epsilon))})^{-1} - (1 + e^{\beta(\epsilon - \mu)})^{-1}}{\Delta(\epsilon)}
$$
$$
= \frac{-\beta e^{\beta(\epsilon - \mu)}}{(1 + e^{\beta(\epsilon - \mu)})^2} \quad \text{(F.2)}
$$

The operators for the velocity ($\hat{v}_{\vec{\nu}}$) in different lattice directions ($\vec{\nu}$) are given by:

$$i\hbar\hat{v}_{\vec{x}} = -\sum_{\sigma,\alpha,\beta,\mathbf{i}} t_{\hat{x}}^{\alpha\beta} d_{\mathbf{i},\alpha,\sigma}^{\dagger} d_{\mathbf{i}+\hat{\mathbf{x}},\beta,\sigma} +$$

$$\frac{t_{\hat{x}+\hat{y}}^{\alpha\beta}}{\sqrt{2}} d_{\mathbf{i},\alpha,\sigma}^{\dagger} d_{\mathbf{i}+\hat{\mathbf{x}}+\hat{\mathbf{y}},\beta,\sigma} + \frac{t_{\hat{x}-\hat{y}}^{\alpha\beta}}{\sqrt{2}} d_{\mathbf{i},\alpha,\sigma}^{\dagger} d_{\mathbf{i}+\hat{\mathbf{x}}-\hat{\mathbf{y}},\beta,\sigma} - h.c \quad \text{(F.3)}$$

$$i\hbar\hat{v}_{\vec{y}} = -\sum_{\sigma,\alpha,\beta,\mathbf{i}} t_{\hat{y}}^{\alpha\beta} d_{\mathbf{i},\alpha,\sigma}^{\dagger} d_{\mathbf{i}+\hat{\mathbf{y}},\beta,\sigma} +$$

$$\frac{t_{-\hat{x}+\hat{y}}^{\alpha\beta}}{\sqrt{2}} d_{\mathbf{i},\alpha,\sigma}^{\dagger} d_{\mathbf{i}-\hat{\mathbf{x}}+\hat{\mathbf{y}},\beta,\sigma} + \frac{t_{\hat{x}+\hat{y}}^{\alpha\beta}}{\sqrt{2}} d_{\mathbf{i},\alpha,\sigma}^{\dagger} d_{\mathbf{i}+\hat{\mathbf{x}}+\hat{\mathbf{y}},\beta,\sigma} - h.c \quad \text{(F.4)}$$

$$i\hbar\hat{v}_{\vec{x}+\vec{y}} = -\sum_{\sigma,\alpha,\beta,\mathbf{i}} \frac{t_{\hat{y}}^{\alpha\beta}}{\sqrt{2}} d_{\mathbf{i},\alpha,\sigma}^{\dagger} d_{\mathbf{i}+\hat{\mathbf{y}},\beta,\sigma} +$$

$$t_{\hat{x}+\hat{y}}^{\alpha\beta} d_{\mathbf{i},\alpha,\sigma}^{\dagger} d_{\mathbf{i}+\hat{\mathbf{x}}+\hat{\mathbf{y}},\beta,\sigma} + \frac{t_{\hat{x}}^{\alpha\beta}}{\sqrt{2}} d_{\mathbf{i},\alpha,\sigma}^{\dagger} d_{\mathbf{i}+\hat{\mathbf{x}},\beta,\sigma} - h.c \quad \text{(F.5)}$$

$$i\hbar\hat{v}_{-\vec{x}+\vec{y}} = -\sum_{\sigma,\alpha,\beta,\mathbf{i}} \frac{t_{\hat{y}}^{\alpha\beta}}{\sqrt{2}} d_{\mathbf{i},\alpha,\sigma}^{\dagger} d_{\mathbf{i}+\hat{\mathbf{y}},\beta,\sigma} +$$

$$t_{-\hat{x}+\hat{y}}^{\alpha\beta} d_{\mathbf{i},\alpha,\sigma}^{\dagger} d_{\mathbf{i}-\hat{\mathbf{x}}+\hat{\mathbf{y}},\beta,\sigma} + \frac{t_{-\hat{x}}^{\alpha\beta}}{\sqrt{2}} d_{\mathbf{i},\alpha,\sigma}^{\dagger} d_{\mathbf{i}-\hat{\mathbf{x}},\beta,\sigma} - h.c \quad \text{(F.6)}$$

with the hoppings given by

$$t_{\hat{x}}^{\alpha\beta} = \begin{pmatrix} t_2 & 0 & t_7^* \\ 0 & t_1 & 0 \\ t_7^* & 0 & t_5 \end{pmatrix}$$

135

$$t_{\hat{y}}^{\alpha\beta} = \begin{pmatrix} t_1 & 0 & 0 \\ 0 & t_2 & t_7^* \\ 0 & t_7^* & t_5 \end{pmatrix}$$

$$t_{\hat{x}+\hat{y}}^{\alpha\beta} = \begin{pmatrix} t_3 & -t_4 & t_8^* \\ -t_4 & t_3 & t_8^* \\ -t_8^* & -t_8^* & t_6 \end{pmatrix}$$

$$t_{\hat{x}-\hat{y}}^{\alpha\beta} = \begin{pmatrix} t_3 & t_4 & t_8^* \\ t_4 & t_3 & -t_8^* \\ -t_8^* & t_8^* & t_6 \end{pmatrix}$$

$$t_{-\hat{x}+\hat{y}}^{\alpha\beta} = \begin{pmatrix} t_3 & t_4 & -t_8^* \\ t_4 & t_3 & t_8^* \\ t_8^* & -t_8^* & t_6 \end{pmatrix}$$

The parameters $t_i$ provided in Table A.1 are the tight-binding hoppings in the three-orbital model for pnictides from Ref. [56]. Notice that $t_7^* = (-1)^{i+j}t_7$ and $t_8^* = (-1)^{i+j}t_8$ due to the periodicity of the As atom's positions (where $i$ and $j$ are the $x$ and $y$ coordinates of lattice site $\mathbf{i}$, respectively). The resistivity anisotropy for the iron-pnictides occurs along the $\hat{x}$ and $\hat{y}$ directions while in the iron chalcogenides the $\hat{x}+\hat{y}$ and $-\hat{x}+\hat{y}$ directions need to be considered due to the $45^o$ relative rotation of the lattice axis. These are also the directions along which the magnetic order forms in the respective compounds (see Sec. 4.3).

In order to increase the accuracy of the calculation, Twisted Boundary Conditions (TBC) were implemented [61]. This multiplies the number of momenta in both the $\hat{x}$ and $\hat{y}$ directions from L $\rightarrow$ L x M through applying a phase $\Phi = \frac{2 \pi m}{M}$ with $m = 0, 1, ..., M - 1$, at the boundaries so that the hoppings at the boundaries are now given by $t_{TBC}^{\alpha\beta} = t^{\alpha\beta} e^{i\Phi}$.

The velocity matrix elements for each relevant directions $\vec{\nu}$ are evaluated using the Monte Carlo method described in the previous subsection. The directional resistance $R_{\vec{\nu}}$ is obtained by inverting the conductance $G_{\vec{\nu}}$.

# Appendix G

# Additional Phase Diagrams for the Hamiltonian Studied in Ch. 4

The phase diagram as a function of the couplings $\tilde{g}_{66}$ and $\tilde{g}_{12}$ at $T = 10$ K is presented in Fig. G.1 including Heisenberg couplings. It is important to remember that in the absence of spin-lattice couplings the SF model already develops a collinear AFM ground state due to the comparable NN and NNN hoppings in the tight-binding term of the Hamiltonian (and the concomitant NN and NNN Heisenberg interactions between the localized spins if included [61]). The coupling $\tilde{g}_{66}$ that couples the short-range $B_{1g}$ magnetic nematic operator to the orthorhombic distortion stabilizes a small orthorhombic distortion that increases monotonically with the value of this spin-lattice coupling, as indicated by the size of the inverted triangles in the figure. The blue circles indicate the concomitant presence of collinear $(\pi, 0)$ AFM order. The figure shows that, regardless of $\tilde{g}_{66}$, the coupling $\tilde{g}_{12}$, between the monoclinic lattice distortion and the $B_{2g}$ magnetic nematic operator, has to reach a finite value close to 0.25 to stabilize the bicollinear AFM state indicated by the red circles in the figure. The bicollinear magnetic order is accompanied by a monoclinic lattice distortion indicated by the triangles whose size increases monotonically with $\tilde{g}_{12}$.

It is interesting to observe that there is a region in the phase diagram Fig. G.1 where the monoclinic distortion is stabilized, but the magnetic order is neither collinear nor bicollinear. This is caused by the competition between $\tilde{g}_{12}$, that after inducing the monoclinic distortion induces the bicollinear magnetic order, and the NN and NNN Heisenberg couplings that
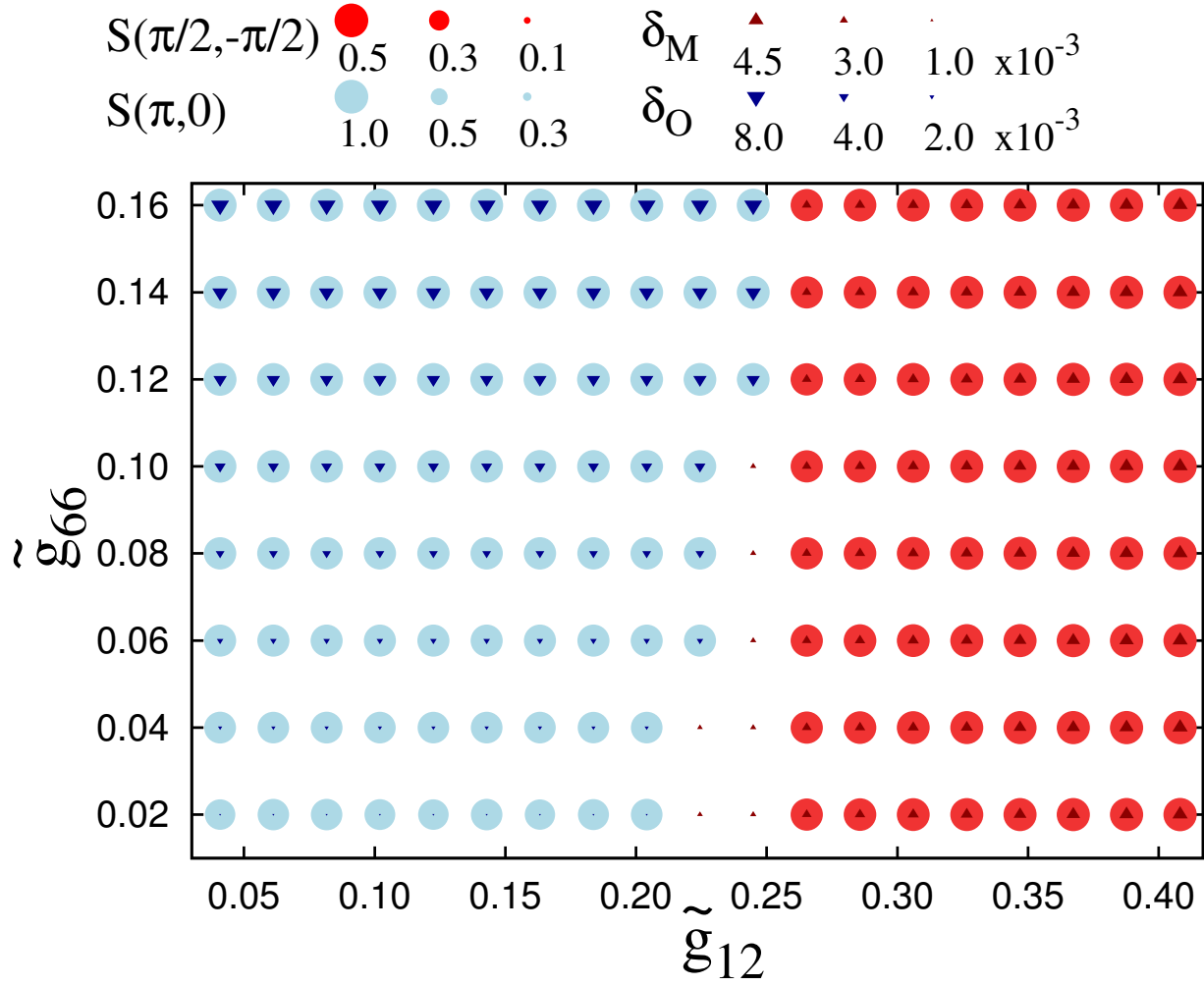
**Figure G.1:** Phase diagram at $T = 10$ K of the spin fermion model, including Heisenberg couplings with the values indicated in the Methods Section, varying the dimensionless couplings to the orthorhombic and monoclinic distortions. The size of the blue (red) circles is proportional to the strength of the collinear (bicollinear) AFM order. The size of the bottom side up (down) triangles is proportional to the magnitude of the orthorhombic (monoclinic) distortion. The actual scales used are shown at the top of the figure.

favor a collinear $(\pi, 0)$ magnetic state. Thus, $\tilde{g}_{12}$ is able to induce the lattice distortion before it clearly stabilizes the bicollinear magnetic order. The fact that the value of $\tilde{g}_{12}$ that stabilizes the bicollinear state is larger than the value of $\tilde{g}_{66}$ needed to obtain the experimentally observed magnitude of the orthorhombic distortion is also a result of the effect of the Heisenberg terms in the Hamiltonian that favor the collinear AFM state.
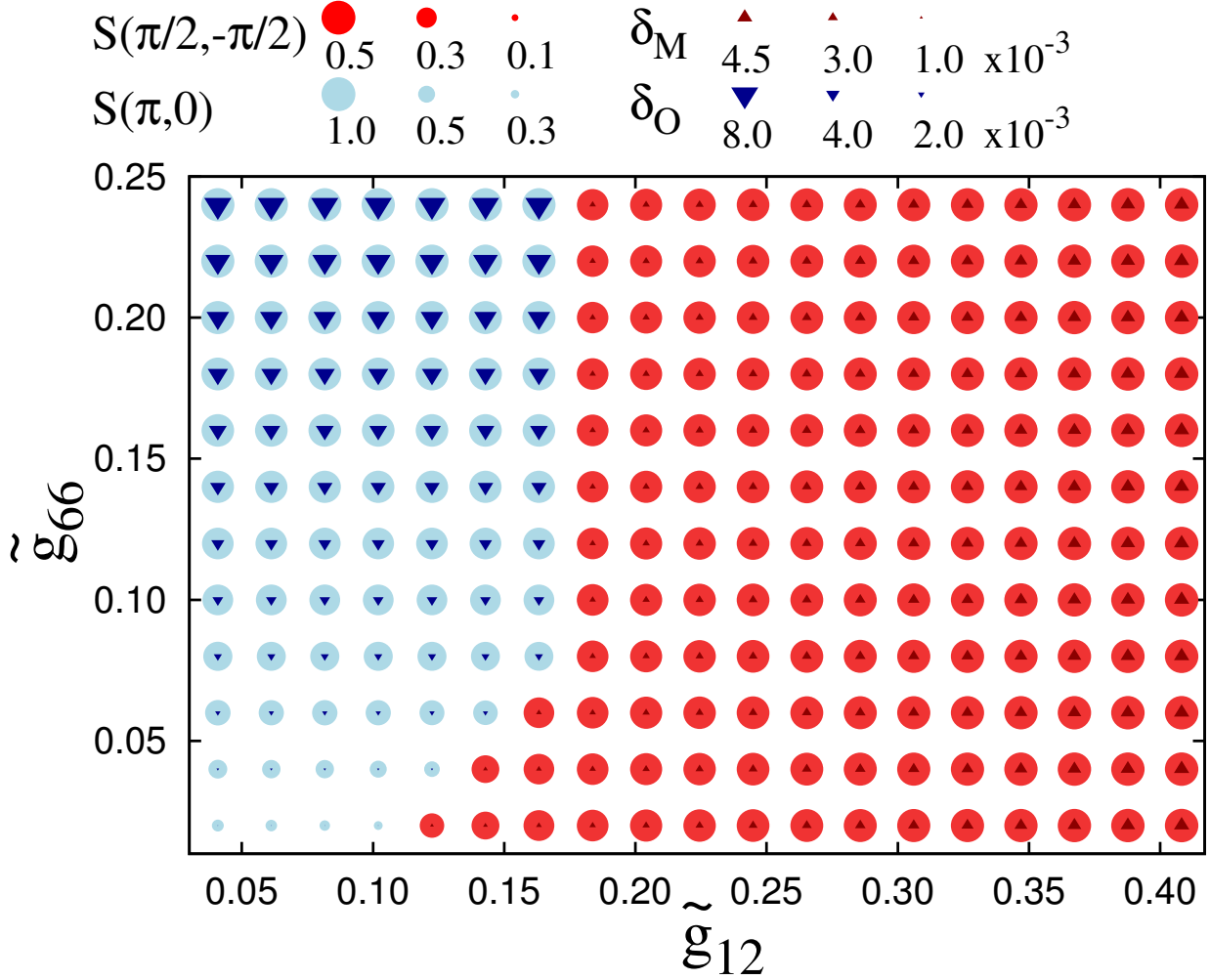


**Figure G.2:** Phase diagram at $T = 10$ K corresponding to the spin-fermion model for the case $J_{\mathrm{NNN}}{=}J_{\mathrm{NN}}{=}0$, varying the spin-lattice couplings that lead to the orthorhombic and monoclinic distortions. The size of the blue (red) circles is proportional to the strength of the collinear (bicollinear) AFM order, while the size of the bottom side up (down) triangles is proportional to the magnitude of the orthorhombic (monoclinic) distortion.

In Fig. G.2 we display the low-temperature phase diagram in the plane $\tilde{g}_{12} - \tilde{g}_{66}$ for the case $J_{\mathrm{NN}}{=}J_{\mathrm{NNN}}{=}0$. Again the collinear and bicollinear phases are stabilized but, as
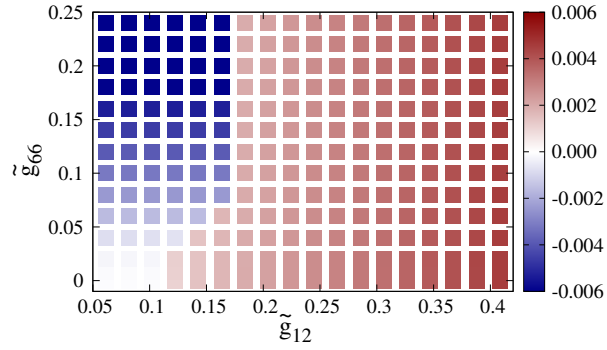
**Figure G.3:** Orthorhombic, $\delta_O$ (blue), and monoclinic, $\delta_M$ (red), lattice distortions varying $\tilde{g}_{66}$ and $\tilde{g}_{12}$ at $T = 10$ K using the spin-fermion model with $J_{\text{NNN}}=J_{\text{NN}}=0$. The scale on the right shows that the lattice distortions obtained numerically are within the correct order of magnitude when compared with experimental data [41, 137, 145]. The values for the orthorhombic distortion are plotted with a negative sign for simplicity to display.

expected, smaller values of the monoclinic coupling are needed to induce the monoclinic phase. Note, however, that a finite value $\tilde{g}_{12} \approx 0.1$ is still required to stabilize the bicollinear phase because the tight-binding term in the Hamiltonian still favors a collinear magnetic state via FS nesting.

The strength of the lattice distortion of Fig. G.2 is shown in Fig. G.3. A reasonable coupling $\tilde{g}_{66} \approx 0.2$ is needed to reproduce the experimental value of the orthorhombic distortion corresponding to the 122 parent compounds. The scale shows that the range in the values of the stabilized monoclinic distortion is also in qualitative agreement with experiments [41, 137, 145].
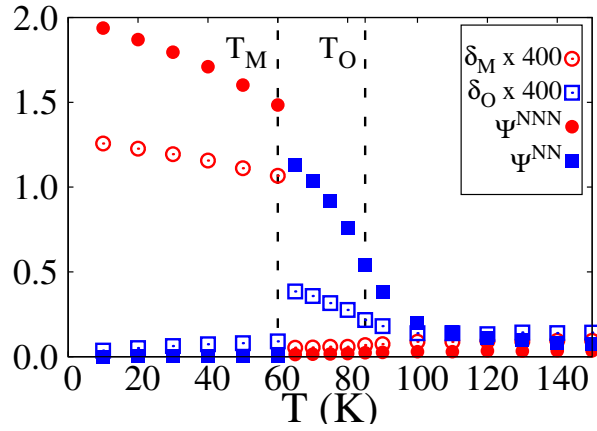
**Figure G.4:** Orthorhombic, $\delta_O$ (blue open squares), and monoclinic, $\delta_M$ (red open circles), lattice distortions and the spin nematic order parameters $\Psi^{NN}$ (blue filled squares) and $\Psi^{NNN}$ (red filled circles) as a function of temperature corresponding to the case $\tilde{g}_{12} = 0.29$, $\tilde{g}_{66} = 0.05$, and with the inclusion of Heisenberg couplings.

# Appendix H

# Unexpected Intermediate Temperature Range of Finite $J_{NNN}/J_{NN}$ for the Hamiltonian Studied in Ch. 4

When Heisenberg couplings are included, the inset of Fig. 4.4) shows an exotic region where the bicollinear/monoclinic transition is preceded by an orthorhombic transition upon cooling. In Fig. G.4 we show the magnetic and structural order parameters for both types of transitions in this unexpected regime. The transition to the collinear/orthorhombic region occurs at about $T = 80$ K and it appears to be continuous, while the bicollinear/monoclinic transition occurs at $T = 60$ K and is strongly first order. Note that in our simulations the orthorhombic phase appears to be accompanied by a collinear magnetic state while experimentally the orthorhombic phase that precedes the monoclinic state in FeTe with excess Fe is magnetically incommensurate [154, 157]. We may need either larger lattices or the explicit addition of extra irons in order to capture the magnetic incommensurability of this phase.
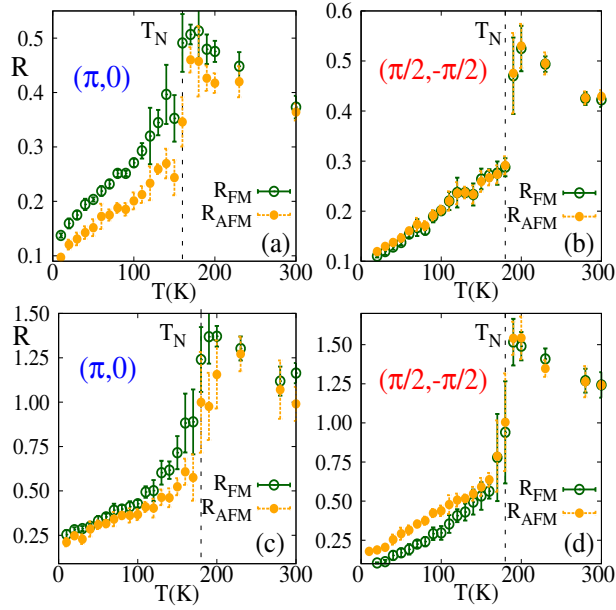
**Figure H.1:** Resistance ($h/2e^2$ units) vs. temperature along the AFM (orange points) and FM (green points) directions in: (a) the collinear/orthorhombic state at $\tilde{g}_{66} = 0.16$, $\tilde{g}_{12} = 0.00$, $J_{\mathrm{H}} = 0.10$ eV, and nonzero Heisenberg couplings; (b) same as (a) but for the bicollinear/monoclinic state with $\tilde{g}_{66} = 0$ and $\tilde{g}_{12} = 0.40$; (c) same as (a) but for $J_{\mathrm{H}} = 0.20$ eV; (d) same as (b) but for $J_{\mathrm{H}} = 0.20$ eV.

# Appendix I

# Reversed Resistivity in FeTe with Details on the Results Presented in Ch. 4

An interesting result reproduced by our study is the anisotropy observed in the planar resistivity of FeTe.

In general, one of the most puzzling behaviors observed in the Fe-based materials is the anisotropic behavior of the in-plane resistivity as the temperature decreases. In the pnictides the cause of the anisotropy is usually attributed to nematicity of electronic origin. In isovalent or electron doped pnictides the resistivity anisotropy develops in the orthorhombic phase and the resistivity is lower along the direction with the largest lattice constant which becomes the antiferromagnetic direction below the magnetic critical temperature. This behavior is in principle counterintuitive because in the colossal magnetoresistive manganites it is well-known that electrons move better in ferromagnetic states. In principle this is not the case in the pnictides due to the geometry of the orbitals that appear at the Fermi surface. Interestingly, a "reversed" or "negative" anisotropy in the resistivity has been observed in the chalcogenides, both in the parent compound FeTe [147, 148] and also in FeSe [181].

The resistance $R$ along the AFM and FM directions was calculated as a function of the temperature following the procedure described in [61] implementing twisted boundary conditions so that the number of accessible momenta along the $x$ and $y$ directions was as large
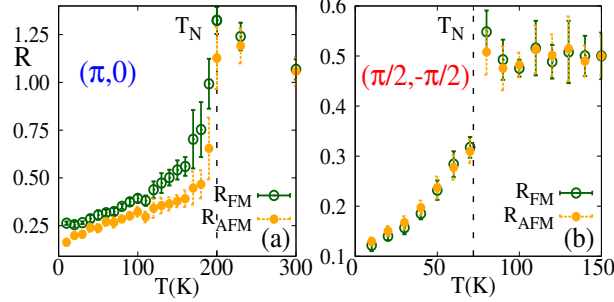
**Figure I.1:** Resistance vs. temperature along the AFM (orange points) and FM (green points) directions in: (a) the collinear/orthorhombic state for $\tilde{g}_{66} = 0.24$, $\tilde{g}_{12} = 0.00$, $J_H = 0.20$ eV, and $J_{NNN}=J_{NN}=0$; (b) same as (a) but for the bicollinear/monoclinic state with $\tilde{g}_{66} = 0.00$, $\tilde{g}_{12} = 0.24$, $J_H = 0.10$ eV, and $J_{NNN}=J_{NN}=0$.

as $L = 256$. The error bars include in these resistivity figures are the standard deviation of the resistivities calculated from 20 different configurations of the classical MC variables. In Fig. H.1 (a) we show the planar resistance in the collinear/orthorhombic phase corresponding to $\tilde{g}_{66} = 0.16$, $\tilde{g}_{12} = 0.00$, $J_H = 0.10$ eV, and nonzero Heisenberg couplings. In this case, the resistance is the smallest along the AFM direction ($x$-direction in the square lattice) in agreement with previous theoretical investigations [79] and with the experimental data for pnictides [71]. In the bicollinear phase, obtained for example at $\tilde{g}_{66} = 0$ and $\tilde{g}_{12} = 0.40$ we actually observe the reversed behavior as shown in Fig. H.1 (b) although here the anisotropy is very small [182]. However, it is experimentally known that the magnetic moment measured in the chalcogenides is larger than the one in the pnictides [41, 137] and, for this reason, we have repeated the simulation increasing the Hund coupling from 0.10 eV to 0.20 eV. As it can be observed in Fig. H.1 (d) the reversed anisotropy effect is now enhanced. On the other hand, a similar increase in Hund coupling decreases the resistance anisotropy in the orthorhombic phase as shown in panel (c) of the same figure. These results indicate that the reversed anisotropy is favored (hindered) by the increase (decrease) in the magnitude of the magnetic moments. A similar response to the Hund coupling is observed for the case where the Heisenberg couplings are zero, as presented in Ch. 4: in Fig. I.1 we display the results illustrating how the anisotropy is reduced with increasing Hund coupling in the collinear phase (panel a) while the reversed anisotropy decreases when the Hund coupling is reduced in the bicollinear phase (panel b).

As already explained in Ch. 4, we believe that this "reversed" anisotropy occurs for reasons similar to those unveiled in manganite investigations [82], namely when electrons move along the AFM direction they must pay an energy as large as $J_{\mathrm{H}}$, while along the FM direction there is no such penalization. This is compatible with the observation that the magnitude of the reversed effect increases with $J_{\mathrm{H}}$.

# Vita

Christopher Bishop was born in St. Louis, Missouri to parents Leonard and Carol Bishop. As an undergraduate, he attended the University of Missouri-St. Louis from 2006 to 2011 where he earned a Bachelors of Science in Physics. After graduation Christopher was accepted to the Doctoral program at the University of Tennessee in Knoxville, Tennessee. While a graduate student, Christopher worked as a Graduate Research Assistant for Dr. Adriana Moreo. During this time, he focused on the numerical study of Iron based superconductors using Spin-Fermion models. Christopher also became interested in high performance computing and parallel programing which has been a useful tool to his previous and current research. The result of his graduate research has been three presentations at the APS march meeting and seven publications in peer reviewed journals. He is scheduled to defend his Ph.D. in August 2017.